

JEOL NEWS

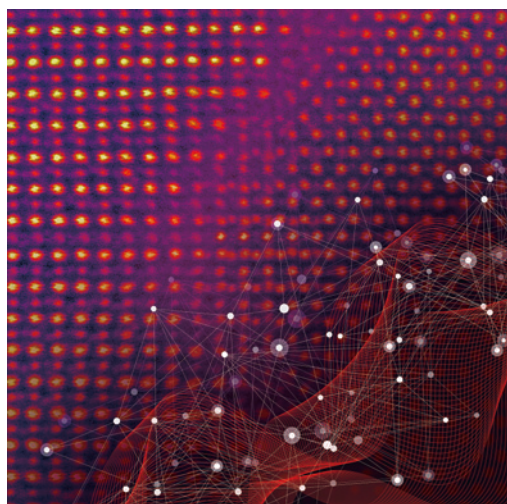
July 2023

Vol.58

No.1



- **Revealing the Latent Atomic World Through Data-Driven Microscopy**2
 Steven R. Spurgeon^{1,2}, Kayla Yano¹, Christina Doty³, Sarah Akers³, and Matthew Olszta¹
¹Energy and Environment Directorate, Pacific Northwest National Laboratory ²Department of Physics, University of Washington
³National Security Directorate, Pacific Northwest National Laboratory
- **Imaging Zeolite Architecture by High Resolution Scanning Electron Microscopy: When Physical and Chemical Etching Meet**12
 Zhengxing Qin, Ye Wang¹, Natsuko Asano², Yanfeng Shen¹, Valentin Valtchev³, Shunsuke Asahina² and Svetlana Mintova^{1,3}
¹China University of Petroleum (East China), ²JEOL Ltd.,
³Normandie Univ, ENSICAEN, UNICAEN, CNRS, Laboratoire Catalyse et Spectrochimie
- **Low-Dose Atomic-Resolution Observation of Beam-Sensitive Materials via OBF STEM Imaging Technique**21
 Kousuke Ooe^{1,2}, Takehito Seki^{2,3}, Yuji Kohno⁴, Akiho Nakamura⁴, Yuichi Ikuhara^{1,2}, Naoya Shibata^{1,2}
¹Nanostructures Research Laboratory, Japan Fine Ceramics Center ²Institute of Engineering Innovation, the School of Engineering, the University of Tokyo
³PRESTO, Japan Science and Technology Agency ⁴JEOL Ltd.
- **Advanced Analytical Methods for the Evaluations of Olefin Polymerization Catalysts and Produced Polymers**27
 Masayoshi Saito¹, Takuo Kataoka¹, Masahide Murata², Yuhei Nakajima³, Rinya Masuko³, Hiroyuki Yamada³, Hideyuki Takahashi³
¹TOHO TITANIUM CO., LTD. ²former TOHO TITANIUM CO., LTD. ³JEOL Ltd.
- **A Practical Method for the Measurement of ¹⁸³W NMR Signals in Solution: Challenge to Multinuclear Solution NMR**35
 Toshiyuki Oshiki Okayama University
- **Introduction of Various Application Examples Obtained by Multi-Purpose TEM (JEM-F200) with Various Attachments**43
 Kei-ichi Fukunaga EM Business Unit, JEOL Ltd.
- **TEM Sample Preparation Using JIB-PS500i and Multi-Purpose FIB-SEM**48
 Misumi Kadoi, Tatsuru Kuramoto, Masateru Shibata, Osamu Suzuki, and Yuichiro Ohori
 EP Business Unit, JEOL Ltd.
- **msFineAnalysis AI Novel Qualitative Analysis Software for JMS-T2000GC with AI Structural Analysis**53
 Ayumi Kubo MS Business Unit, JEOL Ltd.
- **He-less Light Element Analysis Using a Low-Vacuum Liquid Sample Capsule by X-ray Fluorescence Spectrometry**62
 Genki Kinugasa¹, Naoki Muraya¹ and Hiroshi Onodera²
¹SA Business Unit, JEOL Ltd. ²EP Business Unit, JEOL Ltd.



Cover micrograph

Inverted annular bright field image of phase separation in the double perovskite $\text{La}_2\text{MnNiO}_6$, overlaid with an illustration of a convolutional neural network.

Revealing the Latent Atomic World Through Data-Driven Microscopy

Steven R. Spurgeon^{1,2}, Kayla Yano¹, Christina Doty³, Sarah Akers³, and Matthew Olszta¹

¹Energy and Environment Directorate, Pacific Northwest National Laboratory

²Department of Physics, University of Washington

³National Security Directorate, Pacific Northwest National Laboratory

Many emerging technologies depend on the precise design of materials structure, chemistry, and defects. As devices shrink, manufacturing tolerances tighten, and performance envelopes improve, we must increasingly measure and manipulate materials at or near the single atom level. Here we describe how transmission electron microscopy (TEM) underpins our ability to see and direct the latent atomic world. We review a selection of our recent high-resolution TEM studies of the synthesis of oxide-based nanomaterials and their evolution in extreme environments. We then discuss powerful new artificial intelligence (AI) and machine learning (ML) approaches we have developed for rich, reproducible, and scalable experimentation. We conclude by discussing future developments that will enable new materials for breakthrough technologies.

Introduction

Mastery of emerging technologies ranging from quantum computing to energy storage depends on our ability to precisely control materials at ever smaller length scales [1-3]. The central tenet of materials science is that the hierarchy of structure and chemistry – from the atomic to the macroscale – gives rise to properties and determines functionality [4, 5]. Traditionally, low-resolution processing and characterization approaches have been sufficient to incrementally improve materials performance. However, today's high performance materials contain active device regions encompassing just a handful of atoms, necessitating both exceptional resolution and precision throughout in synthesis and processing. For example, the active layers of modern transistors are now single nanometer scale [6, 7], while emerging donor qubits for quantum computing operate on the basis of single donor impurity atoms [1]. As we seek to further improve performance, we must move toward increasingly powerful ways to measure and manipulate materials.

With this goal in mind, the materials community has developed increasingly elaborate synthesis methods and approaches to observe materials in near-operating conditions [3, 8-10]. Synthesis of nanomaterials can be conducted using a variety of approaches, with some of the most powerfully precise being chemical and physical vapor deposition techniques [11, 12]. These approaches are particularly well suited to crafting precise, small volumes of materials such as thin films for electronic, optical, and magnetic devices. Molecular beam epitaxy (MBE) and pulsed laser deposition (PLD), for example, enable exquisite control of reactants to achieve a desired synthesis product. However, these methods are highly nonequilibrium in nature due to kinetic limitations, substrate effects, and the energetics of adsorbed species, often resulting in significant deviations from idealized target structures [13, 14].

Atomically precise characterization thus plays an important role in benchmarking, interpreting, and providing critical insight into materials synthesis processes [2]. Furthermore, such characterization is essential to understand ordering mechanisms, defect formation, and phase transformations, all of which give rise to emergent properties.

There are few methods that can rival the ability of electron microscopy to simultaneously probe materials structure, chemistry, and defects at high spatial resolution. Over the past several decades, transmission electron microscopy (TEM) has emerged as a cornerstone of materials science, providing an unparalleled window into the formation of materials, including property-defining defects [15, 16], the nature of order-disorder phase transitions [2, 17], and the emergence of local electronic and magnetic order [18-20]. Strongly interacting electron probes offer high-resolution insight into crystallography, composition, bonding, phase, kinetics, and electromagnetic response, often simultaneously [3, 21, 22]. The proliferation of aberration-correction, increasingly stable and powerful instrument platforms, and advanced in situ capabilities has cemented the role of this “synchrotron in a box” in laboratories worldwide [23-26]. With every successful material mystery unraveled with TEM, there are also opportunities for development. Alongside the steady pace of hardware innovations, the proliferation of artificial intelligence (AI) and machine learning (ML) in other scientific domains has begun to spill over into microscopy [27-31]. AI/ML agents that can tirelessly and effectively detect latent associations in high volume data streams are beginning to replace slow and difficult to reproduce manual approaches [32, 33]. More importantly, self-driving instrumentation is now becoming possible through the use of programmable instrument controllers [34-36] and human-like ML reasoning [37-39]. These methods will allow us to finally harness the full array of rich data at our disposal, unlocking previously impossible

experimentation across spatial, chemical, and temporal scales.

Here we review a selection of our recent high-resolution and AI-guided electron microscopy studies of the synthesis, emergent properties, and evolution of nanomaterials. We discuss prior analytical successes driven by cutting-edge hardware developments and the potential for self-driving, autonomous microscopy based on reconfigurable, centralized instrument controllers. We show how multimodal, physics-based microscopy can reveal powerful new insights into materials formation, property-defining defects, and the interaction of energy with matter. We conclude with a discussion of emerging ML capabilities for intelligent analytics, control, and forecasting. We argue that these developments are propelling electron microscopy and materials science into a more reproducible and informative era.

Discussion

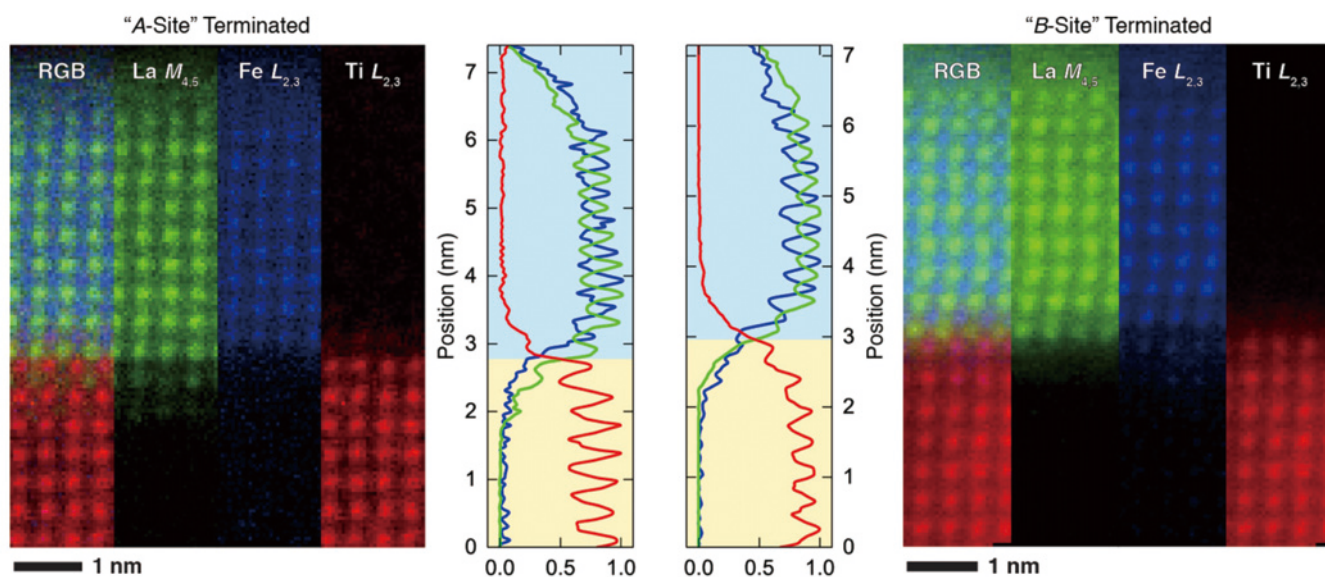
We have organized this focused review into four topical areas, with a particular emphasis on the design and behavior of oxide-based nanomaterials. These materials play a critical role in technologies ranging from quantum information science to energy storage, and their lessons are generalizable to all classes of materials. First, we focus on precision design of functional oxides, which is extremely challenging due to the highly nonequilibrium nature of the associated synthesis approaches. Next, we describe efforts to understand the processing and degradation of oxides, which find use in extreme environments of deep space, nuclear reactors, and high temperatures. We then describe our efforts to create an atomic taxonomy via sparse data analytics, which are particularly well suited to electron microscopy. Finally, we discuss our platform for automated scanning TEM (STEM) utilizing a task-based, centralized communications platform. We explore the possibility of incorporating human-like reasoning into automated experiments and comment on the emerging autonomous future of microscopy.

A. Understanding the Emergence of Order in Thin Film Oxides

Many of today's most important technologies depend on precise control of oxide thin film materials. Their unique structure and chemistry give rise to important properties, such as catalytic behavior, conductivity, and magnetism [40, 41]. However, the synthesis of oxide interfaces is often kinetically limited and subject to substrate constraints, leading to many deviations from ideal, target structures. Our ability to achieve specific functionality thus depends on measuring and understanding synthesis products at high spatial and chemical resolution, a task uniquely suited to STEM. Here we consider two examples of prior work in this area, including understanding dynamic rearrangement during growth and nanoscale phase separation.

Oxide thin film synthesis takes place in complex conditions of elevated temperature (500 – 1200 °C), energetic adatom species, and highly reactive oxygen environments. Precise control of synthesis products depends on our ability to understand dynamic structural and chemical rearrangements, which are known to occur in many systems [14, 42]. This rearrangement is exemplified by our prior studies of heterojunctions of polar / non-polar LaFeO_3 (LFO) / SrTiO_3 (STO), which represents a potentially valuable system for photochemical water splitting [13, 43]. Past work has shown that the termination of the LFO / STO interface affects its band structure and resulting catalytic activity [44]. However, preparation of different terminations of STO (either SrO- or TiO_2 -terminated), followed by MBE growth of LFO, results in very similar electronic structures for the final interface. To investigate this behavior, we examined the final heterojunctions using high-resolution STEM. As shown in **Figure 1**, STEM can directly resolve the excellent quality and crystallinity of the resulting interface. In particular, we observed similar profiles for chemical intermixing and no extended structural defects in either case. Using electron energy loss spectroscopy (EELS), we were able to examine the

Fig. 1 Dynamic Interface Rearrangement.



Cross-sectional EELS analysis of LaFeO_3 grown on two different starting surfaces of SrTiO_3 results in very similar final heterostructures due to dynamic rearrangement. Reproduced from Spurgeon *et al.* [13] with permission of the American Physical Society.

behavior of various alloying elements, finding that in both cases the final heterojunction assumes a LaO / TiO₂ configuration. EELS provides rich information on projected local density of states, as it probes inelastic core loss transitions encountered by the incident electron wave as it passes through the crystal. This measurement informed density functional theory (DFT) calculations, which indicated that the formation of a FeO₂ / SrO configuration was energetically quite unfavorable. Our calculations suggested that, under the growth conditions used, Sr dissolution into the bulk of the film could lead to rearrangement of the interface. In essence, despite having two distinct starting states, the end product was the same. These measurements showcase the strength of STEM to simultaneously resolve structure and chemistry, unlocking local mechanisms to guide more precise synthesis.

While structural and chemical defects are often concentrated at interfaces, they may also emerge later in growth. For example, the buildup of strain imparted by a substrate in a growing material can lead to eventual defects in the form of misfit dislocations or phase separation [45]. Alternatively, the buildup of charge associated with polar / non-polar interfaces may also drive materials to undergo nanoscale phase separation, as shown for nickelate oxides [46]. Observation of such phase separation is challenging using conventional X-ray diffraction (XRD) approaches, which lack sufficient lateral spatial and chemical resolution to uniquely identify local and aperiodic defect configurations. We examined this behavior in the double perovskite La₂MnNiO₆ (LMNO) on STO, which exhibits valuable magnetic properties directly tied to cation ordering and phase purity [15, 47]. We initially observed that ordering in this material was strongly influenced by the incorporation of oxygen during growth; the presence of oxygen vacancies can, in turn, affect cation ordering and magnetic properties. However, upon more detailed investigation, we observed the onset of nanoscale phase separation 1–5 nm into the growth. As shown in **Figure 2**, these regions exhibit a unique lattice-matched structure and appear to consist of largely NiO that has separated

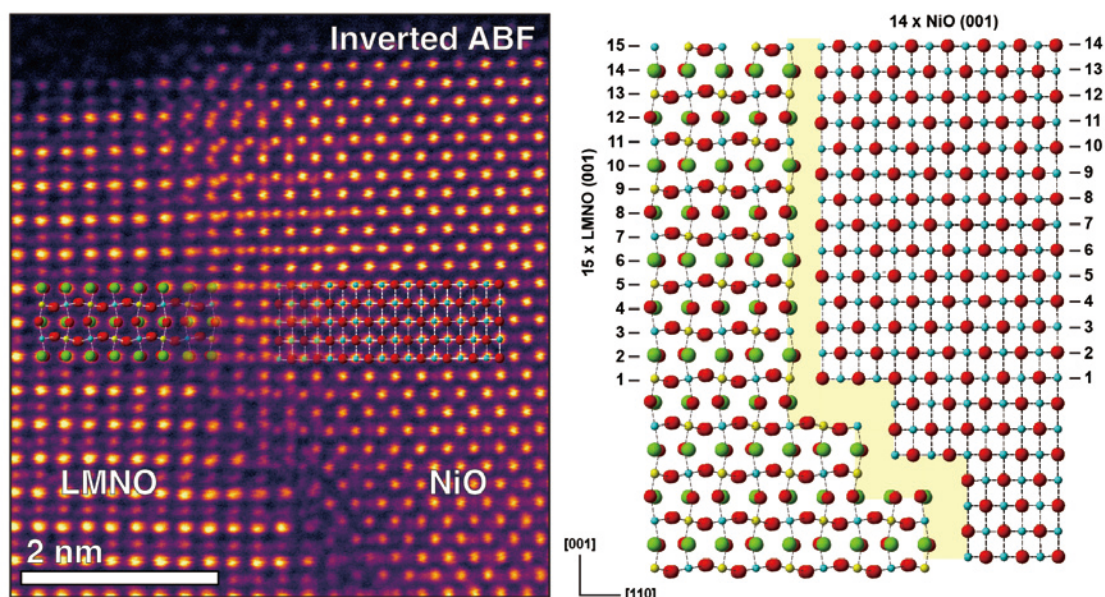
from the LMNO matrix. From STEM annular bright field (ABF) imaging, it is possible to resolve the direct atomic configuration of both light and heavy elements between precipitate and matrix, yielding rich insight into the defect formation process. These observations again informed DFT calculations, which suggested that the buildup of a polar discontinuity during growth leads to initial phase pure growth, followed by phase separation into NiO. Importantly, using local STEM, we are able to effectively detect the presence of these defects, measure their spatial distribution, and determine their configuration to build more accurate models for the synthesis process.

B. Charting the Processing of Nanostructured Materials

Beyond simply synthesizing nanostructured oxides, it is also important to understand their processing and evolution in complex and extreme operating conditions. Many technologies, ranging from solid oxide fuel cells (SOFCs) to sensors and spacecraft, expose materials to extreme environments of temperature, pressure, and irradiation. Thin film oxides represent an excellent testbed to explore the coupling between processing, defects, and functionality, but they have previously received little attention. STEM analysis again provides an excellent probe to examine the unique characteristics of local environments that mediate the interaction of the host lattice with outside radiation. Here we review two examples of our prior work in this area, examining the role of interface configuration on radiation response and dynamic percolation of disorder in these materials.

As already discussed, interface configurations play an important role in determining the functionality of thin film heterostructures. These regions of a material often contain distinct structures, chemistries, and defects that mediate properties. While interfaces have been widely studied in metals by the radiation effects community as potential sources and sinks of radiation-induced defects [48], model oxide interfaces have received far less attention. We have and others have

Fig. 2 Nanoscale Phase Separation.



Charge buildup during the growth of La₂MnNiO₆ double perovskites leads to nanoscale NiO phase separation, as measured by inverted STEM annular bright field, leading to a solution for the interface configuration. Adapted from Spurgeon *et al.* [15] with permission of the American Physical Society.

studied the unique behavior of pyrochlore oxide interfaces [49-51], which are useful in both devices and nuclear waste storage. In particular, we have examined the $\text{La}_2\text{Ti}_2\text{O}_7$ (LTO) system grown on STO and subjected it to controlled ex situ ion irradiation with 1 MeV Zr^+ ions. Using high-resolution STEM imaging and diffraction, we are able to assess the spatial evolution of radiation damage in these materials. As shown in **Figure 3**, we observe extensive amorphization in the bulk of the film and substrate, but also the preservation of a distinct crystalline interface region in these materials. We utilized EELS to probe the chemical environment associated with radiation-induced defects in the vicinity of the interface. Our measurements showed the formation of extensive oxygen vacancies, as manifested by changes in the Ti $L_{2,3}$ and O K edge fine structure, despite the appearance of crystalline order. These findings informed DFT calculations for the energy of formation of defects for different interface configurations. In particular, our modeling showed that the interface has a higher energetic barrier to form oxygen vacancies than the bulk of either LTO film or STO substrate, suggesting that it will be last to disorder, in agreement with our experimental observations. These findings highlight the important role of interface configurations in mediating not just properties, but also radiation response and lifecycle of functional materials.

While ex situ studies of irradiation are powerful, it is well known that the evolution of radiation induced defects is highly transient and that studies of end products provides only partial mechanistic insight [8, 52, 53]. Much of our understanding of radiation effects in nanomaterials can be improved by real-time observation of defect evolution [54]. To address this gap, we examined a model LaMnO_3 (LMO) / STO system using the I³TEM system at Sandia National Laboratories. This microscope is a highly modified JEOL JEM-2100 TEM, with the capability of introducing a MeV-energy level ion irradiation source in situ. In contrast to the polycrystalline or nanostructured materials commonly examined using this microscope, model thin film

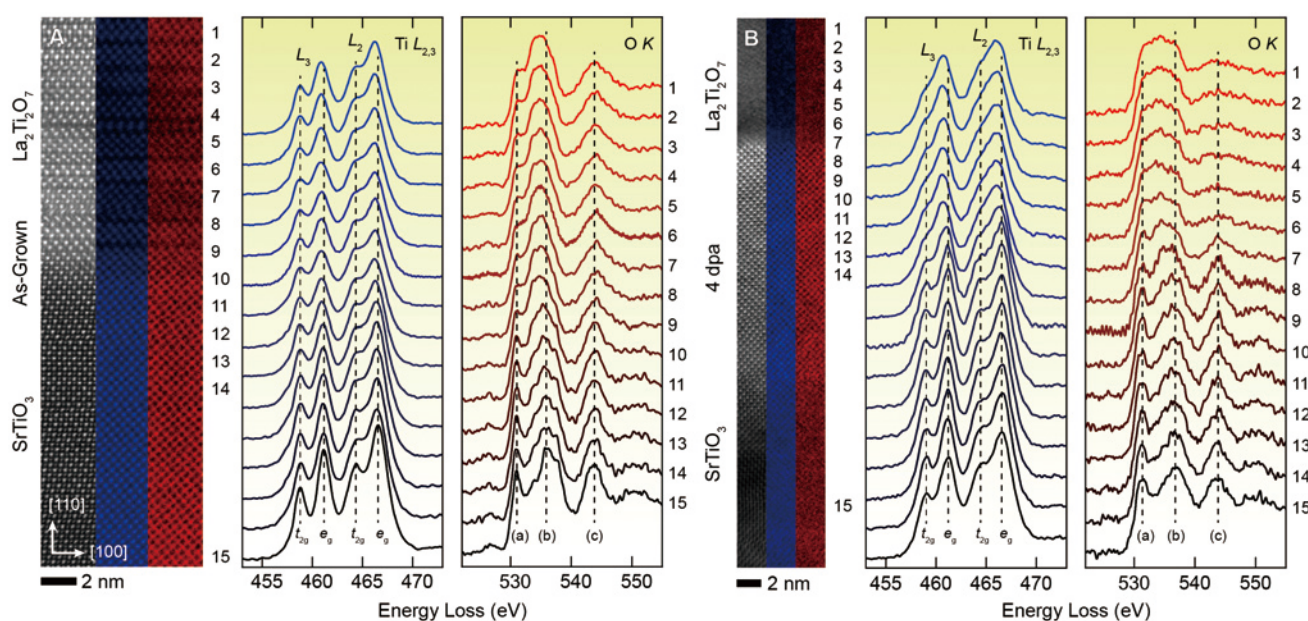
oxides provide a controlled interfacial structure that can be precisely oriented relative to the ion beam.

As shown in **Figure 4**, high-resolution TEM (HRTEM) can be used to visualize the starting interface and its progression under irradiation over approximately 40 minutes to a total fluence of $6.25 \times 10^{14} \text{ Au}^{4+} \text{ cm}^{-2}$. We examined raw images and also measured changes in crystallinity, using time-resolved Fourier filtering of Bragg reflections corresponding to the film lattice planes. This approach allowed us to visualize the initial, largely crystalline microstructure and the percolation of disorder in the vicinity of the interface. We observed that disorder first emerges at the center of the LMO film, in the form of local dislocations, and subsequently progresses to the film-substrate interface. The initial rate of disorder is slow, with just 5% of crystallinity lost in the first 5 minutes, but it soon accelerates to nearly 15% loss between 9 – 19 minutes. At this point, the disorder appears to plateau, with a further drop in crystallinity by 40% at the end of 40 minutes. Our direct observations revealed a complex percolation and breakup of the material, beginning away from the interface and progressing toward it. These results again informed DFT calculations of defect energies, which showed the propensity for LMO to disorder before STO, as observed experimentally. More broadly, these results speak to the powerful local information that in situ TEM can provide, helping us to understand the dynamic evolution of materials in extreme environments.

C. Building the Atomic Taxonomy

As the preceding sections have shown, today's microscopes are capable of generating immense volumes of simultaneous multimodal imaging, spectroscopic, and diffraction data. However, it is presently difficult for us to fully harness and act on such data using conventional analysis approaches, which cannot scale and are prone to irreproducibility because of their human-in-the-loop design. ML methods can potentially analyze data in a more reproducible, holistic, and semantically meaningful way to

Fig. 3 Chemical Analysis of Interfacial Disorder.



EELS measurements of an $\text{La}_2\text{Ti}_2\text{O}_7$ / SrTiO_3 interface before (A-C) and after (D-F) irradiation, showing both the preservation of an interfacial crystalline region and formation of extensive oxygen vacancies. Adapted from Spurgeon *et al.* [49] under CC-BY-4.0 license.

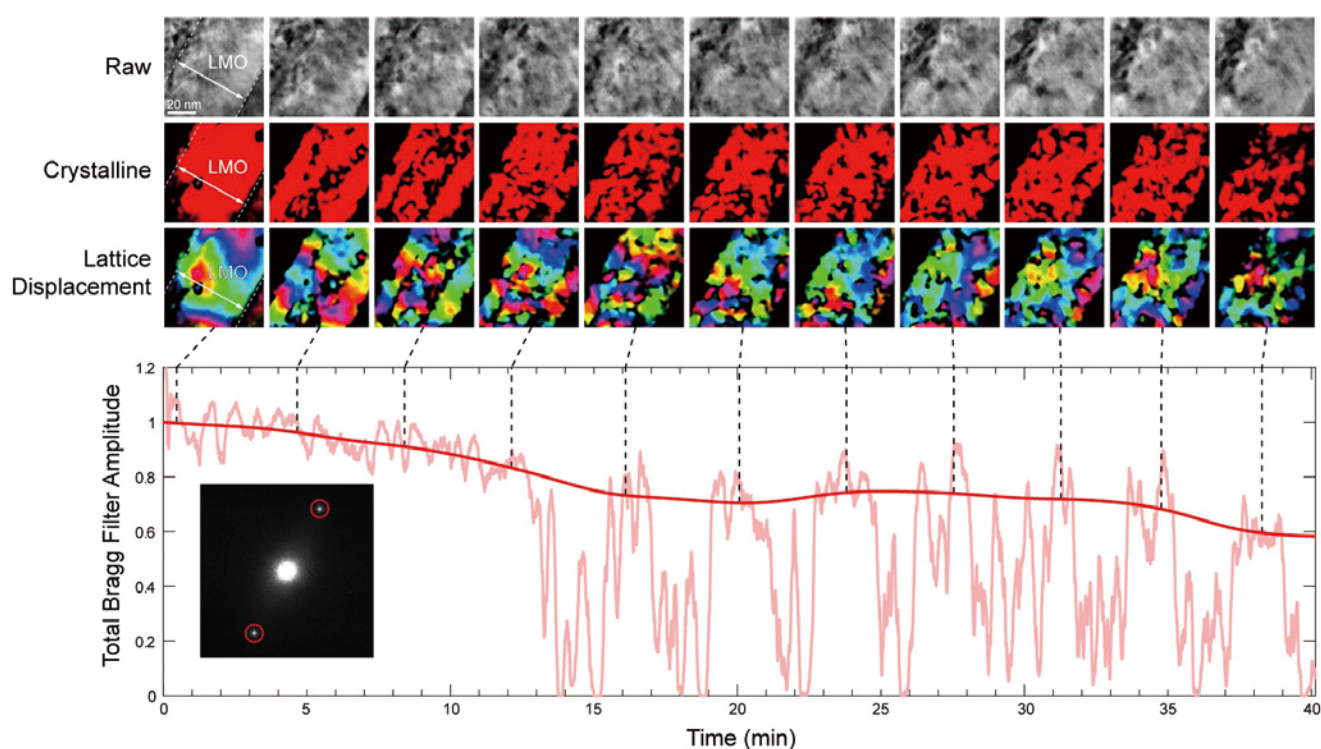
extract relevant materials descriptors [27, 30, 33]. Until recently, these methods have been developed in other domains, and they lack tuning to make them suitable for electron microscopy. We must consider specific characteristics of microscopy data, including data sparsity, a lack of high-quality training data, noisy acquisitions, and the strong dependence of the imaging function on instrument parameters.

We have specifically chosen to address the challenge of data sparsity, which is a major barrier to the adopt of ML in microscopy. As convolutional neural network (CNN) algorithms continue to push computer vision (CV) tasks to unprecedented performance, the community has begun to realize that these data hungry models are difficult or impossible to implement in scientific domains [56]. The high cost of data annotation [57], necessary for model training, creates a brittleness in traditionally trained architectures that causes performant models to fail on out-of-distribution samples. Specifically, there is a need for high-performance models that can accommodate real-world scenarios with few to no annotations. This need has led to development of few-shot learning approaches, which rely on an extremely limited amount of prior information—even one or two data points [58, 59]. The ability to analyze data sets in the presence of limited training data, as is the case for transient, unstable, or novel materials, is an important frontier in materials and data science [32]. As shown in **Figure 5.A**, we have recently developed a flexible few-shot approach that leverages the sparse labeling paradigm to quickly describe and locate regions in electron micrographs [39]. In this approach, a larger microstructure is first broken down into semantically meaningful features known as chips, which may encompass atomic-scale motifs, particles, or grains, for example. These chips are passed through a previously trained encoder and then compared against canonical examples

via a metal earner. The result is a chip level and task-based segmentation of the image, with associated statistics on classes of interest. This model does not require any retraining between tasks and can be effectively scaled to large volumes of data. Most importantly, the model can be quickly adapted to account for new information, taking mere seconds to select new support sets, compared to hours of traditional hand labeling.

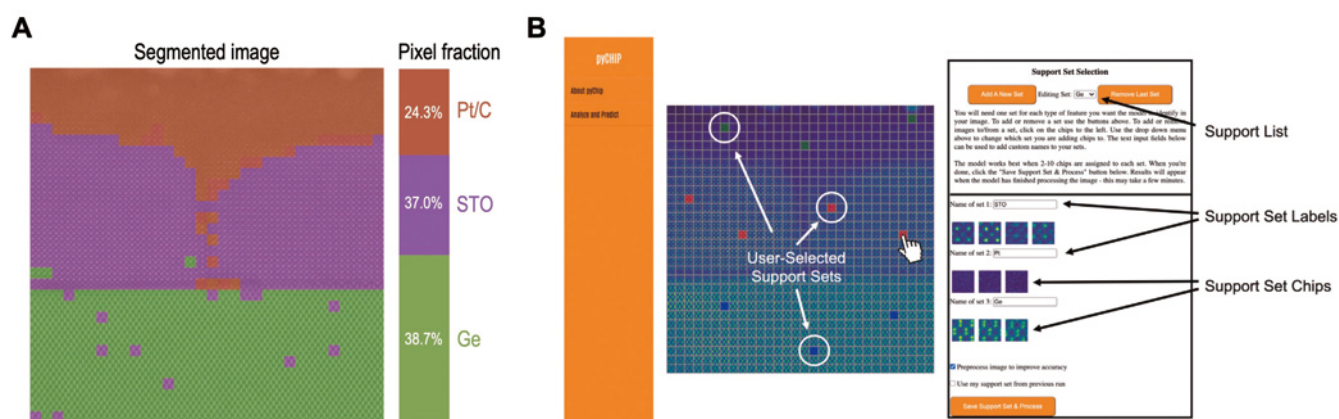
Alongside this model, we have developed an intuitive graphical user interface (GUI) to aid in training and applying a model to new data sets, as shown in **Figure 5.B**. Often, research is primarily focused on model development but not its actual deployment into day to day workflows. The best case scenario at present is typically a Jupyter Notebook or Google Collab distribution. However, these implementations are often difficult to use due to complicated dependencies, their notebook-style execution, and poor runtime performance. A GUI can improve model trustworthiness and explainability, as the images displayed at each stage of the model's training and inference are easily interpreted by a microscopist, and can give much needed context to values such as accuracy and uncertainty [60]. While our model only requires a few examples of each feature type, there are several preprocessing steps that must be performed to prepare these example sets [39]. One step involves identifying a good chip size based on the size of features in the image. The GUI eliminates the trial- and-error in this step by providing the user with a slider, which dynamically updates the size of a grid of chips overlaid on top of their image. Another step involves identifying the location of feature examples within the image. The GUI facilitates this by allowing the user to click on a chip containing a feature to add it to (or remove it from) an example set [60]. This GUI significantly improves the accessibility of the few-shot model to microscopists, while increasing its

Fig. 4 Nanoscale Percolation of Disorder.



In situ HRTEM and time-resolved Fourier filtering reveal pathways for disorder during irradiation of $\text{LaMnO}_3/\text{SrTiO}_3$ interfaces. Reproduced from Matthews *et al.* [55] under CC-BY-4.0 license.

Fig. 5 Sparse Analytics for Material Descriptors.



Emerging few-shot ML can rapidly perform triaging and classification of SrTiO₃ / Ge interfaces by task (A), using a GUI that enables dynamic and transparent model operation (B). Adapted from Akers *et al.* [39] and Doty *et al.* [60] under CC-BY-4.0 license.

interpretability and explainability.

The ability to curate large amounts of data is one facet of next-generation electron microscopy, but copious data without informed collection is also a valid concern, especially when machine learning algorithms are based upon user-provided ground truth. Our research group has developed the protocols coined Nanocartography, which provides microscopists with a toolbox to bridge the gap between reciprocal space and real space [61–64]. As previously noted, control of the stage has often been an overlooked feature in the materials electron microscopy community, most likely owing to the highly site-specific nature of sample analysis. Predictive and precision control of the stage is necessary for performing large area montage, but as well for tilting experiments. Coupling tilting in real space (e.g., morphological examinations and interfaces) to reciprocal space (diffraction) provides microscopists with the ability accurately plan and direct microstructural and microchemical examinations. It has long been known that investigation of grain boundaries is highly dependent upon correct orientation whether towards the appropriate detector [65]. Nanocartography provides the ability to intelligently assess crystallographic orientation with respect to the physical features within a sample as well as the stage. Knowledge of these relationships also allows for rapid re-analysis of samples because orientation can be recalled. Automation of oblique tilt series (i.e., tilt series where the feature of interest is not aligned with the alpha or beta axis) can be programmed to assess three dimensional nature of the sample without destructive analysis and other limitations of full tomography. Finally, adoption of this protocol will promote collaboration between labs, since users can readily share mapping information of various samples, thereby reducing expensive costs associated with re-exploration of existing samples.

D. Moving Toward the Autonomous Future

With the convergence of high-resolution analysis capability and bespoke ML, we are now increasingly moving toward completely automated, AI-guided microscope architectures [31, 35]. As already discussed, models that replicate human-like reasoning are only one part of these architectures; we must also develop centralized controllers to collect data and implement decision-making. As an example, we can consider automated montage

of large statistical volumes of material, which is useful for understanding synthesis products, failure mechanisms, and the evolution of materials in situ. At its simplest, automated montage should provide a scientist user with modifiable settings to dictate the number of images to be taken over a given area. While this technology exists on other instruments, such as scanning electron microscopes (SEMs), arbitrary task-based, self-driving montage is presently unavailable in the STEM.

To address this challenge, we have developed an automated instrument architecture called AutoEM based on asynchronous, centralized control of a JEOL GRAND ARM™ (JEM-ARM300F) STEM instrument [35]. We implement a new low-level Python application programming interface (API), called pyJEM, which allows us to both issue instrument commands and read out data [66]. As shown in **Figure 6**, this platform enables various new automated analysis modes. We consider an example analysis of MoO₃ nanoparticles, a transition metal oxide of significant interest as an energy storage material, photocatalyst, and adsorbent due to its tunable nanostructure [67]. The ability to synthesize desired morphologies (typically plates or rods) is essential, as large surface areas play a key role in catalysis, and statistical analysis can inform improved nanoparticle processing. In open-loop experimentation (Figure 6.A), a user can identify an area of interest and the automated platform will image this region, sending over the final montage to a few-shot ML model trained to distinguish particle features. At this point, the model can branch to different tasks, such as distinguishing all particles from the background or distinguishing different particle types (Figure 6.B). Finally, the system can automatically identify and drive to features of interest determined by the few-shot analysis, as shown in Figure 6.C. AutoEM allows for increased throughput, repeatability, and improved statistics over manual data collection, informing important synthesis and processing outcomes.

Equipped with a centralized instrument controller, we can now implement more sophisticated ML analytics for on-the-fly decision-making during in situ studies. We have recently explored predictive ML for forecasting of chemical reactions in the microscope. Based on a type of recurrent neural network (RNN), long short-term memory models (LSTMs) have found use in prediction of video data [68]. Despite their power, these models have not yet been applied to in situ reactions in the TEM, where they might inform automated decision-making. We have developed a specialized LSTM model for EELS data,

called EELSTM, that allows us to predict the future state of real-time reduction of STO [69]. As shown in **Figure 7**, this model can describe an entire core-loss EELS spectrum with exceptional accuracy relative to ground truth experimental data. Since the core-loss region encodes information about oxidation state and bonding, it is a powerful indicator of local defects formed at different stages of materials processing [9]. EELSTM uses prior spectra to predict a future spectrum and could provide necessary predictive capabilities for automated instrument control in AutoEM. Alternatively, this model may be used to artificially run reactions to completion to further augment the temporal resolution of a given experiment. More broadly, this model shows the power of the modular AutoEM system to incorporate various analytic engines, depending on the desired task.

Conclusions

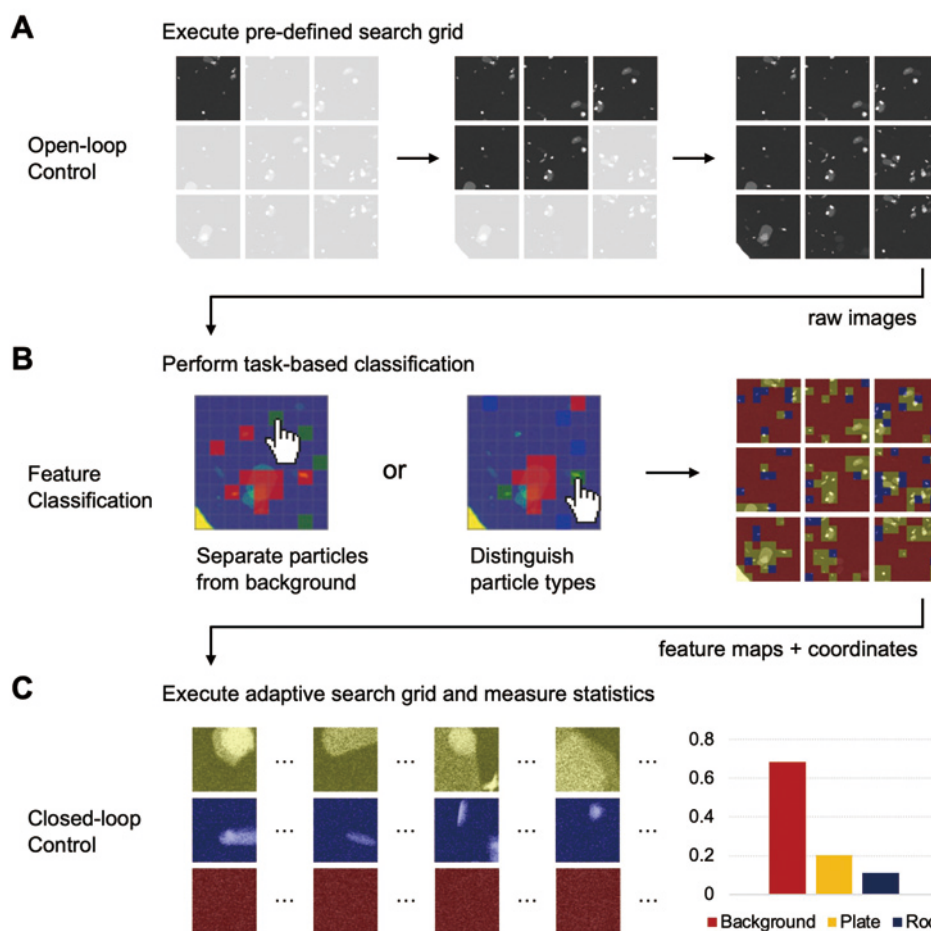
The science of atomic-resolution electron microscopy has illuminated fundamental mechanisms for materials synthesis and processing that would otherwise go unnoticed. It has become a mainstay of modern materials science, chemistry, and physics, continuing to inform our mechanistic understanding of processes that underpin emerging technologies. As we have shown, TEM imaging, spectroscopy, and diffraction can richly probe the complex defect pathways for materials formation and degradation. These methods allow us to better understand how materials will evolve in complex, harsh operating environments, leading to improved materials design and performance lifecycles.

The field of materials science and microscopy are collectively in the midst of transformation. While previous approaches remain valuable, emerging AI/ML will reshape how scientific experimentation is conducted. Our early work has shown that machine intelligence can better harness existing data and unlock powerful new types of experiments. These approaches can lead to more accurate and comprehensive models for materials synthesis and processing. Nonetheless, it is increasingly clear that hardware developments must be accompanied by more agile and open software development. Reconfigurable and modular instrumentation ecosystems, with adaptable hardware, programmable controllers, and interchangeable analytics, represents the future of electron microscopy. These new ecosystems will improve reproducibility and permit broad dissemination of best experimental practices. Constantly updating instrumentation, informed by the latest AI/ML, will elevate the state-of-the-art more broadly and catalyze transformative discovery in the coming decade.

Acknowledgements

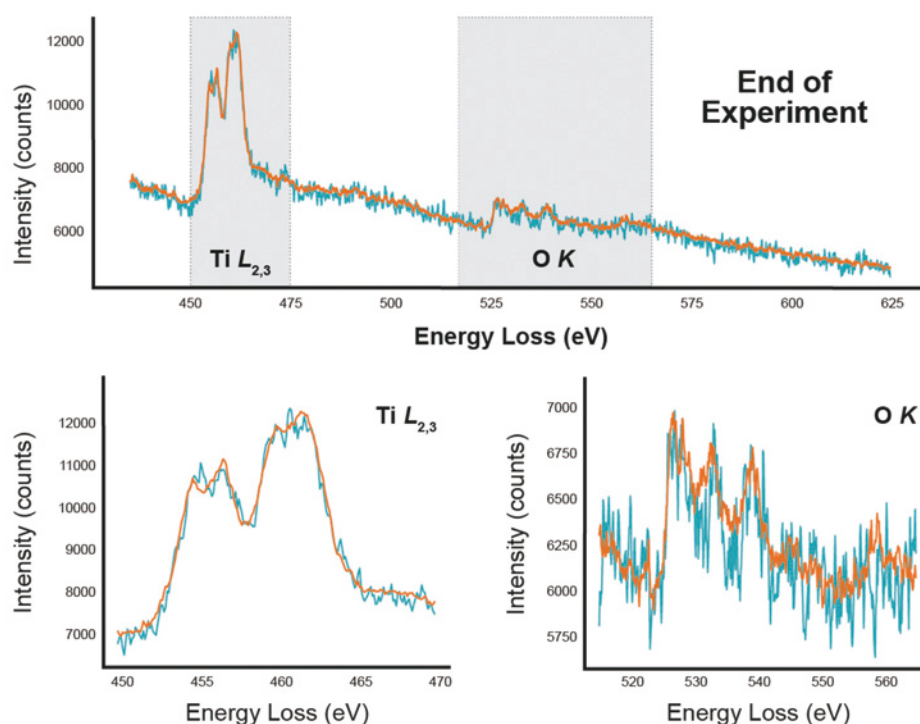
The authors would like to thank Dr. Bethany E. Matthews for reviewing the manuscript. This review was supported by the Chemical Dynamics Initiative/Investment (CDi), under the Laboratory Directed Research and Development (LDRD) program at Pacific Northwest National Laboratory (PNNL). PNNL is a multiprogram national laboratory operated for the U.S. Department of Energy (DOE) by Battelle Memorial Institute

Fig. 6 Sparse Data-Guided Automated Microscopy.



Centralized instrument control and on-the-fly analytics enable automated experimentation. (A–B) Pre-defined search grids provide statistical overviews of MoO₃ nanoparticles, which can be automatically analyzed by task. (C) Analysis results then drive adaptive searches for specific features of interest. Reproduced from Olszta *et al.* [35] under CC-BY-4.0 license.

Fig. 7 ML-Based Forecasting of Phase Transitions.



Specialized LSTM models can accurately predict the future state of reduction in SrTiO₃ via EELS data. The raw data (ground truth) is shown in blue and the prediction is shown in orange. Reproduced from Lewis *et al.* [69] under CC-BY-4.0 license.

under Contract No. DE-AC05-76RL0-1830. The analysis of the LFO and LMNO samples was originally supported by the DOE, Office of Basic Energy Sciences, Division of Materials Science and Engineering under award #10122. The analysis of the LTO and LMO samples was originally supported by Nuclear Processing Science Initiative (NPSI) LDRD at PNNL. Some of the data shown was collected in the Radiological Microscopy Suite (RMS), located in the Radiochemical Processing Laboratory (RPL) at PNNL. Some sample preparation was performed at the Environmental Molecular Sciences Laboratory (EMSL), a national scientific user facility sponsored by the Department of Energy's Office of Biological and Environmental Research and located at PNNL.

References

- [1] N. P. d. Leon, K. M. Itoh, D. Kim, K. K. Mehta, T. E. Northup, H. Paik, B. S. Palmer, N. Samarth, S. Sangtawesin, and D. W. Steuerman, "Materials challenges and opportunities for quantum computing hardware," *Science* **372**, 253 (2021).
- [2] S. R. Spurgeon, "Order-disorder behavior at thin film oxide interfaces," *Current Opinion in Solid State and Materials Science* **24**, 100870 (2020-12), <https://linkinghub.elsevier.com/retrieve/pii/S1359028620300681>.
- [3] C. Zhang, K. L. Firestein, J. F. S. Fernando, D. Siriwardena, J. E. Treinfeldt, and D. Golberg, "Recent Progress of In Situ Transmission Electron Microscopy for Energy Materials," *Advanced Materials* **1904094**, (2019).
- [4] S. R. Kalidindi and M. D. Graef, "Materials Data Science: Current Status and Future Outlook," *Annual Review of Materials Research* **45**, 171–193 (2015-7).
- [5] D. T. Fullwood, S. R. Niezgodna, B. L. Adams, and S. R. Kalidindi, "Microstructure sensitive design for performance optimization," *Progress in Materials Science* **55**, 477–562 (2010-8), <https://linkinghub.elsevier.com/retrieve/pii/S0079642509000760>.
- [6] K. A. Brown, S. Brittman, N. Maccaferri, D. Jariwala, and U. Celano, "Machine Learning in Nanoscience: Big Data at Small Scales," *Nano Letters* **20**, 2–10 (2020).
- [7] I. K. Schuller and R. Stevens, "Neuromorphic Computing : From Materials to Systems Architecture Report of a Roundtable Convened to Consider Neuromorphic Computing," Tech. Rep. (2015).
- [8] R. J. Parrish, D. C. Bufford, D. M. Frazer, C. A. Taylor, J. Gutierrez-Kolar, D. L. Buller, B. L. Boyce, and K. Hattar, "Exploring Coupled Extreme Environments via In-situ Transmission Electron Microscopy," *Microscopy Today* **29**, 28–34 (2021).
- [9] S. Spurgeon and S. Chambers, "Reference Module in Chemistry, Molecular Sciences and Chemical Engineering," in *Encyclopedia of Interfacial Chemistry* (Elsevier, New York, 2017) pp. 38–48, <https://linkinghub.elsevier.com/retrieve/pii/B978012409547212877X>.
- [10] C. J. Palmström, "Heusler compounds and spintronics," *Progress in Crystal Growth and Characterization of Materials* **62**, 371–397 (2016).
- [11] M. Brahlek, A. S. Gupta, J. Lapano, J. Roth, H.-T. T. Zhang, L. Zhang, R. Haislmaier, and R. Engel-Herbert, "Frontiers in the Growth of Complex Oxide Thin Films: Past, Present, and Future of Hybrid MBE," *Advanced Functional Materials* **28**, 1–41 (2018-2).
- [12] S. A. Chambers, "Epitaxial growth and properties of doped transition metal and complex oxide films," *Advanced Materials* **22**, 219–248 (2010-1).
- [13] S. R. Spurgeon, P. V. Sushko, S. A. Chambers, and R. B. Comes, "Dynamic interface rearrangement in LaFeO₃/n-SrTiO₃ heterojunctions," *Physical Review Materials* **1**, 063401 (2017).
- [14] J. H. Lee, G. Luo, I. C. Tung, S. H. Chang, Z. Luo, M.

- Malshe, M. Gadre, A. Bhattacharya, S. M. Nakhmanson, J. A. Eastman, H. Hong, J. Jellinek, D. Morgan, D. D. Fong, and J. W. Freeland, "Dynamic layer rearrangement during growth of layered oxide films by molecular beam epitaxy," *Nature Materials* **13**, 879–883 (2014), <http://doi.wiley.com/10.1002/adfm.201102763>.
- [15] S. R. Spurgeon, P. V. Sushko, A. Devaraj, Y. Du, T. Droubay, and S. A. Chambers, "Onset of phase separation in the double perovskite oxide $\text{La}_2\text{MnNiO}_6$," *Physical Review B* **97**, 134110 (2018), <https://pubs.acs.org/doi/10.1021/acs.chemmater.6b00829>, 1710.08535.
- [16] S. A. Chambers, Y. Du, Z. Zhu, J. Wang, M. J. Wahila, L. F. J. Piper, A. Prakash, J. Yue, B. Jalan, S. R. Spurgeon, D. M. Kepaptsoglou, Q. M. Ramasse, and P. V. Sushko, "Interconversion of intrinsic defects in SrTiO_3 (001)," *Physical Review B* **97**, 245204 (2018).
- [17] C. M. Rost, E. Sachet, T. Borman, A. Moballeggh, E. C. Dickey, D. Hou, J. L. Jones, S. Curtarolo, and J.-P. Maria, "Entropy-stabilized oxides," *Nature Communications* **6**, 8485 (2015).
- [18] D. G. Schlom, L.-Q. Chen, C. J. Fennie, V. Gopalan, D. a. Muller, X. Pan, R. Ramesh, and R. Uecker, "Elastic strain engineering of ferroic oxides," *MRS Bulletin* **39**, 118–130 (2014).
- [19] T. Zhang, X. P. Wang, Q. F. Fang, and X. G. Li, "Magnetic and charge ordering in nanosized manganites," *Applied Physics Reviews* **031302**, 0–21 (2014).
- [20] H. Y. Hwang, Y. Iwasa, M. Kawasaki, B. Keimer, N. Nagaosa, and Y. Tokura, "Emergent phenomena at oxide interfaces," *Nature Materials* **11**, 103–113 (2012).
- [21] C. Colliex, "From a physicist's toy to an indispensable analytical tool in many fields of science: A personal view of the leading contribution of Ondrej Krivanek to the spectacular successes of EELS spectroscopy in the electron microscope," *Ultramicroscopy* **180**, 14–21 (2017).
- [22] H. Zheng, Y. S. Meng, and Y. Zhu, "Frontiers of in situ electron microscopy," *MRS Bulletin* **40**, 12–18 (2015), <https://www.cambridge.org/core/product/identifier/S0883769414003054/type/journal-article>.
- [23] Q. M. Ramasse, "Twenty years after: How "Aberration correction in the STEM" truly placed a "A synchrotron in a Microscope"," *Ultramicroscopy* **180**, 41–51 (2017).
- [24] I. MacLaren and Q. M. Ramasse, "Aberration-corrected scanning transmission electron microscopy for atomic-resolution studies of functional oxides," *International Materials Reviews* **59**, 115–131 (2014).
- [25] D. a. Muller, "Structure and bonding at the atomic scale by scanning transmission electron microscopy." *Nature materials* **8**, 263–70 (2009-4).
- [26] P. E. Batson, N. Dellby, and O. L. Krivanek, "Sub-ångstrom resolution using aberration corrected electron optics," *Nature* **419**, 94–94 (2002), <http://www.ncbi.nlm.nih.gov/pubmed/12167855>.
- [27] K. P. Treder, C. Huang, J. S. Kim, and A. I. Kirkland, "Applications of deep learning in electron microscopy," *Microscopy* **71**, i100–i115 (2022).
- [28] M. Xu, A. Kumar, and J. M. LeBeau, "Towards Augmented Microscopy with Reinforcement Learning-Enhanced Workflows," *Microscopy and Microanalysis*, 1–9 (2022), 2208.02865.
- [29] M. Ziatdinov, A. Ghosh, C. Y. T. Wong, and S. V. Kalinin, "Atom AI framework for deep learning analysis of image and spectroscopy data in electron and scanning probe microscopy," *Nature Machine Intelligence*, 1–12 (2022).
- [30] J. M. Ede, "Deep learning in electron microscopy," *Machine Learning: Science and Technology* **2**, 011004 (2021), <https://iopscience.iop.org/article/10.1088/2632-2153/abd614>, 2009.08328.
- [31] S. V. Kalinin, M. A. Ziatdinov, J. Hinkle, S. Jesse, A. Ghosh, K. P. Kelley, A. R. Lupini, B. G. Sumpter, and R. K. Vasudevan, "Automated and Autonomous Experiment in Electron and Scanning Probe Microscopy," *ACS Nano* **15**, 1–48 (2021), 2103.12165.
- [32] S. V. Kalinin, M. Ziatdinov, S. R. Spurgeon, C. Ophus, E. A. Stach, T. Susi, J. Agar, and J. Randall, "Deep learning for electron and scanning probe microscopy: From materials design to atomic fabrication," *MRS Bulletin* **47**, 931–939 (2022).
- [33] S. R. Spurgeon, C. Ophus, L. Jones, A. Petford-Long, S. V. Kalinin, M. J. Olszta, R. E. Dunin-Borkowski, N. Salmon, K. Hattar, W.-c. D. Yang, R. Sharma, Y. Du, A. Chiaramonti, H. Zheng, E. C. Buck, L. Kovarik, R. L. Penn, D. Li, X. Zhang, M. Murayama, and M. L. Taheri, "Towards data-driven next-generation transmission electron microscopy," *Nature Materials* **20**, 274–279 (2021), <http://www.nature.com/articles/s41563-020-00833-z>.
- [34] K. M. Roccapriore, M. G. Boebinger, O. Dyck, A. Ghosh, R. R. Unocic, S. V. Kalinin, and M. Ziatdinov, "Probing Electron Beam Induced Transformations on a Single-Defect Level via Automated Scanning Transmission Electron Microscopy," *ACS Nano* **16**, 17116–17127 (2022).
- [35] M. Olszta, D. Hopkins, K. R. Fiedler, M. Oostrom, S. Akers, and S. R. Spurgeon, "An Automated Scanning Transmission Electron Microscope Guided by Sparse Data Analytics," *Microscopy and Microanalysis* **28**, 1611–1621 (2022), 2109.14772.
- [36] M. Schorb, I. Haberbosch, W. J. Hagen, Y. Schwab, and D. N. Mastronarde, "Software tools for automated transmission electron microscopy," *Nature Methods* **16**, 471–477 (2019).
- [37] Y. Liu, K. P. Kelley, R. K. Vasudevan, H. Funakubo, M. A. Ziatdinov, and S. V. Kalinin, "Experimental discovery of structure–property relationships in ferroelectric materials via active learning," *Nature Machine Intelligence* **4**, 341–350 (2022).
- [38] M. Ziatdinov, Y. Liu, K. Kelley, R. Vasudevan, and S. V. Kalinin, "Bayesian Active Learning for Scanning Probe Microscopy: From Gaussian Processes to Hypothesis Learning," *ACS Nano* **16**, 13492–13512 (2022).
- [39] S. Akers, E. Kautz, A. Trevino-Gavito, M. Olszta, B. E. Matthews, L. Wang, Y. Du, and S. R. Spurgeon, "Rapid and flexible segmentation of electron microscopy data using few-shot machine learning," *npj Computational Materials* **7**, 187 (2021).
- [40] J. Chakhalian, J. W. Freeland, A. J. Millis, C. Panagopoulos, and J. M. Rondinelli, "Emergent properties in plane view: Strong correlations at oxide interfaces," *Reviews of Modern Physics* **86**, 1189–1202 (2014), <http://link.aps.org/doi/10.1103/RevModPhys.86.1189>, 1408.3173.
- [41] J. Mannhart and D. G. Schlom, "Oxide Interfaces—An Opportunity for Electronics," *Science* **327**, 1607–1611 (2010), <http://www.sciencemag.org/cgi/doi/10.1126/science.1181862>.
- [42] G. Saint-Girons, R. Bachelet, R. Moalla, B. Meunier, L. Louahadj, B. Canut, A. Carretero-Genevri, J. Gazquez, P. Regreny, C. Botella, J. Penuelas, M. G. Silly, F. Sirotti, and G.

- Grenet, "Epitaxy of SrTiO₃ on Silicon: The Knitting Machine Strategy," *Chemistry of Materials* **28**, 5347–5355 (2016).
- [43] R. Comes and S. Chambers, "Interface structure, band alignment, and built-in potentials at LaFeO₃ / n-SrTiO₃ heterojunctions," *Physical Review Letters* **117**, 226802 (2016), <https://link.aps.org/doi/10.1103/PhysRevLett.117.226802>.
- [44] K. Stoerzinger, R. Comes, S. Spurgeon, S. Thevuthasan, K. Ihm, E. Crumlin, and S. Chambers, "Influence of LaFeO₃ Surface Termination on Water Reactivity," *The Journal of Physical Chemistry Letters* **8**, 1038 – 1043 (2017).
- [45] J. L. Macmanus-Driscoll, "Self-assembled heteroepitaxial oxide nanocomposite thin film structures: Designing interface-induced functionality in electronic materials," *Advanced Functional Materials* **20**, 2035–2045 (2010).
- [46] E. Detemple, Q. M. Ramasse, W. Sigle, G. Cristiani, H.-U. Habermeier, E. Benckiser, a. V. Boris, A. Frano, P. Wochner, M. Wu, B. Keimer, and P. A. v. Aken, "Polarity-driven nickel oxide precipitation in LaNiO₃-LaAlO₃ superlattices," *Applied Physics Letters* **99**, 211903 (2011).
- [47] S. R. Spurgeon, Y. Du, T. Droubay, A. Devaraj, X. Sang, P. Longo, P. Yan, P. G. Kotula, V. Shutthanandan, M. E. Bowden, J. M. LeBeau, C. Wang, P. V. Sushko, and S. A. Chambers, "Competing Pathways for Nucleation of the Double Perovskite Structure in the Epitaxial Synthesis of La₂MnNiO₆," *Chemistry of Materials* **28**, 3814–3822 (2016), <http://dx.doi.org/10.1021/acs.chemmater.6b00829> <http://pubs.acs.org/doi/abs/10.1021/acs.chemmater.6b00829>
- [48] I. Beyerlein, A. Caro, M. Demkowicz, N. Mara, A. Misra, and B. Uberuaga, "Radiation damage tolerant nanomaterials," *Materials Today* **16**, 443–449 (2013-11), <https://linkinghub.elsevier.com/retrieve/pii/S1369702113003581>.
- [49] S. R. Spurgeon, T. C. Kaspar, V. Shutthanandan, J. Gigax, L. Shao, and M. Sassi, "Asymmetric Lattice Disorder Induced at Oxide Interfaces," *Advanced Materials Interfaces* **7**, 1901944 (2020), <https://onlinelibrary.wiley.com/doi/abs/10.1002/admi.201901944>, 1904.05932.
- [50] T. C. Kaspar, J. G. Gigax, L. Shao, M. E. Bowden, T. Varga, V. Shutthanandan, S. R. Spurgeon, P. Yan, C. Wang, P. Ramuhalli, and C. H. Henager, "Damage evolution of ion irradiated defected-fluorite La₂Zr₂O₇ epitaxial thin films," *Acta Materialia* **130**, 111–120 (2017-5), <https://linkinghub.elsevier.com/retrieve/pii/S1359645417300228>.
- [51] T. C. Kaspar, S. Hong, M. E. Bowden, T. Varga, P. Yan, C. Wang, S. R. Spurgeon, R. B. Comes, P. Ramuhalli, and C. H. Henager, "Tuning piezoelectric properties through epitaxy of La₂Ti₂O₇ and related thin films," *Scientific Reports* **8**, 3037 (2018).
- [52] K. Hattar and K. L. Jungjohann, "Possibility of an integrated transmission electron microscope: enabling complex in-situ experiments," *Journal of Materials Science* **56**, 5309–5320 (2021).
- [53] K. Hattar, D. Bufford, and D. Buller, "Concurrent in situ ion irradiation transmission electron microscope," *Nuclear Instruments and Methods in Physics Research Section B: Beam Interactions with Materials and Atoms* **338**, 56–65 (2014-11), <https://linkinghub.elsevier.com/retrieve/pii/S0168583X14007046>.
- [54] X. Zhang, K. Hattar, Y. Chen, L. Shao, J. Li, C. Sun, K. Yu, N. Li, M. L. Taheri, H. Wang, J. Wang, and M. Nastasi, "Radiation damage in nanostructured materials," *Progress in Materials Science* **96**, 217–321 (2018-7), <https://linkinghub.elsevier.com/retrieve/pii/S007964251830032X>.
- [55] B. E. Matthews, M. Sassi, C. Barr, C. Ophus, T. C. Kaspar, W. Jiang, K. Hattar, and S. R. Spurgeon, "Percolation of Ion-Irradiation-Induced Disorder in Complex Oxide Interfaces," *Nano Letters* **21**, 5353–5359 (2021).
- [56] N. Fujinuma, B. DeCost, J. Hattrick-Simpers, and S. E. Lofland, "Why big data and compute are not necessarily the path to big materials science," *Communications Materials* **3**, 59 (2022).
- [57] R. Sainju, W.-Y. Chen, S. Schaefer, Q. Yang, C. Ding, M. Li, and Y. Zhu, "DefectTrack: a deep learning-based multi-object tracking algorithm for quantitative defect analysis of in-situ TEM videos in real-time," *Scientific Reports* **12**, 15705 (2022).
- [58] A. Parnami and M. Lee, "Learning from Few Examples: A Summary of Approaches to Few-Shot Learning," arXiv (2022), 10.48550/arxiv.2203.04291, 2203.04291.
- [59] K. Kaufmann, H. Lane, X. Liu, and K. S. Vecchio, "Efficient few-shot machine learning for classification of EBSD patterns," *Scientific Reports* **11**, 8172 (2021), <http://www.nature.com/articles/s41598-021-87557-5>.
- [60] C. Doty, S. Gallagher, W. Cui, W. Chen, S. Bhushan, M. Oostrom, S. Akers, and S. R. Spurgeon, "Design of a graphical user interface for few-shot machine learning classification of electron microscopy data," *Computational Materials Science* **203**, 111121 (2022-2), <https://linkinghub.elsevier.com/retrieve/pii/S0927025621007874>, 2107.10387.
- [61] M. Olszta, K. Fiedler, D. Hopkins, K. Yano, C. Doty, M. Oostrom, S. Akers, and S. R. Spurgeon, "Pivot Point: The Key to TEM Automation," *Microscopy and Microanalysis* **28**, 2920–2921 (2022).
- [62] M. Olszta and K. Fiedler, "Nanocartography: Planning for success in analytical electron microscopy," arXiv (2022), 10.48550/arxiv.2205.03956, 2205.03956.
- [63] M. Olszta, K. Fiedler, S. Spurgeon, S. Reehl, and D. Hopkins, "The role of Nanocartography in the Development of Automated TEM," *Microscopy and Microanalysis* **27**, 2986–2987 (2021).
- [64] M. Olszta and K. Fiedler, "Nanocartography in the Age of Automated TEM," *Microscopy and Microanalysis* **26**, 32–32 (2020).
- [65] D. A. Muller and M. J. Mills, "Electron microscopy: probing the atomic structure and chemistry of grain boundaries, interfaces and defects," *Materials Science and Engineering: A* **260**, 12–28 (1999).
- [66] JEOL, "PyJEM Software Package, Available at <https://github.com/PyJEM/PyJEM>," (2023).
- [67] Y. Gong, Y. Dong, B. Zhao, R. Yu, S. Hu, and Z. Tan, "Diverse applications of MoO₃ for high performance organic photovoltaics: fundamentals, processes and optimization strategies," *Journal of Materials Chemistry A* **8**, 978–1009 (2019).
- [68] C. Robertson, J. L. Wilmoth, S. Retterer, and M. Fuentes-Cabrera, "Performing Video Frame Prediction of Microbial Growth with a Recurrent Neural Network," arXiv, 1–15 (2022), 2205.05810.
- [69] N. R. Lewis, Y. Jin, X. Tang, V. Shah, C. Doty, B. E. Matthews, S. Akers, and S. R. Spurgeon, "Forecasting of in situ electron energy loss spectroscopy," *npj Computational Materials* **8**, 252 (2022).

Imaging Zeolite Architecture by High Resolution Scanning Electron Microscopy: When Physical and Chemical Etching Meet

Zhengxing Qin, Ye Wang¹, Natsuko Asano², Yanfeng Shen¹, Valentin Valtchev³, Shunsuke Asahina² and Svetlana Mintova^{1,3}

¹ China University of Petroleum (East China), ² JEOL Ltd.,

³ Normandie Univ, ENSICAEN, UNICAEN, CNRS, Laboratoire Catalyse et Spectrochimie

“Seeing is believing”. The clear imaging of zeolite crystals down to a nano-scale is important, as the size and morphology information is very helpful in guiding the design and synthesis of zeolite crystals. Besides, a detailed acquisition of zeolite properties (crystal architecture characteristics, elements distribution, porosity, etc.) is an essential prerequisite for the comprehensive understanding of structure-performance relationships. However, zeolites, especially those with a nanosized dimension, are notorious for its difficult-to-characterization by scanning electron microscopy, as these materials are nonconductive and electron irradiation sensitive, both of which are not favorable for the acquisition of high-resolution images. The born of high-resolution low incident voltage SEM solved beautifully the problem that has troubled zeolite scientists for a long time. As a result, the clear observation of the intrinsic surface of zeolite crystals without masking by conductive nanoparticles becomes a reality. Besides, the combination of high-resolution imaging with physical (ion beam polishing) and chemical (NH₄F) etching make scanning electron microscopy a new choice for the imaging of the inner parts of zeolite crystals.

Introduction

Zeolites are crystalline inorganic microporous materials that find many important applications in the fields of ion exchange, catalysis, and sorption/separation, thanks to their tunable Si/Al ratio and acidity, unique shape selectivity, and outstanding thermal and hydrothermal stability. The understanding of the surface structure characteristics and the precise analysis of the local arrangement of elements in these materials are prerequisite for the comprehensive understanding of the inter-correlated synthesis-structure-performance relationships, which, however, depends on the availability of sophisticated analysis techniques. At present, the state-of-the-art imaging technologies for the characterization of the structure and composition of nanostructures are transmission electron microscope (TEM) and scanning electron microscope (SEM). TEM can obtain local composition and crystal structure information at atomic-level as projection information, but it is difficult to selectively obtain surface information. In comparison, SEM has a large depth of focus and can obtain surface morphology information with secondary electron images, composition information with EDX method, and crystal orientation information using backscattered electron detector even for samples with height differences, so it

is expected to be applied especially for the characterization of the surface of zeolites that even have surface roughness.

However, SEM has issues with an insufficient spatial resolution, electron charging and severe damage by electron beams for zeolites which are very sensitive to the incident electron beams. In addition, zeolites are particles that, no matter how small or large, have certain sizes in a three-dimensional space. As a result, the properties of zeolites are determined not only by its surface structure properties, but are much more determined by their internal architectures including, but not limited to, the spatial distribution of elements in the inner part of zeolite crystals. Further, in order to improve the diffusion and sorption properties of zeolite crystals, the engineering of zeolite crystals through the introduction of intra-particle secondary porosity is an important aspect in the field of zeolite research. A comprehensive understanding of the size, morphology, connectivity and spatial distribution of the hierarchical pores is important, both for the further optimization of the preparation of hierarchical zeolites, and for the interpretation of their performance in applications. However, the majority of this secondary porosity is hidden inside crystal volume, which is not reachable via routine SEM characterization.

In order to solve these problems and obtain structural

information that govern the properties of zeolites, development of a high-resolution low incident voltage SEM for the characterization of beam sensitive materials is highly desirable. On the other hand, in the low incident voltage SEM, the effects of objective lens aberration and chromatic aberration become significant, and the electron probe diameter increases, resulting in a decrease in spatial resolution. For this reason, JEOL has been working to improve the spatial resolution of the SEM under low incident voltage conditions. As a result, even at a low incident voltage of several 100 V, many structural details, such as steps and pores of a few nanometers, can be observed on the zeolite surface, as will be seen below. As far as the inner architecture of zeolite crystals is concerned, the samples can be cut with an ion beam (physical etching, **Figure 1a**), then the cross-section imaging of zeolites can be conducted using the high-resolution low incident voltage SEM system. In addition, the high-resolution imaging can be combined with fluoride etching (Figure 1b), a chemical etching approach that is able to remove framework Si and Al atoms from zeolite framework permanently, and, in a non-biased manner [1]. As a result, many inner architecture details in zeolite crystals hitherto unknown was revealed for the first time.

Experimental

-Samples-

Two ZSM-5 samples (denoted MFI-1 and MFI-2), a FAU-Y zeolite, and a SAPO-34 zeotype was used for demonstration purpose in the present study. The source of these samples is shown as follows:

MFI-1: a home-made sample synthesized according to the procedures described in reference [2];

MFI-2: offered by Clariant;

FAU-Y zeolite: provided by UOP;

SAPO-34: purchased from XFANO company.

-Fluoride medium etching-

Fluoride medium etching of both as-prepared and calcined ZSM-5 zeolites was carried out in NH_4F aqueous solution using the following procedure: 1 g of the pristine ZSM-5 zeolite was dispersed in 20 to 30 g of 40 wt.% NH_4F aqueous solution and reacted at 50 °C for up to 4 h under mechanical stirring. Intermediate samples were taken out after a specific reaction time. The etched products were thoroughly washed with distilled water after the fluoride medium treatment.

Fluoride medium etching of NH_4Y zeolite was conducted in 25 to 30 wt.% NH_4F (98.0%, Sigma-Aldrich) solution. The treatment was performed under ultrasonic radiation (USC 600 TH, 45 kHz, VWR) in an ice bath for 1 to 15 min. The solid products were washed thoroughly and dried.

The NH_4F treatment of the parent SAPO-34 was carried out in 4 wt.% NH_4F solution. 2 g SAPO-34 was added into 40 g NH_4F solution and then the solution was stirred (400 rpm) at room temperature for 2.5 minutes. At last, the treated samples were collected by vacuum filtration, washed with deionized water and dried at 393 K.

-SEM and TEM characterization-

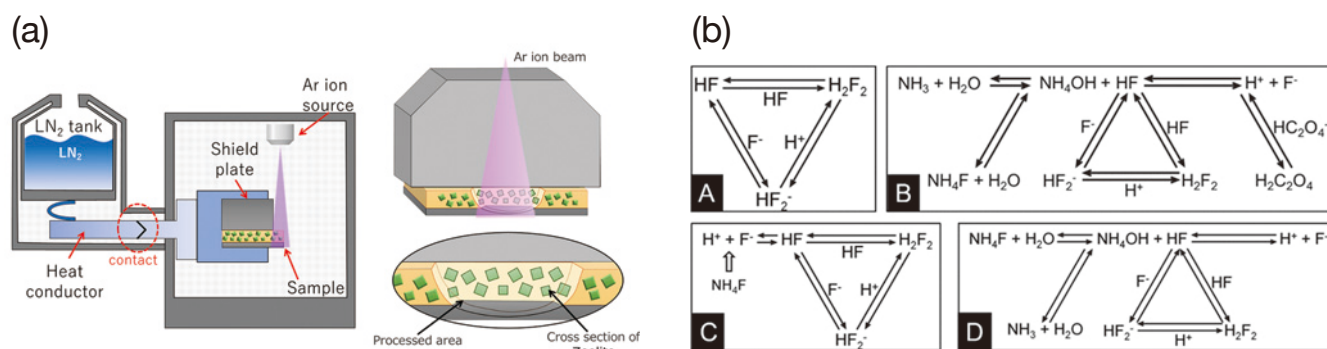
Scanning electron microscopy (SEM) images of non-coated zeolite surface were taken with JEOL scanning electron microscopes equipped with a field emission gun. The cross-section of zeolite samples was prepared by using an IB-19510CP (JEOL) ion Beam cross-section polisher. TEM images were recorded using a JEOL JEM-2100F microscope with a high voltage of 200 kV, equipped with a high-resolution objective lens pole piece.

Results and Discussion

1) High resolution imaging of zeolite surface by low voltage SEM

When using a SEM to characterize zeolite crystals, the first expectation is to “see” the sample surface clearly. Previously, however, this was non-trivial a task especially for the observation of nano-sized zeolites. The surface imaging of zeolite samples by SEM is very sensitive to the primary electron beam. By varying the energy of primary electrons, different information of the zeolite structures can be obtained. A simulation result of interaction volume of incident electrons in the silicon using Monte Carlo simulation method is presented in **Figure 2a-c**. Notably, the incident electrons can diffuse with a depth of 200 nm from the surface and the diffusion width is larger than 200 nm when the accelerating voltage is set as 3 kV. However, although the high energy electrons can penetrate into the inner part of the sample and emit a large number of electrons, the output of surface information is little, preventing the clear observation of the surface structure (Figure 2d). In contrast, the penetrated depth and width are less than 8 nm when the accelerating voltage is reduced to 0.3 kV. In this case, the secondary electrons are just generated from a narrow interaction

Fig. 1



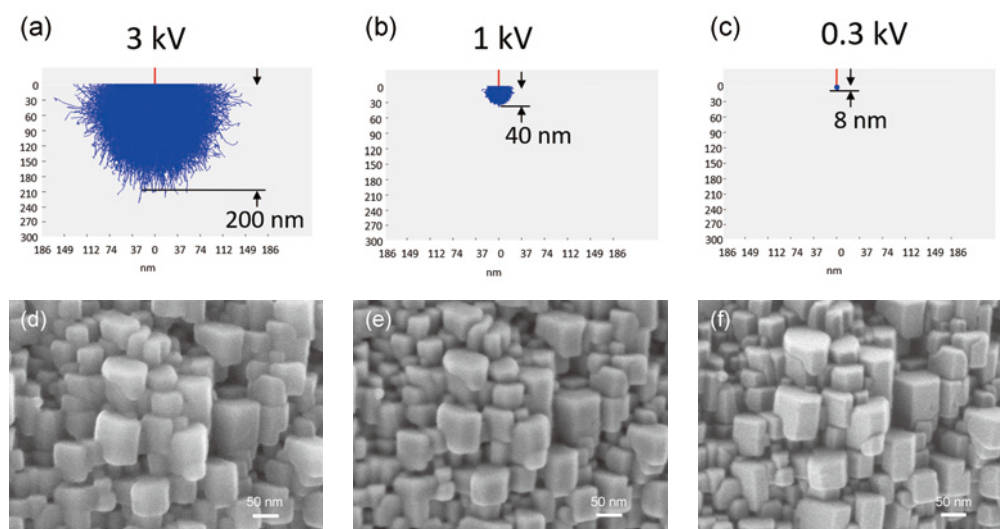
area near the surface, which allows a clearer imaging of the nanostructure details on the sample surface (Figure 2f). This provides the theoretical basis for the invention of low-voltage high resolution SEM.

Thanks to the advent of the low-voltage field emission scanning electron microscope, the high-resolution imaging of zeolite surface is no longer a difficult problem. As shown in **Figure 3**, the crystal on focus is a zeolite Y sample. It has a well-defined octahedron morphology, which is characteristic for the FAU type zeolites (Figure 3a). The three-dimensional shape of the crystal is vividly recorded thanks to the large depth of field. In addition, many details are presented. The corners and edges of the crystal are clearly distinguishable.

Also, the growth steps on the top of crystal surface can be identified (Figure 3b). In addition, since the sample was used directly for image formation without covering it in advance with a layer of conductive nano-particles (Pt or C), and the low-accelerating voltage is very appropriate for the high-resolution surface observation without causing damages of the crystals, the observed surface morphology can be considered as the intrinsic surface of zeolite crystals with confidence.

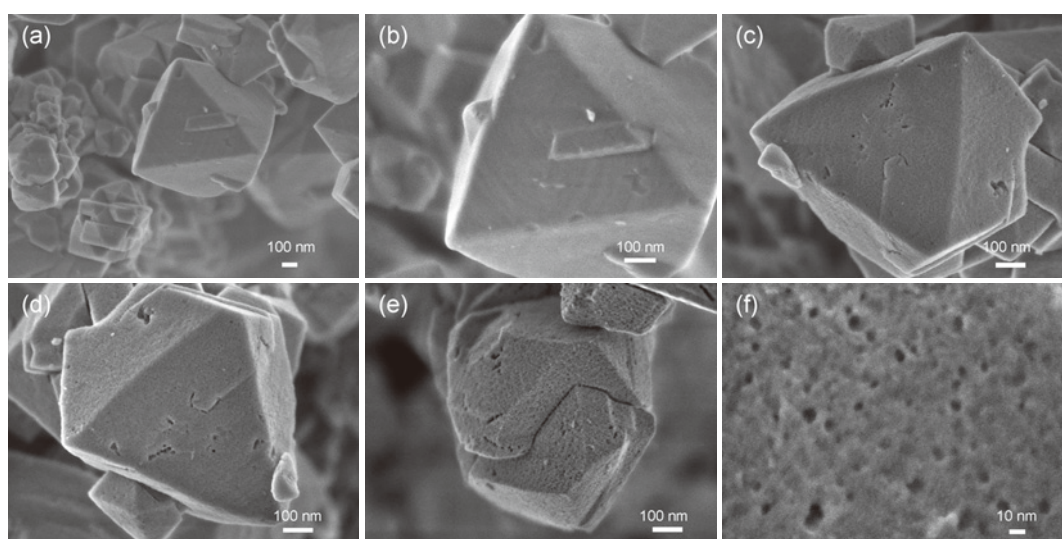
Therefore, a change in surface morphology is a vivid evidence demonstrating the impact of the applied treatment on zeolite crystals. This is exemplified by the SEM observation of the FAU-Y zeolite surface before and after the NH_4F treatment. Namely, the NH_4F treated sample shows apparently a rougher

Fig. 2



(a-c) Simulation result of interaction volume of incident electrons in the silicon using Monte Carlo method (Calculated as SiO_2). (d-f) The SEM images of a ZSM-5 zeolite sample obtained at different accelerating voltage (d: 3 kV, e: 1 kV, f: 0.3 kV). The ZSM-5 zeolite sample, denoted as MFI-1, was synthesized according to the procedures described in reference [2].

Fig. 3



The SEM images at lower (a) and higher (b) magnifications showing the deep view field and high quality of the images. The sample used for demonstration is a FAU-Y zeolite sample with a characteristic octahedral plane morphology. In Figure 3b, the growth layer on top of the (111) crystal plain can be seen clearly. (c, d) The observation of the same crystal from different orientation. (e, f) The SEM images at low (e) and high (f) magnification showing the intensive dissolution of zeolite crystals in NH_4F medium: (e) The intensive removal of framework atoms from crystal surface and the preferential dissolution of zeolite crystals along extended interface between intergrown crystal; (f) Surface imaging of zeolite crystal at ultra-high magnification showing the presence of ultra-small nanopores.

surface than the parent, untreated sample, in addition to the appearance of surface craters of varied size and morphology (Figure 3c). The imaging quality can be improved further, through the adjustment of the orientation of the sample stage (Figure 3d), and the optimization of the operation parameters including, but not limited to, the magnification (Figure 3e, f). In the example shown in Figure 3f, the fine adjustment of the instrument allows the observation of surface with a magnification as high as 500 K. At this magnification, nanopores on zeolite surface smaller than 10 nm can be observed directly.

Recently, JEOL has developed a new type of FE-SEM, the latest low-voltage field emission scanning electron microscope so called JSM-IT800<SHL>, equipped with a high contrast in lens detection system which is very appropriate for zeolites imaging in super low aberration compound objective lens. The sophisticated high contrast detection system contains the following advanced parts. First, the application of a negative bias voltage to the zeolite samples on the sample stage. This adjustment can further reduce the effect of chromatic aberration caused by the primary electron beam, improving the detection efficiency. Second, the employment of a new combined objective lens consisting of magnetic and electrostatic lenses (Figure 4a) to the observation. With this new compound type objective lens system, one could produce a small probe size, thus providing higher resolution. In addition, the choice of detector is also important for the observation of zeolites. Various electrons emitted from the sample could be selectively detected by different detectors (Figure 4a), UED (upper electron detector) and UHD (upper hybrid detector) equipped in this latest low-voltage field emission scanning electron microscope.

Using this new SEM, a set of high contrast images with a vivid stereoscopic effect were obtained for a model ZSM-5 zeolite with a characteristic mosaic surface (Figure 4b). According to the position of the detector, as shown in Figure 4a, the UED could detect the low energy electrons which produces the edge contrast and the voltage contrast on the image (Figure 4b). While the UHD located in the objective lens could detect the high energy electrons which present the topography of samples without any effect of charge (Figure 4c). Moreover, applying a -5 kV bias voltage on the zeolite sample, one could make an accelerated beam decelerate just before reaching the sample surface, enabling a high-resolution observation. As a result, the

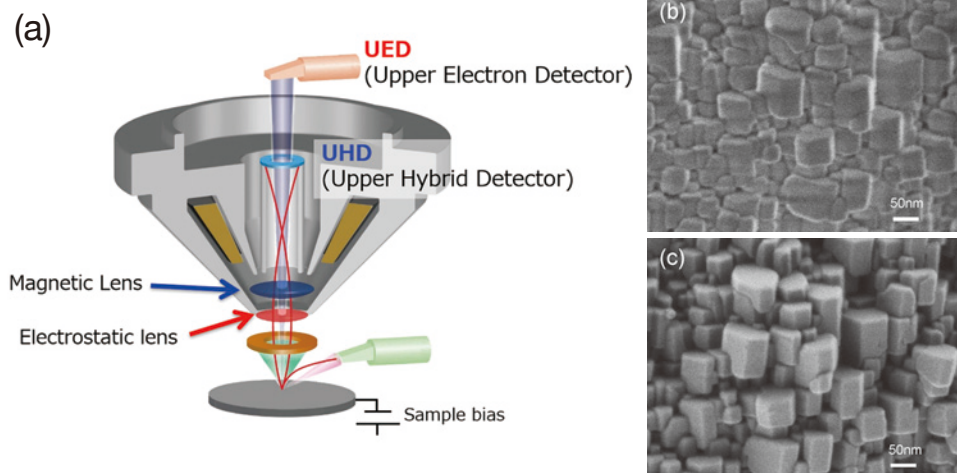
ZSM-5 zeolite is presented as a nano aggregate made of closely assembled nano-cubes (Figure 4c). This observation is consistent with our synthesis knowledge that, indeed, there should be nanomosaic domains with well-defined shapes overlapping each other at this stage of crystallization.

Taking the advantage of the high-resolution imaging capacity, the microscopy can be developed as a convenient tool for the intensive inspection of crystal morphology. This is very helpful for the study of zeolite crystallization and dissolution behaviors that involve multiple intermediate samples of different stage. Taking the dissolution of a commercial ZSM-5 zeolite sample (MFI-2, experimental part) in NH_4F solution as an example, the representative images recording the process of anisotropic crystal dissolution behavior is shown in Figure 5. A glance of the crystals which lie on the sample stage is usually the first operation. It is not time-consuming, but is very helpful for the identification of the crystals of interest for further observation. After the preliminary screening, a more detailed inspection of different crystal planes can be carried out, then the collected images can be arranged according to the length of etching time for the comparison purpose. Based on these vivid observations, a progressive dissolution of zeolite crystals leading to the birth and propagation of secondary porosity can be documented. This is very helpful for the screening of samples for deeper study of zeolite dissolution mechanisms and the associated crystallization mechanism-dissolution behavior inter-correlations, as shall be seen below.

2) Insight into the secondary pores in zeolite crystals: The powerfulness of TEM imaging

As described above, a SEM equipped with a high-resolution imaging system is very appropriate for the observation of the outer surface of zeolite crystals. Especially, the direct observation of the post-synthesis engineered pores from crystal surface is a strong evidence showing that, indeed, there is an impact of the implemented chemical etching on zeolite crystals, as the intrinsic micropores of zeolites is too small to be observed by SEM. On the other hand, however, only to see the presence of pores is not enough. One would wonder how many pores are there inside the crystal. In addition, the size, morphology, connectivity, tortuosity, spatial distribution..., all of the information are important for the ultimate goal of the

Fig. 4



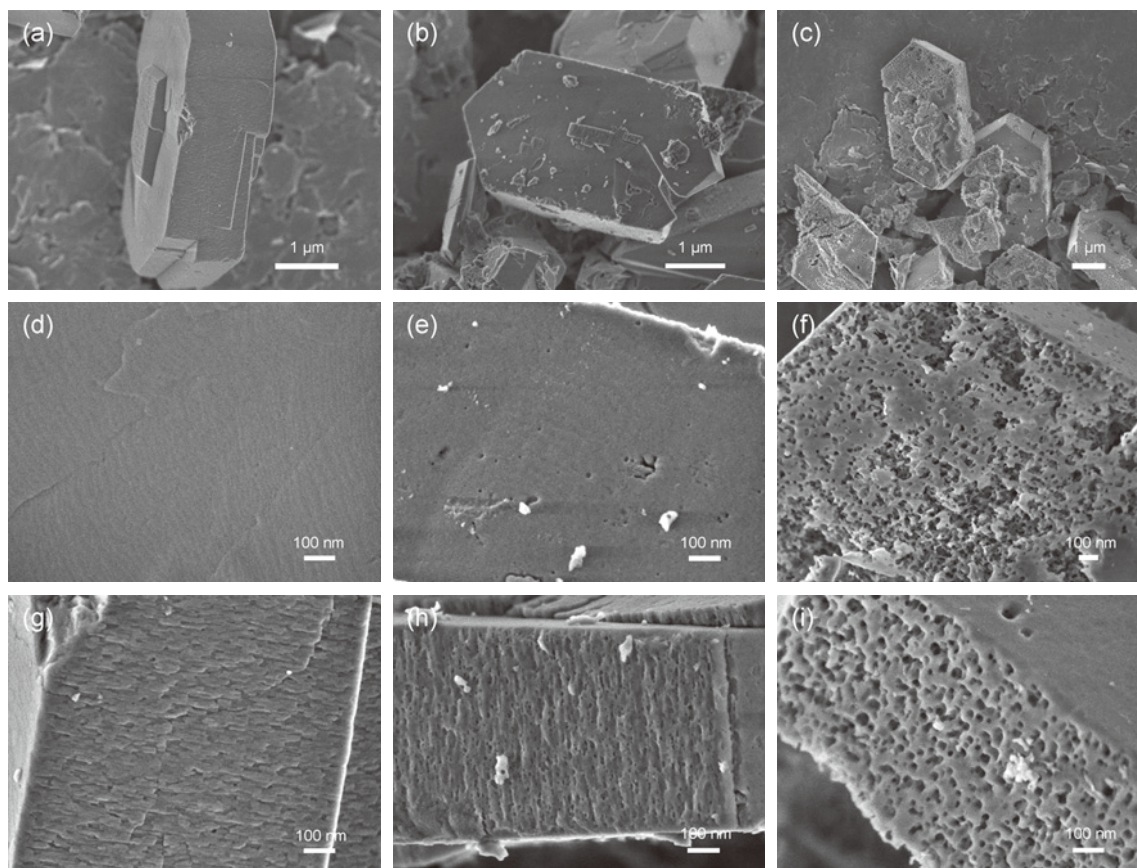
(a) A schematic presentation of objective lens and detection system of JSM-IT800SHL. (b) SEM image of ZSM-5 obtained with the UED detector. (c) SEM image of ZSM-5 obtained with the UHD detector.

comprehensive understanding of the engineered porosity.

Normally, TEM is the technology of choice for the understanding of the secondary porosity in the inner part of zeolite crystals. In the present work, two examples are presented to show the powerfulness of this fantastic technology. The first example is the identification of the birth and propagation of mesopores at the 2 nm scale (Figure 6). While the presence of such mesopores induced by NH_4F etching is confirmed by both SEM (Figure 3f) and TEM (Figure 6a), the high-resolution documentation of the formation of mesopores and their connection from the very

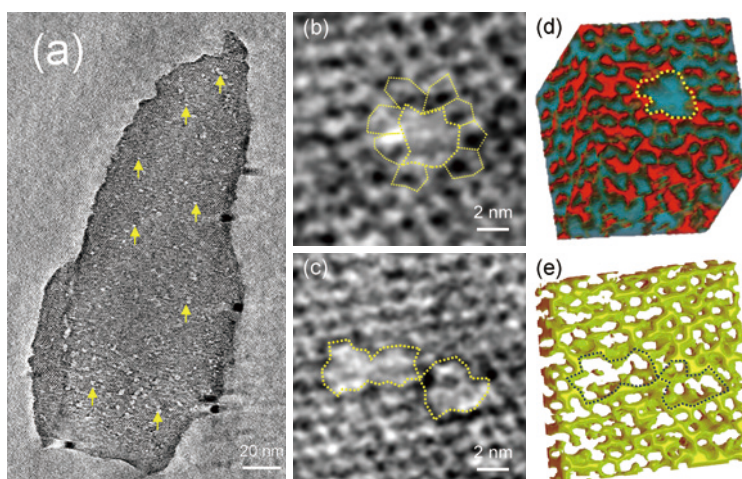
beginning is important for the interpretation of the mesopore formation mechanism. For this purpose, a thin specimen of about 40 nm was prepared by ultramicrotomy of a hierarchical zeolite Y prepared by a mild NH_4F etching [3]. The high-resolution 3D reconstruction shows some of the zeolite cages and their merging resulting in the formation of larger mesopores (Figure 6b, d). The enlargement of the mesopores seems to appear when two or multiple mesopores merge due to the close proximity (Figure 6c, e). With this information in hand, we can conclude with confidence that the mesopore formation in a NH_4F treated

Fig. 5



Time-resolved study of the dissolution behavior of zeolite crystals in NH_4F solution using low-voltage high-resolution SEM in the absence of sample coating.

Fig. 6



(a) Electron tomography slice of a hierarchical zeolite Y showing the presence of many small mesopores. (b, d) High-resolution view of a mesopore created via the merging of few microporous cages (left) and 3D representation of a mesopore and the surrounding in the zeolite crystal (right). (c, e) High-resolution view of a pair of three mesopores merged (left) and 3D representation of mesopores and their surrounding in a zeolite crystal (right).

zeolite Y sample starts from the dissolution of the walls between neighboring micropores.

In the case of MFI type zeolite, however, the dissolution of zeolite framework and the corresponding mesopore formation is caused by the preferential dissolution of the mosaic domains hidden inside zeolite crystals. This is quite different from the situation in the case of zeolite Y. The different dissolution behavior can be identified from the SEM images. Namely, the size of the mesopores in the case of ZSM-5 zeolite is much larger (Figure 5), and the shape more regular, than that of the FAU-Y zeolite (Figure 6). Now that the size and shape of the pores left by partial removal of framework atoms matter, an unambiguous identification of the shape and orientation of the pores is important. Again, high resolution TEM, in combination with tomography techniques, showed its ability in structure characterization. Here the showcase is a NH_4F treated derivative of MFI-2 (See experimental part). Most of the pores in this sample are isolated (Figure 7A). A very interesting observation is that these isolated pores exhibit a rectangular shape and a uniform orientation (Figure 7C, D). Occasionally, neighboring pores connect by the dissolution of a relatively thin dividing wall (Figure 7B). The combination of TEM and tomography was used for the analysis of the 3D shape and spatial orientation of the pores, and the 3D reconstructions (Figure 7C, E) show either a cubic or diamond shape, pointing to the fact that the mesopores has an anisotropic morphology. As a result, the specific shape of the

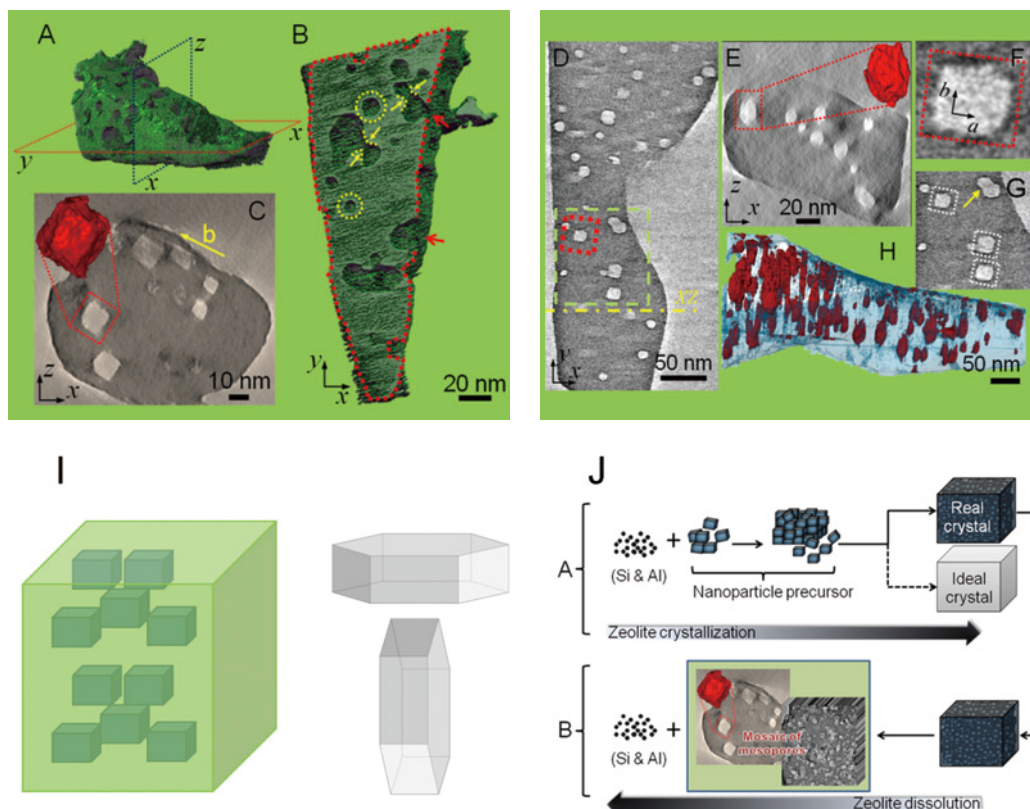
pores from a 2D perspective depends on the angle of observation (Figure 7I). Based on these structural analyses, the mechanisms for zeolite crystallization and dissolution can be deduced.

3) Imaging zeolite architecture by scanning electron microscopy: when physical and chemical etching meet

Many structural information beneath the surface of zeolite crystals, such as the morphology of mesopores and their connectivity and spatial distribution, are of great importance and may guide the optimization of zeolites for applications. While TEM is advantageous for the characterization of structural details beneath the outer surface of zeolite crystals, it is not the only method of choice for such a purpose. In the following part, the applications of low voltage FE-SEM for the characterization of the inner architecture of zeolites were presented.

As the first example, ultra-high-resolution FE-SEM imaging technology was applied to observe the cross-section of a NH_4F treated zeolite Y sample, with the purpose of having more information about the internal architecture of the secondary porosity beneath the outer surface of zeolite crystals. In order to have a better resolution of the cross-section at high magnification, the sample was first coated with a ~ 10 nm thick Osmium (Os). Then the cross-section of the Os-coated sample was prepared by Ar ion sputtering (physical etching) following the procedures depicted in Figure 1a. Then the obtained sample

Fig. 7

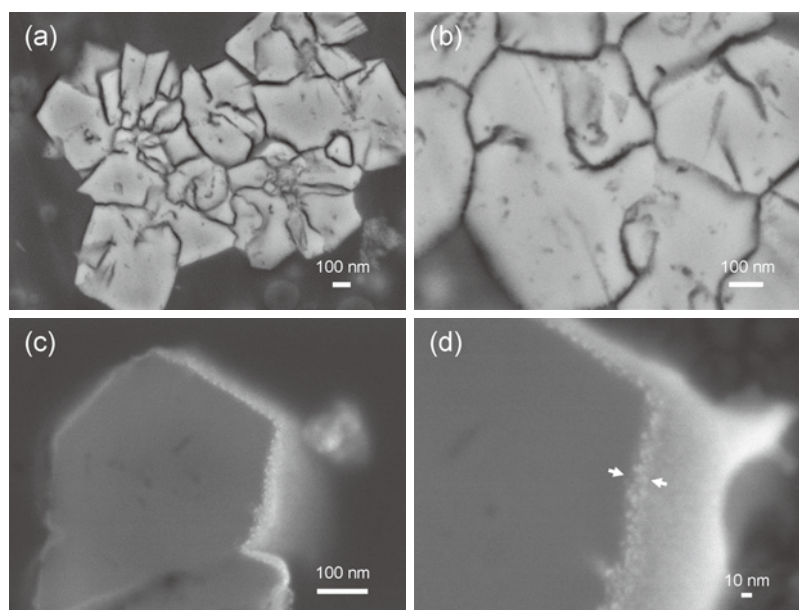


3D models of zeolite grains reconstructed by electron tomography and the slices clipped through the models. (A) 3D model of a NH_4F treated MFI-2, (B) xy and (C) xz slices clipped through the reconstructed volume taken at the positions highlighted in (A). Yellow circles in (B) show the "trapped" isolated mesopores and the yellow arrows highlight the removal of a wall between neighboring pores, while red arrows indicate mesopores with direct access to the external surface of a zeolite grain. The red inset in (C) reveals the cubic 3D shape of the pore. (D) XY slice clipped through the center of the 3D model of the NH_4F treated MFI-2. The yellow line in (D) shows the position of the XZ slice presented in (E). The red inset in (E) shows the 3D morphology of the pore highlighted in rectangle. (F, G) cropped regions of the XY slice highlight the rectangle pores. (H) Snapshots of the 3D model acquired at XY direction (zeolite body in transparent blue, pores in red). (I) The shape of the pores in 2-dimension depends on the angle of observation. (J) Zeolite growth process and its dissolution in fluoride medium revealing the mosaic structure of zeolite crystals.

was studied in detail using an ultrahigh-resolution FE-SEM. This characterization results in two important observations. First, it reveals an overall highly fragmented pattern suggesting the separation of intergrown crystals along the extended boundaries (Figure 8a, b). Although this can be speculated based on a classical surface imaging showing the splitting of intergrown crystals (Figure 3e), the direct observation of the cross-section shows unambiguously the presence of multiple cracks penetrated deeply into zeolite crystals. Most of these cracks, with an estimated width of ca. 50 nm, are interconnected with each other. As a result of such cross-linked pores in all directions, the aggregated crystals are formally divided into nanosized domains (Figure 8a, b). The second important finding is about the spatial

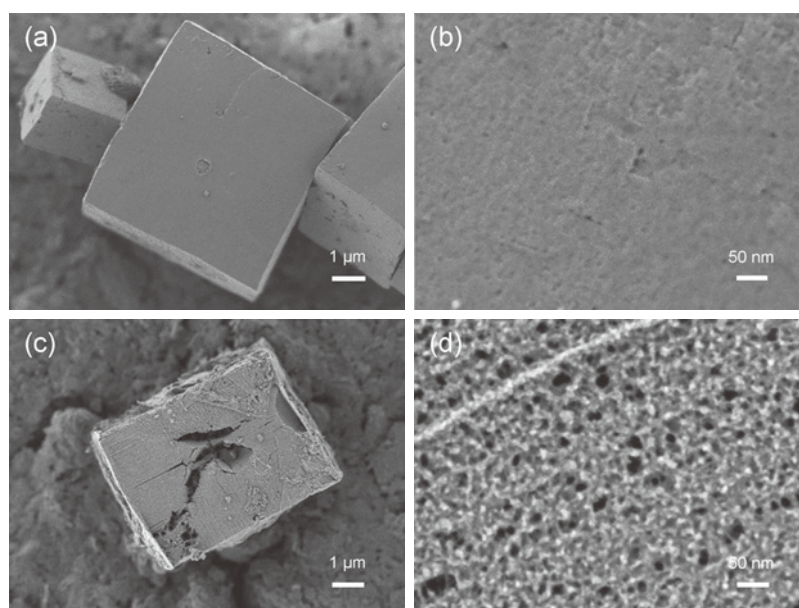
location of the small mesopores. Namely, a further careful inspection of the cross-section at ultra-high magnification using a LABE (low angle backscattered electrons) model confirmed the presence of small mesopores, but these mesopores are distributed only at the rim of zeolite crystals (Figure 8c, d). The thickness of this surface mesoporous layer is homogeneous, ca. 20 nm thick. The inner part of zeolite crystals is essentially microporous in nature. LABE may escape from near surface of sample. In addition, the voltage of the primary electron energy used as landing voltage was at 3 kV. In this case, the information of images is collected from the near surface. Thus, this method is useful to take fine details of sample without the interference of inner information.

Fig. 8



The ultra-high-resolution FE-SEM images of the cross-section of the NH_4F treated zeolite Y with Os-coating. In Figure 8c and d, Os was penetrated in mesopores. The presence of Os particles in the mesopores was indicated with white arrows.

Fig. 9



Morphology, size and surface features of (a, b) parent and (c, d) NH_4F treated SAPO-34 samples.

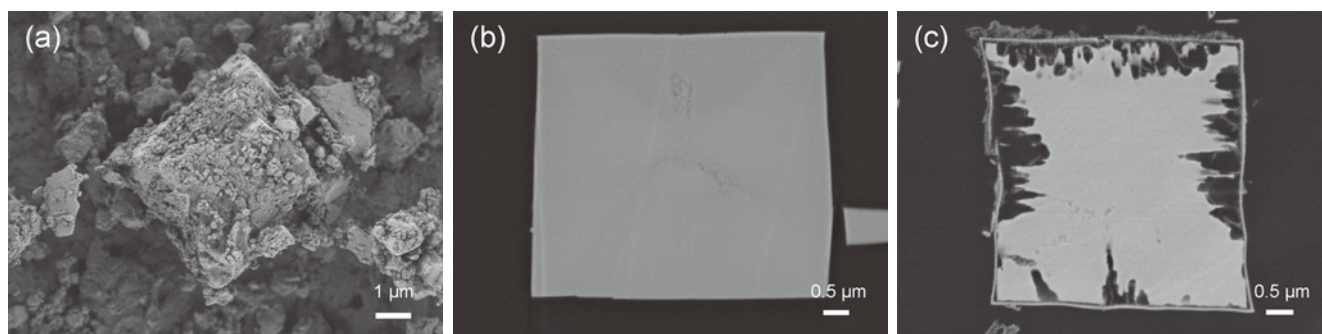
In another example, the parent and NH_4F treated SAPO-34 were used as model materials. The parent SAPO-34 crystals exhibit a cubic morphology and a size larger than $1\ \mu\text{m}$ (Figure 9a). The seemingly flat surface is essentially uneven under high magnification imaging (200 K) at low voltage (Figure 9b). The morphology of the NH_4F treated SAPO-34 crystals is shown in Figure 9c. The high-resolution image reveals the remarkable rough surface of the crystals with a dense distribution of mesopores (Figure 9d). Based on this observation, one may suggest that the sample contains mesopores. Again, the samples were physically “etched” with an Ar ion beam cross sections polisher (CP). In contrast to the irregular interface obtained by crashing samples with mortar (Figure 10a), the CP cross sections of the parent SAPO-34 exhibit flat surfaces without any deposition (Figure 10b). The cross-section image of this sample shows a specific X-shape internal structure without obvious pores or defects. In contrast, the NH_4F etched sample exhibits framed pattern of butterfly-shape (Figure 10c). Between the frame and the butterfly-shape there are many macroporous holes, suggesting that the inner part of the SAPO-34 crystals is preferentially dissolved, while the outermost shell is preserved. The information obtained is different from the one interpreted from the classical imaging of the outermost shell, such as pore size, morphology, density, and uniformity of spatial distribution.

In particular, when magnifying the images of surface and cross section to compare the “mesoporosity” from different perspective in detail (Figure 11), the high mesoporosity of NH_4F treated SAPO-34 interpreted from Figure 9d seems to be far from a representative one. Namely, the dense mesoporous area (Region A) represents only a thin layer on the surface. Therefore, the comparison of the surface and cross section images allows a more comprehensive understanding of the secondary porosity in the NH_4F treated SAPO-34.

4) Imaging zeolite architecture by scanning electron microscopy: observing chemical etching quasi-in situ

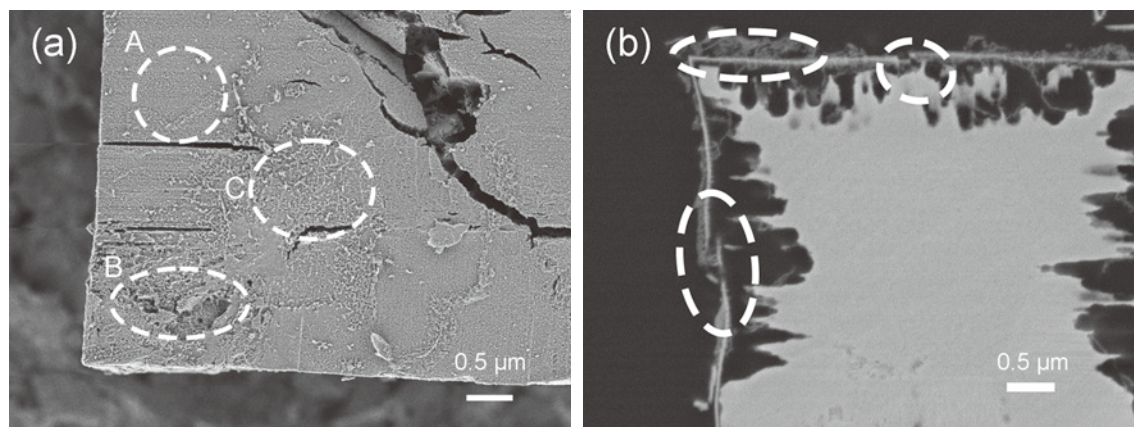
The dissolution behavior of zeolite crystal is intimately related to the engineering of hierarchical porosity inside zeolite frameworks. So, a vivid tracking of crystal dissolution process is of great interest. Previously, the time resolved observation of surface topography changes with chemical etching was examined by atomic force microscopy [4]. Recently, we reported the first example to follow the dissolution of SAPO-34 crystals by cross section imaging using a low vacuum backscattered electron detector (LV-BED). The observation at low-vacuum reduces the effect of charge electrons through introducing N_2 gas into the chamber, while keeping the column of SEM at

Fig. 10



Cross section SEM images of parent and NH_4F treated SAPO-34 samples: (a) Mortar crashed parent SAPO-34, (b) CP cross section of parent SAPO-34, and (c) CP cross section of NH_4F treated SAPO-34 sample.

Fig. 11



Comparison of magnifying images of (a) particle surface and (b) cross section of NH_4F treated SAPO-34 samples; A, B, C show dense mesopores area, macro defects area and nanofibers formed.

high vacuum through an orifice control. This is because N_2 gas irradiated by an electron beam could be ionized and then reacts with charge electrons, then a clear image without charge effect can be obtained by the LV-BED attached on the orifice control.

To investigate the effect of NH_4F etching, the cross section of the parent SAPO-34 under treatment is studied (Figure 12). The backscattered electron images of cross section before and after etching was recorded immediately after the sample preparation (Figure 12a and b). The comparison of the images shows unambiguously that the treated cross section exhibits an obvious spatially inhomogeneous etching (Figure 12b). Combining with the EDS analysis (Figure 12c), the outermost and Si-rich shell is shown to be preserved, while the etching starts from the parts below the shell. This is the first observation reporting on the initial dissolution during the NH_4F etching of SAPOs. Also, this is the first observation revealing that some inner part of SAPO-34 is more vulnerable than the outermost shell of the crystals. As a result, the inner parts are preferentially removed by NH_4F etching.

Conclusion

In this work, a brief summarization of our recent practices in the characterization of zeolites using high-resolution low voltage FE-SEM was presented. The unique advantage of the technical combination of high resolution and low voltage in the imaging of zeolite crystals without the interference of surface conductive nanoparticles deposit was elaborated. The powerfulness of the combination of high-resolution imaging with physical and chemical etching in characterization of the inner part of zeolite crystals by scanning electron microscopy was highlighted. While the SEM, EDS, ion beam polishing and NH_4F etching are commonly available, the creative combination of these technologies allows us to explore the internal structure of zeolite crystals more appropriately. SEM is routinely used only for crystal size and morphology observation. Now with

the comprehensive combination of high-resolution low voltage imaging and cross section preparation technologies, we are able to observe the hidden meso- and microporosity in a much wider view field than the classical TEM characterization. Moreover, we illustrated that the high solid angle EDS analysis for the cross section of zeolite before and after chemical etching is the very effective method to investigate the structure change of zeolite quasi in-situ.

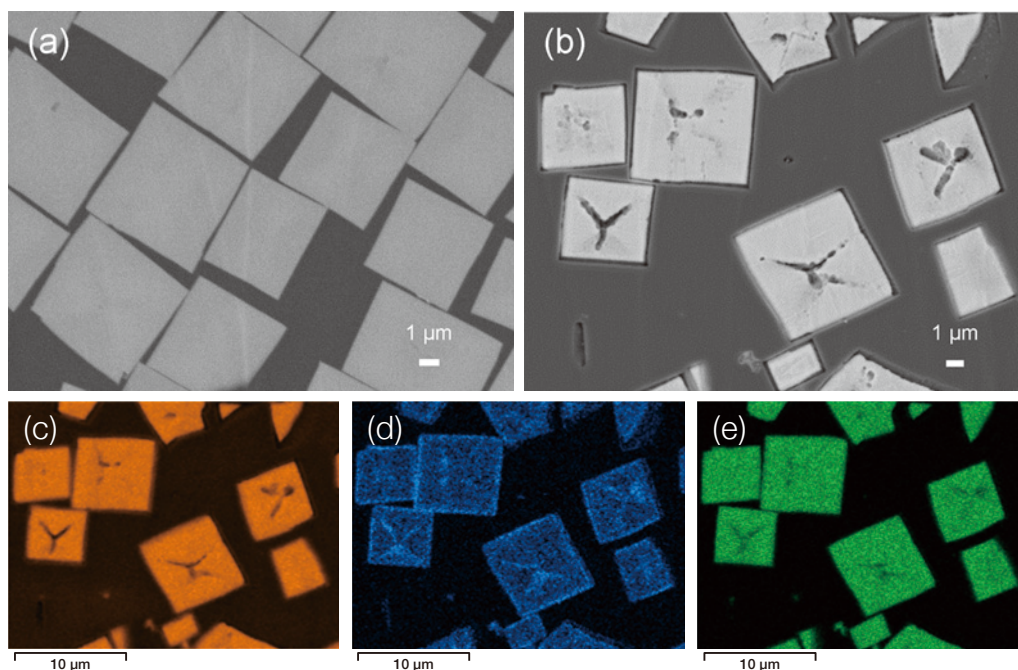
Acknowledgements

We acknowledge the financial support from the National Natural Science Foundation of China (22178389).

References

- [1] Z. Qin, Z. You, K.N. Bozhilov, S.K. Kolev, W. Yang, Y. Shen, X. Jin, J.-P. Gilson, S. Mintova, G.N. Vayssilov, V. Valtchev, Dissolution Behavior and Varied Mesoporosity of Zeolites by NH_4F Etching, *Chemistry – A European Journal*, **28** (2022) e202104339.
- [2] Y. Shen, Z. Qin, S. Asahina, N. Asano, G. Zhang, S. Qian, Y. Ma, Z. Yan, X. Liu, S. Mintova, The inner heterogeneity of ZSM-5 zeolite crystals, *Journal of Materials Chemistry A*, **9** (2021) 4203-4212.
- [3] Z. Qin, S. Zeng, G. Melinte, T. Bučko, M. Badawi, Y. Shen, J.-P. Gilson, O. Ersen, Y. Wei, Z. Liu, X. Liu, Z. Yan, S. Xu, V. Valtchev, S. Mintova, Understanding the Fundamentals of Microporosity Upgrading in Zeolites: Increasing Diffusion and Catalytic Performances, *Advanced Science*, **8** (2021) 2100001.
- [4] K.N. Bozhilov, T.T. Le, Z. Qin, T. Terlier, A. Palčić, J.D. Rimer, V. Valtchev, Time-resolved dissolution elucidates the mechanism of zeolite MFI crystallization, *Science Advances*, **7** (2021) eabg0454.

Fig. 12



SEM images of the cross section of SAPO-34 crystals (a) before and (b) after NH_4F treatment and (c) element distribution maps for O, Si and Al. Two EDS detectors (170 mm² sensor area, Ultim Max Oxford) and one windowless type EDS detector (100 mm² sensor area, Ultim Extreme Oxford) were used to obtain the element distribution maps.

Low-Dose Atomic-Resolution Observation of Beam-Sensitive Materials via OBF STEM Imaging Technique

Kousuke Ooe^{1,2}, Takehito Seki^{2,3}, Yuji Kohno⁴, Akiho Nakamura⁴,
Yuichi Ikuhara^{1,2}, Naoya Shibata^{1,2}

¹Nanostructures Research Laboratory, Japan Fine Ceramics Center

²Institute of Engineering Innovation, the School of Engineering, the University of Tokyo

³PRESTO, Japan Science and Technology Agency

⁴JEOL Ltd.

With the advent of aberration correction technology, (Scanning) transmission electron microscopy (S/TEM) has been a powerful technique for characterizing materials and devices. However, observation of beam-sensitive materials, which are easily damaged by electron irradiation, is one of the most challenging issues. Herein, we developed the optimum bright-field (OBF) STEM technique for observing these samples at very low-dose. In this article, we briefly summarize the theoretical aspects of OBF STEM, and introduce its applications for a lithium-ion battery material and an organic molecular crystal.

Introduction

Scanning transmission electron microscopy (STEM) performs a scan of a converged electron probe across the sample and detects the transmitted electrons to form raster images. With the advent of aberration correctors, STEM can converge an electron beam into the atomic size and directly observe local atomic structures inside the sample. Nowadays, STEM is a very powerful structural analysis tool for materials science, and is actively used to characterize defects and interfaces in metals, semiconductors, and ceramics. In STEM observations, however, electron irradiation damage often becomes problematic due to the strong interaction between the illuminated electrons and the sample. Especially, porous materials (zeolites and metal-organic frameworks), battery materials, and polymer materials are known as beam-sensitive materials because their structures are easily damaged by electron irradiation. For the observation of these materials, a low-dose condition is essential. However, because shot-noise becomes significant under low-dose conditions, the signal-to-noise ratio (SNR) becomes poor, and detailed atomic structure analysis becomes extremely difficult. Thus, the irradiation damage and SNR are in an inevitable trade-off relationship in the STEM observation of beam-sensitive materials.

For low-dose atomic-resolution imaging of the beam-sensitive materials, high-resolution TEM (HRTEM) has been utilized for many years. In HRTEM, atomic structures are observed via phase contrast, which is obtained by the interference of transmitted and diffracted electrons under the parallel-beam illumination condition. Since HRTEM uses most of the

illuminated electrons to form images, this method can achieve high SNR images and has been applied to high-resolution observations of beam-sensitive materials [1]. However, because the HRTEM image contrast strongly depends on the defocus and sample thickness, it is necessary to perform systematic image simulations to interpret atomic structures from the image. On the other hand, aberration-corrected STEM has been recently becoming popular for atomic-scale observations due to the straightforward interpretability of the image contrast. Especially high angle annular dark-field (HAADF) imaging can offer very easily interpretable contrast nearly proportional to the square of atomic number (Z), and annular bright-field (ABF) imaging can simultaneously visualize heavy and light elements, which are now indispensable techniques to analyze local atomic structures [2]. Nevertheless, these STEM techniques use single annular detectors on the bright/dark field regions and detect only a fraction of the transmitted/scattered electrons, making the application for beam-sensitive materials challenging due to the low imaging efficiency.

Under these circumstances, next-generation STEM detectors such as segmented/pixelated detectors have been reported since around the 2010s [3, 4]. These detectors have multiple detection areas and record the intensities of transmitted/scattered electrons on each segment/pixel. Thus, multiple STEM images are acquired for each detection area by a segmented detector, and two-dimensional diffraction patterns are recorded at each probe raster by a pixelated detector. These detectors can use the information about azimuthal scattering angle, which is neglected in the conventional methods because the intensity is rotationally averaged on the single annular detectors. Due to

this improvement, novel imaging techniques such as differential phase contrast (DPC) imaging for electromagnetic field observations [5, 6] and electron ptychography for phase imaging [7] are intentionally investigated and applied to materials science researches.

Herein, using these next-generation STEM detectors, we newly developed a highly efficient imaging technique called optimum bright-field (OBF) imaging [8]. OBF imaging can achieve approximately two orders of magnitude higher dose efficiency than ABF imaging by using a segmented/pixelated detector. Furthermore, OBF images are obtainable in real-time as well as the conventional techniques such as HAADF and ABF imaging. Thus, operators can tune aberrations and select the field-of-view (FOV) even under low-dose conditions by referring to high contrast OBF images, which is difficult to do by referring to conventional STEM images due to their poor SNR. In this paper, we summarize the theoretical background of OBF STEM imaging and its applications to atomic-resolution observations of beam-sensitive materials.

Theoretical background of OBF imaging

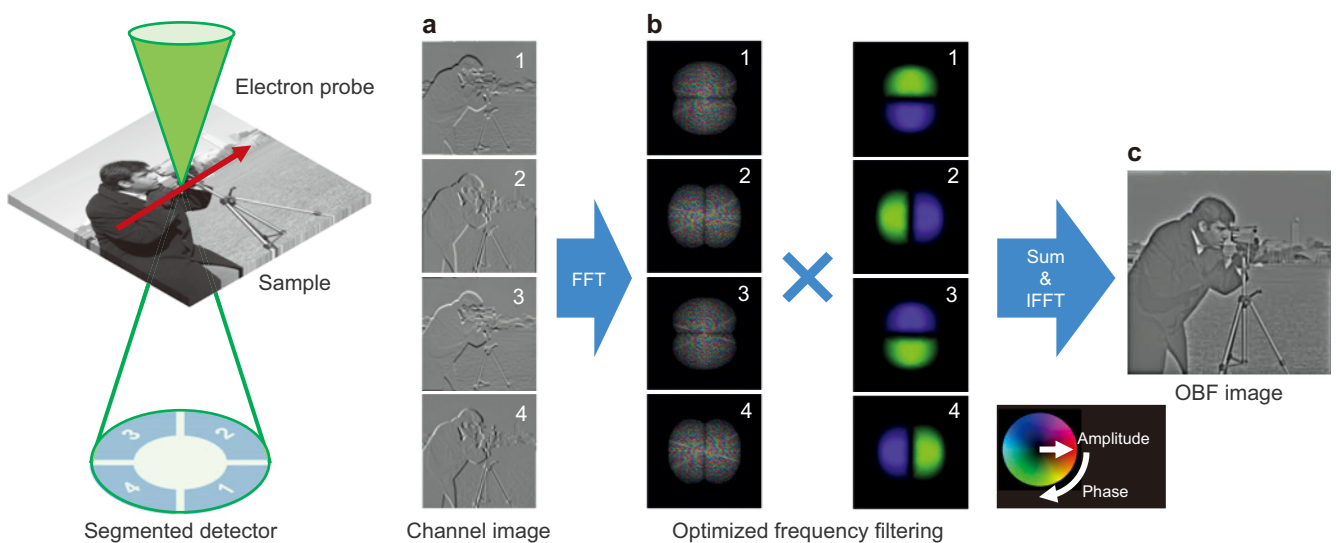
Figure 1 shows a schematic illustration of the optical system and reconstruction workflow used in OBF STEM. For simplicity, we show the case of OBF STEM using a four-segmented detector. Using the segmented detector, we can simultaneously record the transmitted electron intensity integrated in each segment as multiple STEM images. Thus, in the case of a segmented detector, the obtained image contrast reflects the shape and configuration of a corresponding detector segment whereas an annular detector records a single STEM image. The properties of image contrast from each segment can be analyzed via STEM phase contrast transfer functions (PCTFs). Under the

weak phase object approximation (WPOA), the STEM image intensity obtained from the j th segment is written as follows;

$$I_j(\mathbf{r}) = d_j + \mathcal{F}^{-1}[\sigma V_{\text{prj}}(\mathbf{q})\beta_j(\mathbf{q})]$$

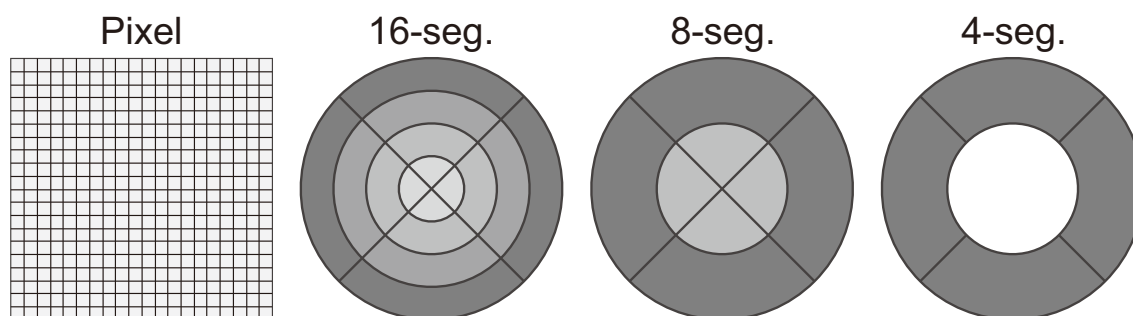
where \mathbf{r} , \mathbf{q} , d_j , \mathcal{F}^{-1} , σ , $V_{\text{prj}}(\mathbf{q})$, $\beta_j(\mathbf{q})$ are two-dimensional real space coordinate and its conjugate spatial frequency coordinate, background intensity of the j th segment, inverse Fourier transform operator, interaction constant, Fourier coefficients of the sample projected potential, and PCTF for the j th segment, respectively. Under WPOA, the second term represents the obtained image contrast, which means that the image contrast is given as the projected potential $V_{\text{prj}}(\mathbf{q})$ band-pass filtered by $\beta_j(\mathbf{q})$. The PCTF $\beta_j(\mathbf{q})$ is given by optical parameters such as accelerating voltage, convergence angle, lens aberration, and detector configuration. Therefore, this equation indicates how the sample information $V_{\text{prj}}(\mathbf{q})$ is modulated by the microscope and then transferred into the image contrast. Thus, by calculating the PCTFs for each segment of a segmented detector by the optical parameters, we can estimate the image contrast as a function of spatial frequency \mathbf{q} . Additionally, according to the recently-developed noise evaluation theory in STEM [9], the noise level of each image from the segmented detector is proportional to the square root of the background level $\sqrt{d_j}$. d_j is equal to the image intensity in the absence of a specimen (i.e., vacuum area) and proportional to the area of each detector segment. Therefore, once the shape and configuration of a detector segment is determined, both image contrast and its noise level can also be calculated, which is very important for evaluating the imaging efficiency under the low-dose condition. Herein, we theoretically derived a reconstruction technique by weighted summation of the STEM images simultaneously obtained from each detector segment with weighting coefficients optimized to maximize the

Fig. 1 Schematic illustration of the optical system and reconstruction workflow in OBF STEM.



(a) A sample is raster-scanned by a converged electron probe and the segmented detector detects transmitted electrons. In the segmented detector, multiple channel images are simultaneously obtained from each segment. (b) The Fourier components of each channel image are calculated by performing the fast Fourier transform. Complex spatial frequency filters are applied to the Fourier components of each channel image, which are calculated as a function of STEM optical parameters such as an accelerating voltage and convergence semiangle. (c) The filtered Fourier components are summed up and then inverse Fourier-transformed to obtain the OBF image. Adapted from Ref. [23] with permission.

Fig. 2 Examples of STEM detectors used in OBF imaging.



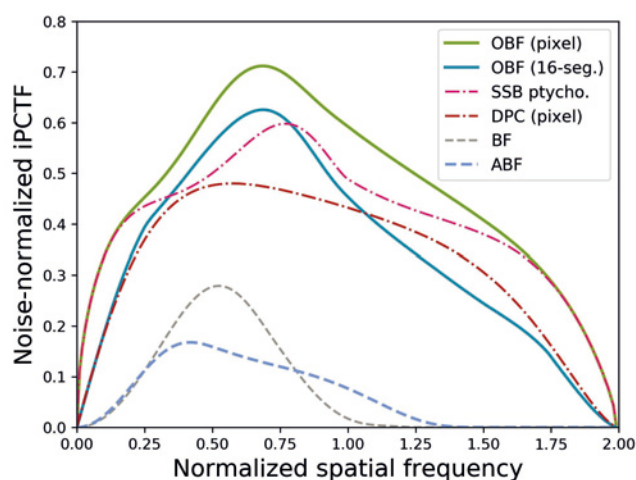
In OBF imaging, images can be reconstructed using various types of segmented/pixelated detectors. Adapted from Ref. [23] with permission.

SNR (theoretical details are described in [8]). The weighting coefficients are calculated as a function of spatial frequency q . In OBF STEM, therefore, this weighting process is performed as frequency filtering to Fourier-transformed STEM images from each detector segment as shown in Fig. 1(b). After this process, all channel images are summed up and inverse Fourier-transformed to obtain the OBF image as schematically shown in Fig. 1(c). While we have shown the OBF reconstruction process in the case of simple four-segmented detector in Fig. 1, OBF imaging is applicable for arbitrary configurations of segmented/pixelated detectors. **Figure 2** shows several examples of segmented/pixelated detectors, where the weighting frequency filters needed for the OBF reconstruction can be calculated respectively. Furthermore, this filtering process can also be performed by convolution calculation in real space without Fourier transformation. By approximating this spatial filtering, OBF images are reconstructed as *live image* in sync with STEM probe scanning. In usual STEM observations, operators refer to the live image and tune the observation conditions such as FOV and lens aberrations in real time. Under the low dose condition, however, this process becomes significantly difficult because the SNR of live images becomes poor, and finely tuned experimental results cannot be obtained. On the other hand, the operators can observe the high-SNR OBF images in real time even under low dose conditions, which is very useful in practical experiments. It is noteworthy that all experimental OBF images shown in this article are obtained by using the *live* OBF imaging function.

Light element imaging by OBF STEM

As an application of OBF STEM, we performed atomic-resolution observation of a lithium-ion battery (LIB) material that contains lithium, an ultra-light element. LIBs are utilized for a wide range of applications due to their high energy density, and degradation behavior of battery properties during the charge/discharge process is crucial to understanding to improve the battery performance. Since the LIBs are charged/discharged via lithium migration associated with lithiation/delithiation, it is highly demanded to analyze the behavior of lithium ions at the atomic scale. In previous studies [10, 11], the direct observations of lithium sites were conducted via ABF imaging. However,

Fig. 3 Dose-efficiency comparison between different STEM imaging techniques via noise-normalized iPCTFs.



The iPCTFs are calculated for OBF using a pixelated detector and a 16-segmented detector, SSB Ptychography, DPC using the pixelated detector, BF and ABF using the conventional annular detectors. Adapted from Ref. [23] with permission.

the obtainable signal from lithium sites in *S/TEM* are extremely weak because of the very small atomic number, and knock-on damage is easily introduced to the samples, which makes the direct imaging of lithium sites in LIB materials very challenging. Herein, we conducted low-dose and low-voltage lithium imaging in LIB samples via OBF STEM.

First, we evaluated the imaging efficiencies of OBF STEM and other techniques. **Figure 3** shows the noise-normalized PCTFs for various phase-contrast imaging techniques. The noise level can be calculated using the recently-developed noise evaluation theory in STEM. PCTFs can be normalized by the noise level for each imaging technique, which represents the SNRs as a function of the spatial frequency. Based on the

noise-normalized PCTFs, the imaging efficiencies of different techniques can be compared for not only conventional methods (ABF and BF) but also for recent phase imaging techniques (DPC and OBF). It is noted that we calculated the integrated PCTFs (iPCTFs) [12] to evaluate the efficiency, which can consider sample thickness effects. The iPCTF is effective for aberration-corrected atomic resolution imaging conditions, where the depth of field is comparable to or smaller than the sample thickness [12–14]. Figure 3 compares noise-normalized iPCTFs for each imaging technique, where the OBF using a pixelated detector achieves the highest efficiency. In the case of OBF using a segmented detector, the noise-normalized iPCTF decreased slightly from that of the pixelated one, but still possesses higher dose efficiency at all spatial frequencies than those of conventional techniques such as ABF and BF STEM. It is also noted that the iPCTF of OBF STEM is extended into the higher spatial frequency domains than the conventional methods, which means that higher spatial resolution can be achieved under the same optical conditions. **Table 1** shows the comparison of dose efficiency calculated by the noise-normalized iPCTFs. These values are normalized by the efficiency of ABF imaging. It is seen that OBF imaging has approximately two orders of magnitude higher dose efficiency than ABF imaging. We also calculated the iPCTFs and dose efficiencies for single side band (SSB) ptychography and DPC STEM using a pixelated detector as shown in Fig. 3 and Table 1. Compared to these techniques, OBF imaging with the segmented detector retains high dose efficiency. The pixelated detector has a vast number of detection areas compared to the segmented ones, which leads to significantly rich information about the sample. However, the dwell time of the STEM probe scan is still limited by the read-out speed of the detector and it is also necessary to process huge amounts of datasets in reconstruction processes such as electron ptychography. Thus, the OBF imaging with a segmented detector is promising for the practical low-dose imaging experiments due to the high dose efficiency and *live imaging* capability.

Here, we performed atomic-resolution observation of LiCoO_2 , a well-known LIB cathode material [15]. As for the observation condition, we selected an accelerating voltage of 120 kV for suppressing knock-on damage and a convergence semiangle of 30 mrad. **Figure 4** shows the experimental image of the LiCoO_2

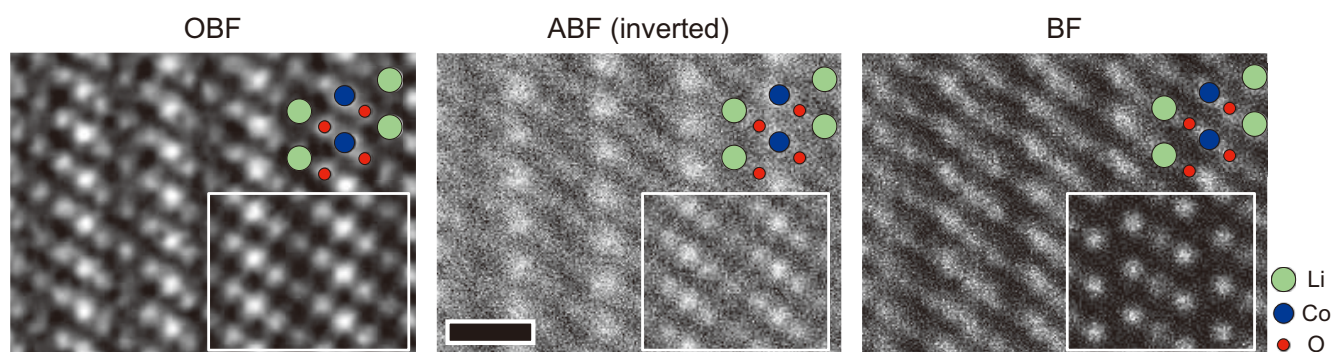
sample observed along the [010] direction. We observed the LiCoO_2 sample with a probe current of 2.4 pA and total dose of $2.8 \times 10^4 \text{ e}/\text{\AA}^2$. This condition is one order of magnitude lower than those in the previous literatures [10, 11]. In the case of conventional methods such as ABF and BF STEM, the obtained SNR is very poor and atomic structures are not well visualized. We also performed multi-slice STEM image simulation; the simulated results are shown as the insets. It is found that the experimental ABF contrast is slightly lower than the simulation, which may be due to the residual aberrations. This should result from the difficulties of aberration tuning with the poor SNR live image of ABF and BF techniques. In the OBF image, on the other hand, the atomic structures are well visualized not only for Co and O sites but also for Li sites at the same dose. Additionally, the experimental image contrast agrees well with the simulation, which means that finely tuned experimental data is acquired without residual aberrations or irradiation damage by using the live OBF imaging function.

Table 1 Dose-efficiency of different STEM techniques based on the noise-normalized iPCTFs shown in Fig. 3.

Imaging method	Dose efficiency ratio
OBF (pixel)	128.6
OBF (16-seg.)	69.2
SSB ptychography	100.7
DPC (pixel)	62.5
BF	1.2
ABF	1.0

These values are normalized by that of ABF. Adapted from Ref. [23] with permission.

Fig. 4 Experimental OBF, ABF, and BF STEM images of LiCoO_2 observed along [010] zone-axis.



The image contrast of ABF is inverted for comparison. These images are recorded under the same observation condition other than the residual aberrations and defocus. The defocus condition was adjusted to be optimal for each technique. The insets are simulated images of each imaging technique assuming the experimental conditions except for the residual aberrations. Scale bar: 5 Å. Adapted from Ref. [23] with permission.

Ultra-low-dose observation of an organic molecular crystal via OBF imaging

As an application of OBF STEM for further beam-sensitive materials, we performed atomic-resolution OBF observation of a copper hexachlorophthalocyanine (CuPcCl_{16}) crystal, a famous organic molecular crystal. Compared with the inorganic materials usually targeted in the S/TEM experiments, organic samples mainly consist of light elements such as carbon, and are significantly damaged by electron irradiation. CuPcCl_{16} is a famous pigment [16] and high-resolution observation using S/TEM has been frequently attempted as a model sample of organic materials. In the 1970s, Uyeda *et al.* reported an HRTEM observation of CuPcCl_{16} crystal for the first time [17]. Since then, aberration-corrected STEM and HRTEM observations have been performed on this sample [18,19]. However, due to the irradiation damage, the attainable spatial resolution is still lower than the typical resolution for inorganic samples [20]. Herein, we applied the low-dose OBF technique for atomic-scale imaging of the CuPcCl_{16} crystal.

Figure 5(a) shows the molecular structure of CuPcCl_{16} and the atomic structure of its molecular crystal observed along the [001] direction. From this projection, the atomic structure has five- and six-membered rings containing light elements such as carbon and nitrogen. At the center of the molecule and around it, there are rather heavy elements such as chlorine and copper. In the published literature using HRTEM, ADF and ABF STEM [18, 19, 21], the ring structure of light elements

and heavy atomic sites are observed. In this study, we try to observe directly all atomic sites including the light elements by using a STEM (JEOL JEM-ARM300F2) equipped with an eight-segmented detector (SAAF-octa) as shown in Fig. 2. The optical parameters are set at an accelerating voltage of 300 kV and a convergence semiangle of 16 mrad. Under this condition, the information limit of OBF imaging is calculated to be 0.62 Å, which is sufficient to resolve all the atomic-sites. Furthermore, we set the probe current as 0.8 pA to suppress irradiation damage, which is approximately two orders of magnitude lower than the usual cases. Under this ultra-low-dose condition, operators conventionally have to tune the FOV and lens aberrations such as defocus and astigmatism, referring to the extremely poor SNR live images. By using the live OBF imaging function as discussed before, tuning of imaging conditions can be performed even under this ultra-low-dose condition. Experimentally obtained results are also checked in real-time, which is very helpful during the data acquisition.

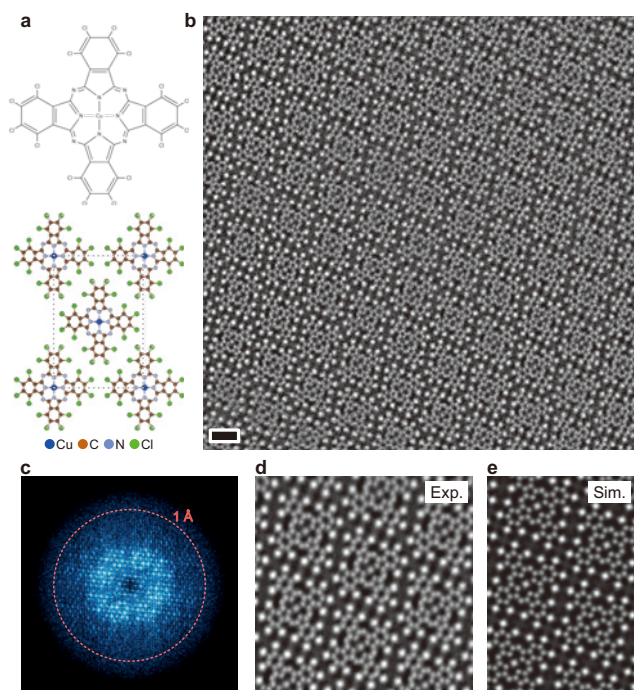
Figure 5(b) shows an experimental OBF image obtained from the CuPcCl_{16} crystal. The OBF image visualizes that the CuPcCl_{16} molecules are periodically arranged over a large FOV at high contrast. Figure 5(c) shows the power spectrum of the OBF image. The spots are confirmed in high spatial frequency domains corresponding to over 1 Å resolution, showing that the atomic scale structural information is obtained even in the organic sample. Figure 5(d) shows the unit-averaged OBF image obtained from the raw image shown in Fig. 5(b). This image visualizes all the atomic sites shown in the structure model in Fig. 5(a), where the six- and five-membered rings of carbon and nitrogen atoms are evidently resolved. It is noted that the bond distance between carbon atoms in the benzene rings is approximately 1.4 Å. Therefore, this resolution corresponds to the power spectrum shown in Fig. 5(c) and the calculated information limit of OBF imaging under the experimental condition. Figure 5(e) shows a simulated OBF image by the multi-slice method assuming the experimental conditions. The experimental OBF image agrees well with the simulation, showing that a high-quality dataset was experimentally obtained without irradiation damage and residual aberrations.

Finally, it should be noted that the image contrast of OBF imaging is maximized in the mid-plane focus condition (i.e., the focal plane of the STEM probe is located at the midplane of the sample along the incident beam direction). This condition is the same as the optimal focus condition of DPC imaging. In the case of image acquisition using conventional methods such as ADF and ABF imaging, operators view the live image in sync with the STEM scanning, and focus can be adjusted, referring to the maximum contrast condition that can be obtained with the probe focused at the entrance surface of the samples [22]. In OBF, the same procedure is available with the live OBF function, and the focus can be adjusted for the optimal condition for OBF imaging during the practical experiments. All the OBF datasets shown in this article were acquired using this adjusting process. This capability is an advantage of OBF STEM as a low-dose imaging technique compared to HRTEM, whose image contrast may be drastically changed by the sample thickness and defocus conditions.

Conclusion

We reviewed the theoretical background of OBF STEM and its applications to atomic-resolution imaging for beam-sensitive materials such as a battery material and an organic sample. The OBF imaging can visualize atomic structures at a significantly

Fig. 5



(a) Molecular structure of hexachlorophthalocyanine (CuPcCl_{16}) and its crystal structure along [001] zone-axis. (b) Experimentally obtained OBF image of the CuPcCl_{16} molecular crystal. Scale bar: 1 nm. (c) Power spectrum of the OBF image shown in (b). The dotted circle indicates the spatial frequency corresponding to 1 Å resolution. (d) Unit-cell averaged OBF image obtained from (b). (e) Simulated OBF image under the experimental condition. Adapted from Ref. [23] with permission.

lower-dose compared with other conventional techniques. Furthermore, because OBF imaging can acquire experimental datasets in real-time in sync with the STEM probe scan, the OBF STEM observations can be performed by the same operation as conventional methods. Thus, the OBF technique is promising for light element imaging and low-dose observation. While the results shown in this article are mainly focused on the atomic-resolution observation, we believe that the OBF technique is also promising for a wide range of spatial resolution analyses such as nanometer to micrometer scales [23].

Acknowledgments

This work was partly supported by JSPS KAKENHI (JP20H05659 and JP19H05788), JST ERATO (JPMJER2202), and JST PRESTO (JPMJPR21AA). The CuPcCl₁₆ sample was used by courtesy of Profs. Hiroki Kurata and Mitsutaka Haruta at Kyoto University.

References

- [1] D. Zhang, Y. Zhu, L. Liu, X. Ying, C.-E. Hsiung, R. Sougrat, K. Li, Y. Han, Atomic-resolution transmission electron microscopy of electron beam-sensitive crystalline materials, *Science*. **359** (2018) 675–679. <https://doi.org/10.1126/science.aao0865>.
- [2] S.D. Findlay, R. Huang, R. Ishikawa, N. Shibata, Y. Ikuhara, Direct visualization of lithium via annular bright field scanning transmission electron microscopy: A review, *Microscopy*. **66** (2017) 3–14. <https://doi.org/10.1093/jmicro/dfw041>.
- [3] N. Shibata, Y. Kohno, S.D. Findlay, H. Sawada, Y. Kondo, Y. Ikuhara, New area detector for atomic-resolution scanning transmission electron microscopy, *J. Electron Microsc.* **59** (2010) 473–479. <https://doi.org/10.1093/jmicro/dfq014>.
- [4] H. Ryll, M. Simson, R. Hartmann, P. Holl, M. Huth, S. Ihle, Y. Kondo, P. Kotula, A. Liebel, K. Müller-Caspary, A. Rosenauer, R. Sagawa, J. Schmidt, H. Soltau, L. Strüder, A pnCCD-based, fast direct single electron imaging camera for TEM and STEM, *J. Instrum.* **11** (2016) P04006. <https://doi.org/10.1088/1748-0221/11/04/P04006>.
- [5] N. Shibata, S.D. Findlay, Y. Kohno, H. Sawada, Y. Kondo, Y. Ikuhara, Differential phase-contrast microscopy at atomic resolution, *Nat. Phys.* **8** (2012) 611–615. <https://doi.org/10.1038/nphys2337>.
- [6] Y. Kohno, T. Seki, S.D. Findlay, Y. Ikuhara, N. Shibata, Real-space visualization of intrinsic magnetic fields of an antiferromagnet, *Nature*. **602** (2022) 234–239. <https://doi.org/10.1038/s41586-021-04254-z>.
- [7] H. Yang, I. MacLaren, L. Jones, G.T. Martinez, M. Simson, M. Huth, H. Ryll, H. Soltau, R. Sagawa, Y. Kondo, C. Ophus, P. Ercius, L. Jin, A. Kovács, P.D. Nellist, Electron ptychographic phase imaging of light elements in crystalline materials using Wigner distribution deconvolution, *Ultramicroscopy*. **180** (2017) 173–179. <https://doi.org/10.1016/j.ultramic.2017.02.006>.
- [8] K. Ooe, T. Seki, Y. Ikuhara, N. Shibata, Ultra-high contrast STEM imaging for segmented/pixelated detectors by maximizing the signal-to-noise ratio, *Ultramicroscopy*. **220** (2021) 113133. <https://doi.org/10.1016/j.ultramic.2020.113133>.
- [9] T. Seki, Y. Ikuhara, N. Shibata, Theoretical framework of statistical noise in scanning transmission electron microscopy, *Ultramicroscopy*. **193** (2018) 118–125. <https://doi.org/10.1016/j.ultramic.2018.06.014>.
- [10] R. Huang, Y. Ikuhara, STEM characterization for lithium-ion battery cathode materials, *Curr. Opin. Solid State Mater. Sci.* **16** (2012) 31–38. <https://doi.org/10.1016/j.cossms.2011.08.002>.
- [11] Y. Oshima, S. Lee, K. Takayanagi, Visualization of lithium ions by annular bright field imaging, *Microscopy*. **66** (2017) 15–24. <https://doi.org/10.1093/jmicro/dfw098>.
- [12] T. Seki, N. Takanashi, E. Abe, Integrated contrast-transfer-function for aberration-corrected phase-contrast STEM, *Ultramicroscopy*. **194** (2018) 193–198. <https://doi.org/10.1016/j.ultramic.2018.08.008>.
- [13] K. Ooe, T. Seki, Y. Ikuhara, N. Shibata, High contrast STEM imaging for light elements by an annular segmented detector, *Ultramicroscopy*. **202** (2019) 148–155. <https://doi.org/10.1016/j.ultramic.2019.04.011>.
- [14] T. Seki, K. Khare, Y.O. Murakami, S. Toyama, G. Sánchez-Santolino, H. Sasaki, S.D. Findlay, T.C. Petersen, Y. Ikuhara, N. Shibata, Linear imaging theory for differential phase contrast and other phase imaging modes in scanning transmission electron microscopy, *Ultramicroscopy*. **240** (2022) 113580. <https://doi.org/10.1016/j.ultramic.2022.113580>.
- [15] J.B. Goodenough, K.S. Park, The Li-ion rechargeable battery: A perspective, *J. Am. Chem. Soc.* **135** (2013) 1167–1176. <https://doi.org/10.1021/ja3091438>.
- [16] A. Abel, The new colour index international of pigments and solvent dyes, *Surf. Coatings Int.* **81** (1998) 77–85. <https://doi.org/10.1007/BF02692335>.
- [17] N. Uyeda, T. Kobayashi, E. Suito, Y. Harada, M. Watanabe, Molecular image resolution in electron microscopy, *J. Appl. Phys.* **43** (1972) 5181–5189. <https://doi.org/10.1063/1.1661094>.
- [18] M. Haruta, H. Kurata, Direct observation of crystal defects in an organic molecular crystals of copper hexachlorophthalocyanine by STEM-EELS, *Sci. Rep.* **2** (2012) 252. <https://doi.org/10.1038/srep00252>.
- [19] K. Yoshida, J. Biskupek, H. Kurata, U. Kaiser, Critical conditions for atomic resolution imaging of molecular crystals by aberration-corrected HRTEM, *Ultramicroscopy*. **159** (2015) 73–80. <https://doi.org/10.1016/j.ultramic.2015.08.006>.
- [20] S. Morishita, R. Ishikawa, Y. Kohno, H. Sawada, N. Shibata, Y. Ikuhara, Attainment of 40.5 pm spatial resolution using 300 kV scanning transmission electron microscope equipped with fifth-order aberration corrector, *Microscopy*. **67** (2018) 46–50. <https://doi.org/10.1093/jmicro/dfx122>.
- [21] M. Haruta, K. Yoshida, H. Kurata, S. Isoda, Atomic resolution ADF-STEM imaging of organic molecular crystal of halogenated copper phthalocyanine, *Ultramicroscopy*. **108** (2008) 545–551. <https://doi.org/10.1016/j.ultramic.2007.08.011>.
- [22] S.D. Findlay, N. Shibata, H. Sawada, E. Okunishi, Y. Kondo, Y. Ikuhara, Dynamics of annular bright field imaging in scanning transmission electron microscopy, *Ultramicroscopy*. **110** (2010) 903–923. <https://doi.org/10.1016/j.ultramic.2010.04.004>.
- [23] K. Ooe, T. Seki, Y. Kohno, A. Nakamura, Y. Ikuhara, N. Shibata, Low-dose Atomic-resolution Imaging Using OBF STEM, *KENBIKYO*. **57** (2022) 49–53. https://doi.org/10.11410/kenbikyو.57.2_49.

Advanced Analytical Methods for the Evaluations of Olefin Polymerization Catalysts and Produced Polymers

Masayoshi Saito¹, Takuo Kataoka¹, Masahide Murata²,
Yuhei Nakajima³, Rinya Masuko³, Hiroyuki Yamada³, Hideyuki Takahashi³

¹ TOHO TITANIUM CO., LTD. ² former TOHO TITANIUM CO., LTD. ³ JEOL Ltd.

Advanced spectroscopic and morphological analyses of the Ziegler-Natta catalyst for olefin polymerization (hereinafter referred to as Z/N catalyst) were performed under a non-atmospheric (inert gas) environment.

By using an air-isolated transfer vessel (hereinafter referred to as TV) for sample transfer/handling, the effects of atmospheric exposure on the deterioration of anhydrous magnesium dichloride (MgCl_2), which is a raw material for olefin polymerization catalysts, were investigated. In the sample kept under the non-atmospheric condition, clear morphology of MgCl_2 crystal was confirmed by the field emission scanning electron microscope (SEM). Furthermore, the cross section of the solid, which was polished by a "Cooling CROSS SECTION POLISHER™ (CCP)", was evaluated by the energy dispersive X-ray spectrometer (EDS). No oxygen was detected at the cross-section. On the other hand, in the sample which was intentionally exposed to air, the morphology was disturbed and the presence of oxygen atoms was detected. Based on these observations, TV is proven to be useful and effective for the analyses of air/moisture sensitive materials to obtain "reliable" analytical data.

Regarding the CCP instrument, this is equipped with a cooling system as well as the air seal capability. In the case of MgCl_2 ion-milled without cooling, it was seen that the morphology of the solid tended to change due to heat. Thus, the cooling was recognized as the key technique to evaluate the exact shape of MgCl_2 .

The Soft X-ray Emission Spectrometer (SXES) made it possible to detect the chemical bonding state of the outermost shell of the titanium atom in Z/N catalyst. In the case of MgCl_2 supported catalyst, a surface titanium species with a high electron density was present. This should be the analytical evidence to show the characteristics of the supported catalyst, which could provide the experimental fact to interpret the high active property of Ti in the supported catalyst.

In addition, by using X-ray micro-CT (X-ray CT), which is a non-destructive analysis method, was used to evaluate the internal void structure in polypropylene (PP) powder particle. The size distribution of the void in the PP particle could be obtained through the quantifying of CT images. We believe that this method is also effective for performing foreign matter analysis in polymers such as PP.

Introduction

The purpose of this paper is to introduce examples of advanced analytical technologies promoted by the authors with the aim to approach to the essential understanding on Z/N catalysts [1-3].

The technical and chemical points of Z/N catalysts will be briefly introduced.

More than half a century has passed since the invention of Z/N catalyst. It has been developed and improved with enormous labor and time at various research institutes around the world, and it is said to be an almost established technology at least from the viewpoint of industry [4-31].

Looking at the invention history, Z/N catalysts can be broadly

classified into two types. One is titanium trichloride (hereinafter referred to as TiCl_3) based, and the other is a " MgCl_2 supported catalyst" in which a titanium component is supported on the MgCl_2 surface. Both are solid heterogeneous catalysts. With the advent of MgCl_2 supported catalysts and further improvements, they have become the mainstream catalysts to produce polyolefins today.

Figure 1 shows the very simplified model of the chemical structure of the Z/N catalyst.

The location of the active Ti sites should be on the solid surface for both TiCl_3 and MgCl_2 supported catalyst. The structural difference in these two types of catalysts can be recognized as the different kind of metal in the solid bulk of the octahedral matrix, that is, Ti in TiCl_3 catalyst and Mg in MgCl_2

supported catalyst, respectively. At the same time, it is well known that the latter is several orders of magnitude more active than the former. This difference in performance by orders of magnitude has been discussed qualitatively from the perspective of organometallic chemistry, quantum chemistry, etc. [13].

However, understanding of the essence of the catalyst itself based on quantitation and direct observation have been eternal challenges. The reason for the obstacle is that the polymerization reaction occurs on a small part of the surface of the solid catalyst, and furthermore, the surface is heterogeneous. It is basically impossible to selectively extract only analytical information derived from catalytic active species. Even so, analytical means such as XPS that can extract information of a specific depth from the surface, for example, will highlight the state of the surface. The analytical methods that can observe only the intended part of a solid sample will greatly contribute to the progress of catalytic chemistry.

Z/N catalysts have another issue to be always considered. Not only the above-described components (titanium chloride and $MgCl_2$) but also the organic aluminum component that coexists for catalytic activation is denatured and inactivated in a short time by the atmosphere (oxygen) and moisture. (An example of changes in atmospheric exposure time and catalytic activity is shown in Fig. 2.) Therefore, handling in an atmospheric unexposed dry inert gas (nitrogen or argon) environment is mandatory. Not only in the industrial production of polyolefin, but of course, analysis is no exception, and it is necessary to handle the catalyst raw material and catalyst under inert gas.

In recent years, analytical instruments that enable atmospheric non-exposure analysis has been advanced. This progress makes it possible to easily analyze air/moisture sensitive samples such as Z/N catalysts.

In this report, we will introduce our analysis results of catalysts evaluated by CCP-SEM [32-34], SEM-SXES, and Field Emission Electron Probe Microanalyzer (EPMA)-SXES [35-42] under non-atmospheric conditions.

In addition, the analysis results of polymerized PP powder particles using X-ray CT [43-48] are introduced. The technological background of this subject is as follows; This is closely related to the industrial PP production technology. That is, the catalyst particles are composed of many microcrystals of

$TiCl_3$ or $MgCl_2$ described above, forming particles of several tens of micrometers. This small size catalyst particle grows to particles of several hundreds to several thousands of micrometers while making a polymer by polymerization reaction. If the inside of the expanded particles is sparse, the particle strength should be weak, and the particle fracture easily occurs, resulting in that the fine powder components are generated. Presence of fine powders can cause operating problems such as line plugging. Thus, it is extremely important to grasp the degree of density in the PP powder particles from the viewpoint of catalyst particle design.

By the way, in order to know the internal structure information of PP particle, fracture analysis by microtomy has been common. In this analysis method, it is difficult to grasp the entire particle because the information is only on the local area, and it takes a lot of time and efforts until the result is obtained because of pretreatment. On the other hand, X-ray CT has been known well as a non-destructive analysis method. However, in conventional X-ray CT, there is a problem with resolution because most X-rays are transmitted to materials with low density such as PP. For this reason, it was necessary to dye it with heavy metals such as osmium and ruthenium, and paying careful attention to safety was also required. The X-ray CT used in this study has enhanced the contrast ability between low-density components so that the whole picture can be visualized without staining even in polymers such as PP with low density, and various 3D analysis such as void and particle size distribution is possible. We introduce our analysis data for PP powder particle analysis by an advanced high performance X-ray CT instrument.

Experimental

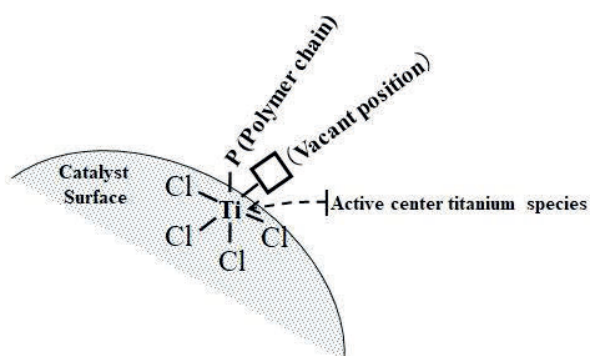
[CCP-SEM experimental method]

SEM: JSM-7610F manufactured by JEOL Ltd. was used at an accelerating voltage of 1 kV to 5 kV.

CCP: IB-19520CCP manufactured by JEOL Ltd. was used under the conditions that the accelerating voltage was 4.5 kV, the milling time was 5 hours, and the holder temperature was at room temperature or $-120\text{ }^\circ\text{C}$ or less.

EDS: Two UltraDry EDS detectors with effective area of 60 mm^2 manufactured by Thermo Fisher Scientific Co., Ltd. were used at 1 to 8 kV of an accelerating voltage.

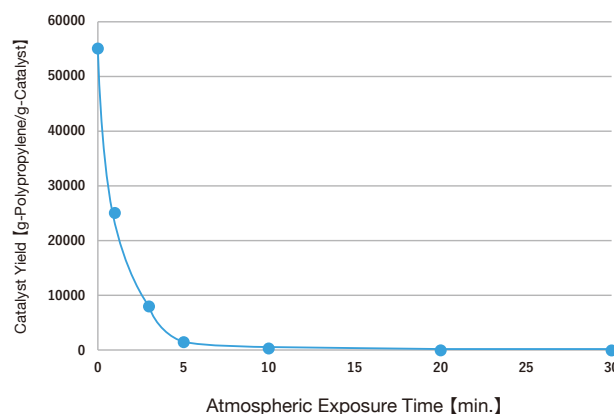
Fig. 1 Structure model of active titanium species on the surface of Ziegler-Natta catalyst.



The interior of a solid catalyst consists of an octahedral structure composition by metal-Cl bonds

Metal species of $\delta TiCl_3$ catalyst=Ti
Metal species of supported catalyst=Mg

Fig. 2 Relationship between atmospheric exposure time and catalyst activity.



Polymerization conditions: 2 liter autoclave bulk polymerization, Aluminum/Ti = 500, Al/Donor = 10, Ti = 0.00264 mmol, External donor = CMDMSi, H_2 = 1.5 NL, Liquid propylene = 1.4 L, Pre-polymerization = $20\text{ }^\circ\text{C}$ -5 min., Main-polymerization = $70\text{ }^\circ\text{C}$ -60 min.,

Anhydrous Magnesium dichloride (MgCl_2) was used as the sample. The measurements were performed under inert gas (dry argon) atmosphere or air exposed condition.

[SEM, EPMA-SXES experimental methods]

TiCl_3 catalyst: TiCl_3 catalyst was synthesized according to JPN 50-83284.

MgCl_2 -Supported TiCl_4 catalyst: Catalyst C reported in *Bull. Chem.Soc.Jpn.*2022, **95**,367-373 was used as MgCl_2 -supported TiCl_4 catalyst.

SXES: X-ray spectral analysis was performed by using SS-94040XSER (SXES-ER) manufactured by JEOL Ltd.

In order to check the resolution sensitivity of SXES, MgCl_2 -Supported TiCl_4 catalyst was evaluated and compared by SXES and EDS. The details of the instruments used were as follows; SXES measurement was performed with JS300N of SXES-ER installed in the SEM machine (JSM-7200F manufactured by JEOL Ltd.) under the conditions of the accelerating voltage = 5 kV, probe current = 20 nA, exposure time = 30 seconds, and accumulation = 20. On the other hands EDS investigation was conducted by EDS-1 manufactured by AMETEK Inc. installed to SEM (JSM-7500F manufactured by JEOL Ltd.) The measuring conditions were Probe size = 10 mm², the accelerating voltage = 10 kV, and the analytical time = 10 minutes.

SXES measurement of TiCl_3 catalyst was conducted with JS300N of SXES-ER installed in the EPMA machine (JXA-iHP200F manufactured by JEOL Ltd.) under the conditions of the accelerating voltage = 5 kV, probe current = 100 nA, exposure time = 60 seconds, accumulation = 10.

[X-ray CT experimental conditions]

X-ray CT: $\mu\text{CT}50$ instrument, which was manufactured by SCANCO Medical AG (Distributor: JEOL Ltd.) was used. The operation conditions were as follows: X-ray output = 70 kV / 57 μA , measurement time = 4 hours, sample holder size diameter = 4 mm ϕ Length = 15 mm, Integration time =

2500 ns, Average time = 2, projection = 1500 steps, spatial resolution < 2.0 μm , voxel size = 0.8 μm . The reconstruction image resolution was done at 3500 \times 3500 pixels.

CCP-SEM Results and Discussion

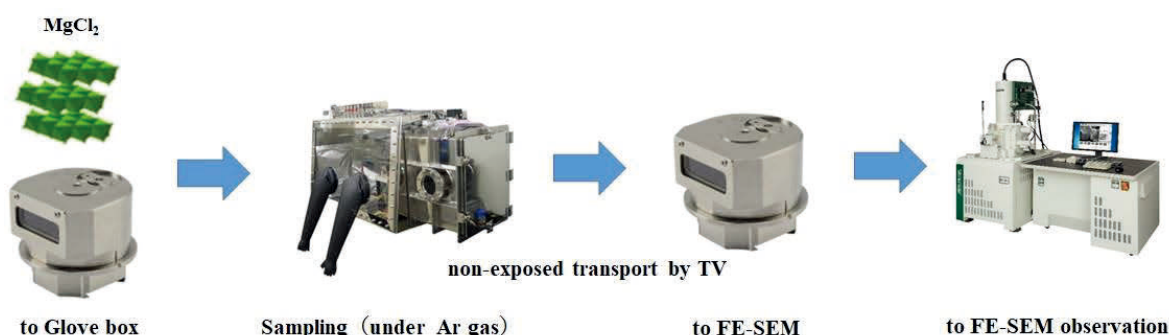
As mentioned, the olefin polymerization catalysts deteriorate when in contact with the atmosphere, even for a short time. Here, a TV was used to block out from the atmosphere. MgCl_2 as a catalyst support was sampled on a TV in a glove box filled with dry argon gas with a dew point of -50°C or less, and then transported to SEM (**Scheme-1**). The results of surface observation by SEM are shown in **Fig. 3**.

Successively, the sample used without atmospheric exposure was brought into contact with the atmosphere for 10 minutes as shown in **Scheme-2**, and the surface was observed by SEM (**Fig. 4**). At this time, SEM observation was evaluated at the same location of the sample as that showed in Fig. 3. As a result, it was able to observe a clean edge area in MgCl_2 sample without atmosphere exposure. On the other hand, in the sample exposed to the air, the edge part was rounded and the shape was deformed.

In order to understand the cause of deformation, the internal structure in the solid was investigated by cross-sectioning MgCl_2 under conditions of -120°C using CCP. Specifically, cross-sectional observation by SEM and elemental analysis of oxygen by SEM-EDS were performed. To improve the X-ray count rate and reduce X-ray vignetting at the edge of the sample surface irregularity, two EDSs were deployed opposite each other on the sample diagonal. The analysis results are shown in **Fig. 5**. From the SEM image at the top of Fig. 5, it was confirmed that the cross-section of MgCl_2 fabricated by the CCP method has a laminated structure.

EDS analysis was performed using this sample. As a result, the oxygen atoms were substantially not detected from most part of the samples. It should be noticed that oxygen has been seen in

Scheme-1 Sample handling procedure for air isolated state FE-SEM experiment.



Scheme-2 Sample handling procedure for non-air isolated state FE-SEM experiment.



some of the edges of $MgCl_2$ only, but it should be from the carbon tape used to install $MgCl_2$ in the TV. It would be plausible that oxygen atom adhered to $MgCl_2$ during cross-sectional processing.

For comparison, the elemental analysis by EDS of a sample in which was exposed to the atmosphere for 10 minutes was conducted. Very high concentration of oxygen was detected from the cross-sectional site (Fig. 6). This indicates that oxygen

or moisture in the atmosphere adsorbed on the surface of $MgCl_2$ and altered the sample.

CCP-SEM measurement results introduced/discussed so far were obtained with $MgCl_2$ sample processed by CCP in a state of cooling to $-120\text{ }^\circ\text{C}$. But for the purpose of confirming the necessity of cooling, $MgCl_2$ was processed at room temperature without cooling, and then transported to SEM without exposure

Fig. 3 Observation of $MgCl_2$ by SEM with air isolated state system.

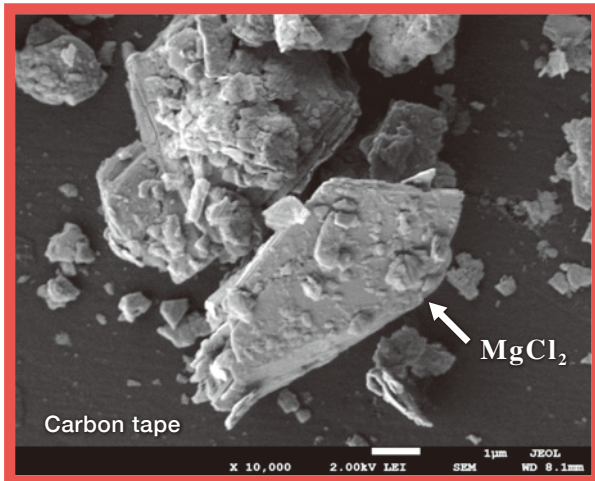


Fig. 4 Observation of $MgCl_2$ by SEM with non-air isolated state system.

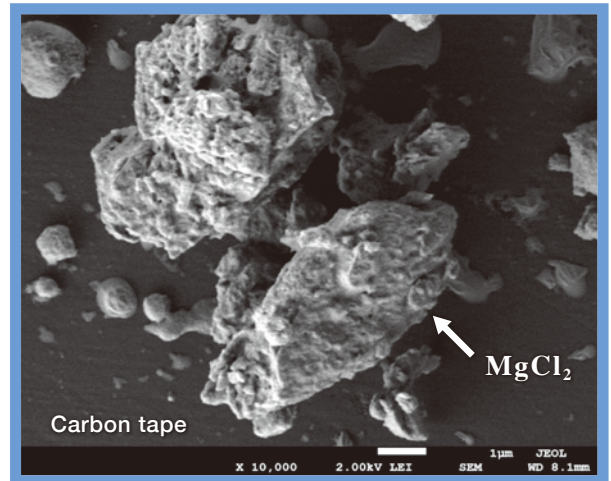


Fig. 5 $MgCl_2$ cross-section analysis (O element) with air isolated state by EDS.

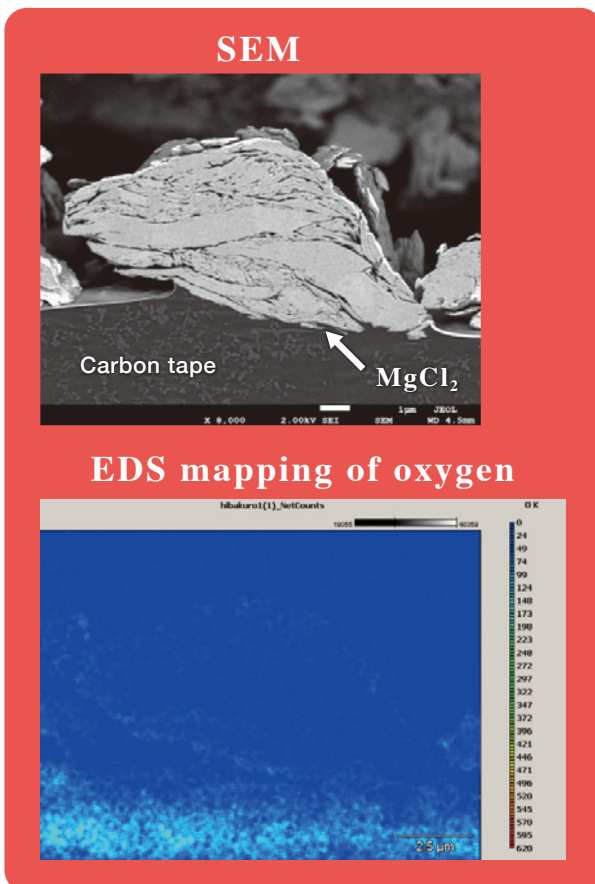
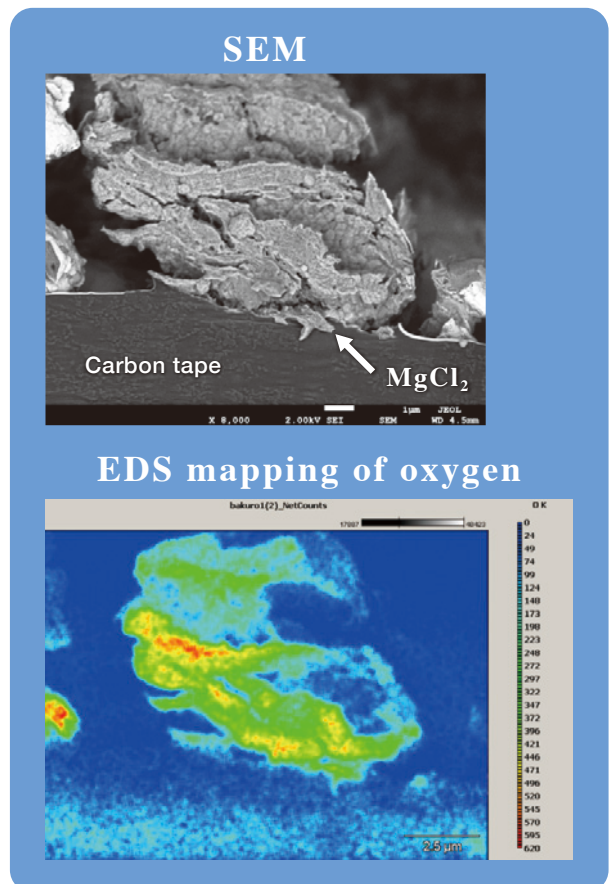


Fig. 6 $MgCl_2$ cross-section analysis (O element) with non-air isolated state by EDS.



to the atmosphere. A cross-section shape of this no-cooling sample is shown in Fig. 7. As shown, the laminated structure of MgCl_2 was not maintained when processed without cooling. This suggests that heat accumulation in the solid sample during cross-sectional polishing, and the cross-section melted due to the heat. From this result, the cooling of the sample is a very important condition as well as non-exposure to the atmosphere.

Fig. 7 MgCl_2 cross-section SEM image processed with air-isolated state and without cooling during the polishing.

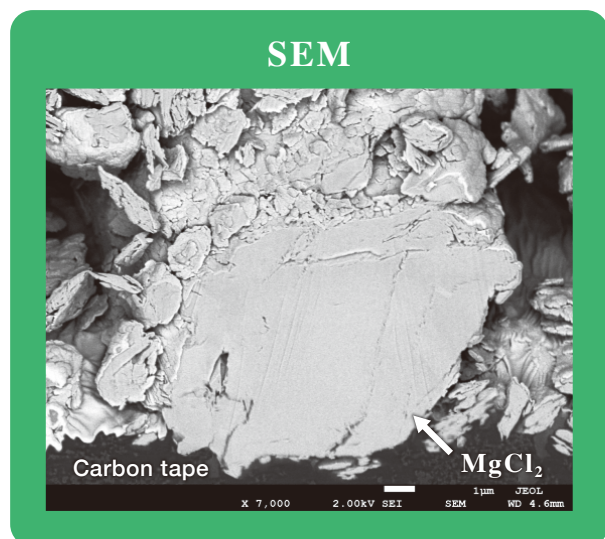
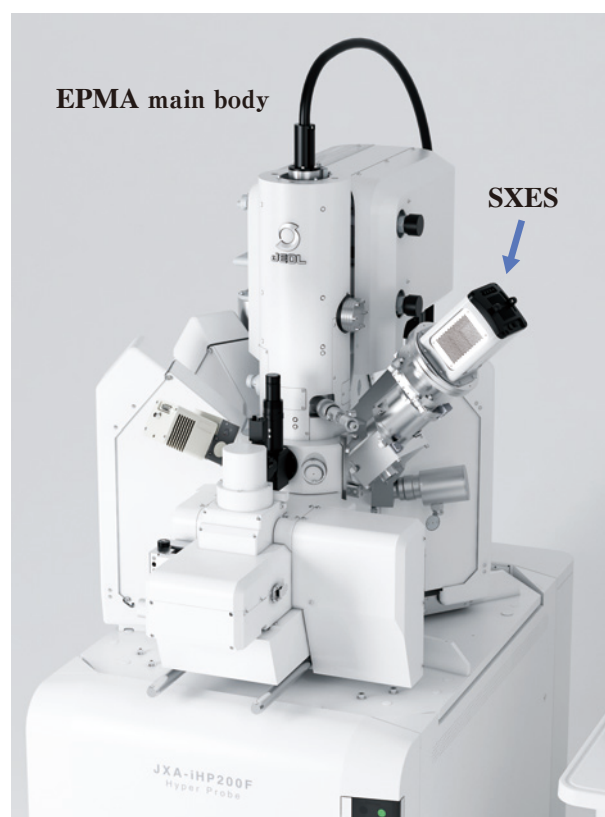


Fig. 8 External view of SXES instrument attached to EPMA.



SXES Results and Discussion

As mentioned in the introductory section, the active species of Z/N catalysts are limited to titanium, which shall be coordinative unsaturation on solid surfaces. The main difference between TiCl_3 base catalyst and MgCl_2 -supported TiCl_4 catalyst is in the different kind of metal in the solid bulk. Nevertheless, the activity of both catalysts differs by more than several orders of magnitude [17, 30, 31].

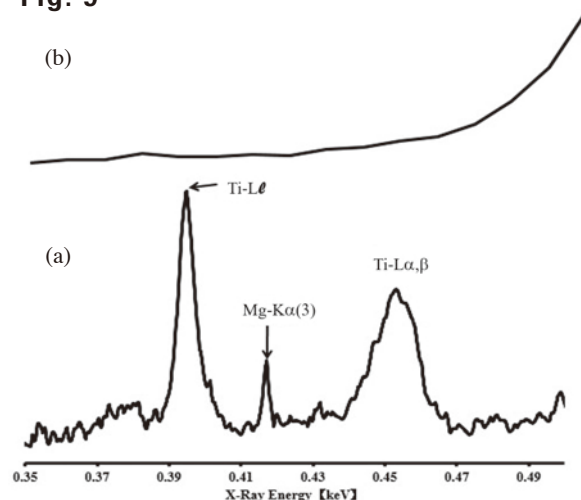
Regarding this, it has been expected to obtain direct experimental and analytical evidence to interpret the chemical meaning of how different between titanium and magnesium, but it was hindered by the limitations of the performance of analytical instruments such as not enough resolution level. However, SXES instruments that can obtain information on the chemical bonding state has been developed due to advances in analytical technology. By using SXES, the differences in the electronical structure of the particular atom among the kind of catalysts have begun to be seen analytically. Applying SXES results, it is expected that further precise design of catalysts will be possible in the future.

The SXES instrument used in this work is a parallel-detection type X-ray spectrometer with ultra-high sensitivity and energy resolution that uses diffraction gratings and a high-sensitivity X-ray CCD camera. Without to say, this is exactly the next-generation X-ray spectrometer that can obtain chemical bonding information that was previously impossible with EDS and other devices (Fig. 8) [37, 40].

Figure 9 shows spectra measured using an apparatus equipped with EDS to SEM and an apparatus equipped with SXES to EPMA and SEM. The measured sample was MgCl_2 -supported TiCl_4 catalyst. As a result, the signal could not be confirmed by EDS, but in SXES, the higher-order line of the Mg-K emission spectrum can be clearly confirmed in addition to the Ti-L emission spectrum. From this result, it can be said that SXES has high energy resolution.

In particular, the Ti-L emission spectrum on the high-energy side (around 450 eV to 460 eV) can be observed due to the difference in valence electron states and binding energy at the inner shell level. The surface heterogeneity shall be the plausible interpretation [38]. For instance, Busico et. al. discussed the different structures of active species between isospecific active sites and specific ones [15].

Fig. 9



Spectra of MgCl_2 -supported catalyst measured by (a) SXES and (b) EDS, respectively.

From the SXES spectrum, $MgCl_2$ -supported $TiCl_4$ catalyst indicated the relatively higher intensities strength of the high-energy side around 455 eV in comparison with $TiCl_3$ catalyst case (Fig. 10). The intensity ratio of the high energy side to the low energy side is also related to the performance of the catalyst [30]. This indicates that electron donation from magnesium to surface titanium can cause high activity.

We believe that we have been able to show the validity of the relationship between the electron charge density and polymerization activity of titanium, which has been said in the past, as analytical data [13].

Results and discussion of X-ray CT

Materials with low densities such as PP and polyethylene (hereinafter referred to as PE) are difficult to achieve contrast because X-rays transmit too much (Fig. 11). In order to solve this problem, the X-ray CT used in this work (Fig. 12) enables high-contrast data acquisition by eliminating ambient spatial noise by using a cone beam with a beam angle of 1° or less. In addition, since the dark current before measurement is automatically optimized, it is possible to obtain high-quality and high-precision data. Furthermore, while incorporating a sample holder method that does not require central axis adjustment and a fully automatic calibration function, it prevents an unspecified number of uneven operations without worrying about the sample position, and anyone can acquire highly reproducible clear

images under various conditions with spatial noise removed. In terms of this advanced X-ray CT instrument, we would emphasize the availability of wide range of options, such as in-situ measurement with compression and tension devices, stress curve acquisition, cooling device, automatic sample changer with up to 20 sample holders, and contrast enhancement for light mass samples. These shall be applicable for the efficient polymer characterization work. It is also equipped with functions such as a filter changer that can reduce the effect of beam-hardening occurring during high-density sample imaging [43, 44].

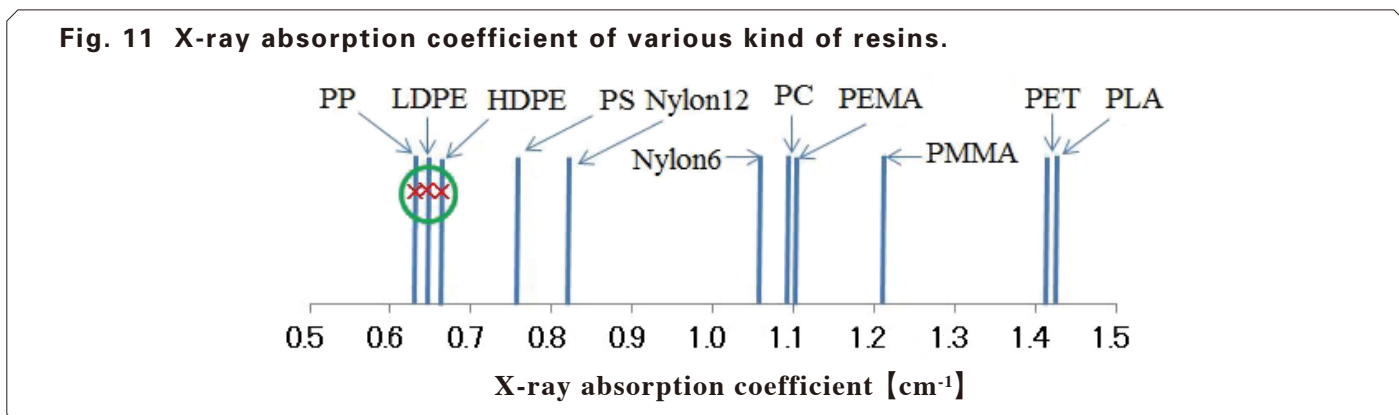
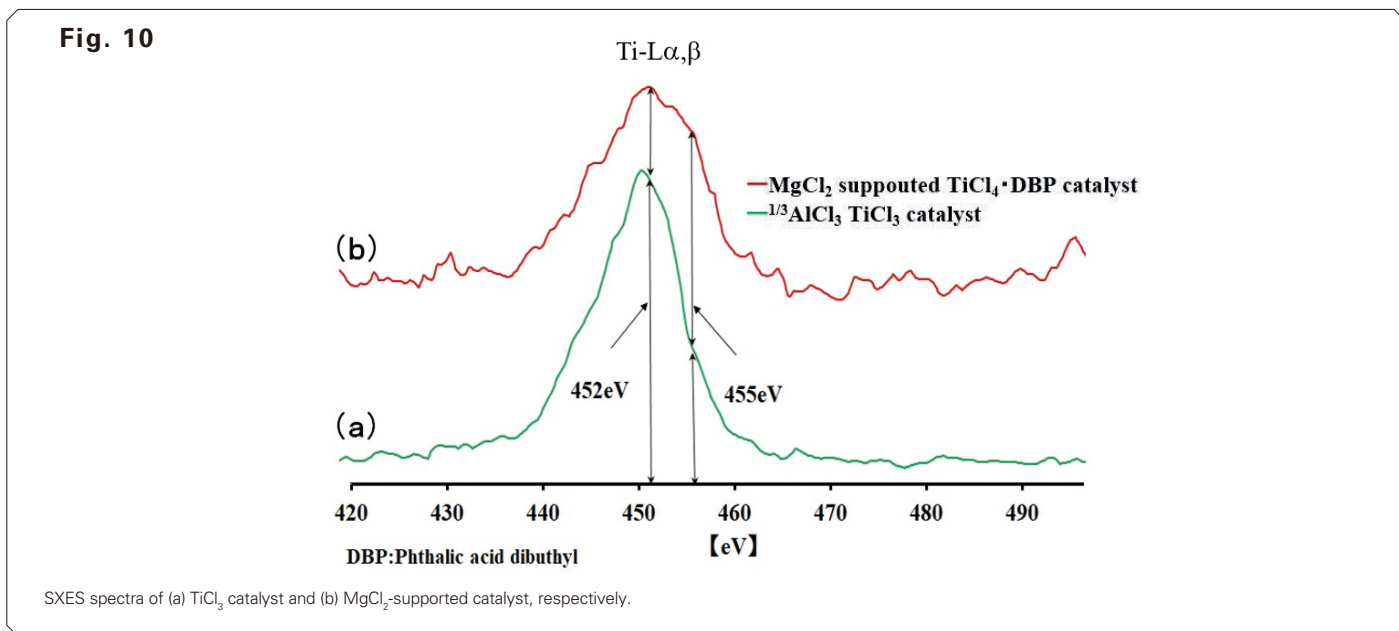
Figure 13 shows three X-ray CT images of “the base PP powder”, “full surface cut”, and “front and top cut”, respectively. The gray color on the image is resin, and the red color is voids. As seen, even in PP and PE, which has been difficult to contrast, the resin solid and voids can be clearly distinguished.

Furthermore, from each void colored, the void size distribution can be quantified in 3D (Fig. 14).

The ability to easily visualize the internal state of polyolefin particles produced by polymerization should be of great help to the design of industrial catalysts and its preparation technologies.

Summary

The atmospheric non-exposure performance of TV was confirmed through SEM and CCP-EDS analyses of $MgCl_2$. That is, $MgCl_2$ crystal as seen in SEM image and oxygen was not detected by CCP-EDS. In addition to the atmospheric non-



exposure function, the CCP was also equipped with a cooling mechanism, and it was possible to observe the exact shape of $MgCl_2$, which tends to change shape due to heat. Therefore, CCP is a useful tool not only for olefin polymerization catalyst sample but also for any other materials of air / moisture / heat sensitive.

Analysis using SXES made it possible to confirm the correlation with the chemical bonding state of titanium

outermost electrons in the olefin polymerization catalyst. This will enable the estimation of the electronic structure of high-performance active titanium species and the design of catalysts. We expect to further progress catalyst research and development.

It was confirmed that quantitative analysis of void information in PP powder can be performed using images and numerical values using X-ray CT, which is a non-destructive analysis method, without staining. This instrument shall also be effective for measuring foreign matter analysis in polymers.

Fig. 12 External view of X-ray CT machine (μ CT50).



Conclusion

In this report, we reported several analytical topics conducted with the latest advanced analytical instruments. The evaluation field was Z/N catalysts and PP powder produced from the catalyst. It has been said that the research on olefin polymerization catalysts has been exhausted. However, we hope that the development of advanced (revolutionary breakthrough) analytical instruments will enable us to obtain deeper and more innovative results in the future.

In the future, cross-checking of the same point of sample by using a wide variety of analytical instruments will be possible even under non-exposure to the atmosphere, which will lead to improved reliability of analysis results. Such progress will pave the way for the development of new materials.

We believe that the advanced analytical technology and the analytical facts obtained from it, as well as the uniqueness of ideas that can read and interpret them, are the driving force for future technological development that contributes to society.

Fig. 13 Cross-sectional imaging of PP powder by X-ray CT.

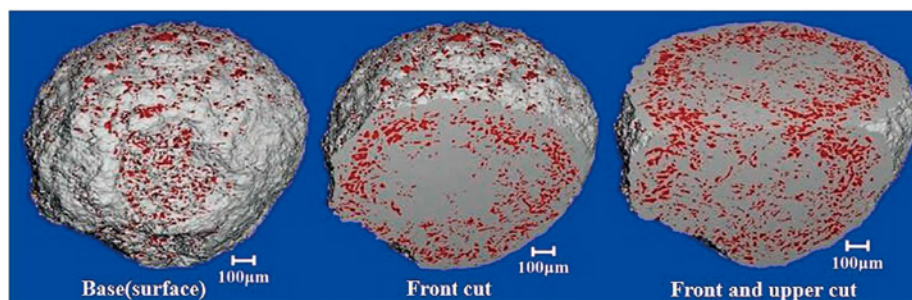
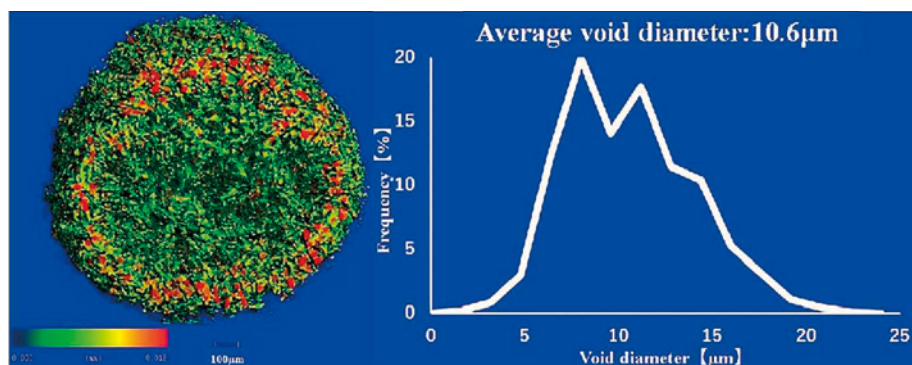


Fig. 14 Void distribution and average void diameter of PP powder determined by X-ray CT.



Acknowledgments

We would like to express our sincere gratitude to Prof. Masami Terauchi at the Institute of Multidisciplinary Research for Advanced Materials of Tohoku University for his kind consultation on SXES analysis.

We would also like to express our sincere gratitude to Prof. Yuuki Imai at the Division of Integrative Pathophysiology Proteo-Science Center Graduate School of Medicine Ehime University for his kind consultation on X-ray CT analysis.

We would like to express our appreciation to Dr. Shunsuke Asahina, Dr. Yusuke Sakuda, Dr. Shogo Koshiya, Mr. Yuji Hasebe and Dr. Masaru Takakura at JEOL Ltd. for support with SEM, CCP and SXES measurements.

Our thanks are also due to Mr. Osamu Emura, Mr. Keiichirou Hosaka, Mr. Ryuichi Narikiyo, Mr. Yusuke Harano, Mr. Hiromichi Tanaka, Mr. Takaki Kobashi, Ms. Saori Uchino, Ms. Kazuko Matsuoka, Ms. Satomi Kambayashi and Ms. Kazue Masubuchi at JEOL Ltd. for dedicated support.

References

- [1] K. Ziegler, E. Holzkamph, H. Breil, H. Martin, *Angew. Chem.*, **67**, 541 (1955).
- [2] G. Natta, *J. Polym. Sci.*, **16**, 143 (1955).
- [3] G. Natta, *Angew. Chem.*, **68**, 393. 4 (1956).
- [4] K. Soga, M. Terano, S. Ikeda, *Polym. Bull* (Berlin), **1**, 849 (1979).
- [5] P. Pino, R. Mulhaupt, *Angew. Chem.*, **92**, 869 (1980); *Angew. Chem., Int., Ed. Engl.*, **19**, 857 (1980).
- [6] Norio Kashiwa, *Poly. J.*, **12**, 603 (1980).
- [7] J. C. W. Chien, J. C. Wu, C. I. Kuo, *J. Polym. Sci., Polym. Chem., Ed.* **21**, 737 (1980).
- [8] T. Keii, *Makromol. Chem.*, **183**, 2285 (1982).
- [9] P. Pino, G. Fochi, O. Piccolo, U. Gianni, *J. Am. Chem. Soc.*, **104**, 7381 (1982).
- [10] K. Soga, T. Sano, K. Yamamoto, T. Shiono, *Chem. Lett.* **11**, 4, 425 (1982).
- [11] T. Keii, E. Suzuki, M. Tamura, M. Murata and Y. Doi, *Makromol. Chem.* **83**, 2285 (1982).
- [12] Y. Doi, M. Murata, K. Yano and T. Keii, *Ind Rng. Chem. Prod. Res. Dev.* **21**, 580 (1982).
- [13] Yoshiharu Doi, Kazuo Soga, Masahide Murata, Eiichi Suzuki, Yoshio Ono and Tominaga Keii, *POLYMER COMMUNICATIONS*, Vol. **24**, August (1983).
- [14] R. Spitz, J. L. Lacombe, A. Guyot, *J. Polym. Sci., Polym. Chem. Ed.*, **22**, 2641 (1984).
- [15] V. Busico, P. Corradini, L. De. Martino, A. Proto, E. Albizati, *Makromol. Chem.* **187**, 1115 (1986).
- [16] M. Terano, T. Kataoka, T. Keii, *Makromol. Chem.*, **188**, 6, 1477 (1987).
- [17] Masahiro Kakugo, Tatsuya Miyatake, Yukio Naito and Kooji Mizunuma, *Macromolecules*, **21**, 314 (1988).
- [18] Kazuo Soga, Takeshi Shiono, Yoshiharu Doi, *Makromol. Chem.*, **189**, 1531 (1988).
- [19] M. Terano, T. Kataoka and T. Keii, *JOURNAL OF MOLECULAR CATALYSIS*, **56**, 203 (1989).
- [20] M. Terano, M. Saito, T. Kataoka, *Makromol. Chem. Rapid Commun.*, **13**, 2, 103 (1992).
- [21] H. Mori, M. Teran, Surface Characterization of Ziegler-Natta Catalysts: XPS, SAM, HRTEM, and in-situ Solid State NMR Studies, Progress and Development of Catalytic Olefin Polymerization, T. Sano, T. Uozumi, H. Nakatani, M. Terano, Eds Technology and Education Publishers, Tokyo 65-74.
- [22] K. Soga, T. Uozumi, M. Saito, T. Shiono, *Makromol Chem Phys* **195**, 1503-15 (1994).
- [23] K. Shimozawa, M. Saito, T. Kataoka and R. Chujo, *Polym Int.* **51**, 530 (2002).
- [24] R. Chujo, K. Shimozawa, M. Saito, T. Kataoka, I. Nishiyama, M. Ishida, N. Sawa, Progress and Development of Catalytic Olefin Polymerization, Technology and Education Publishers, Tokyo, p264 (2000).
- [25] Inter-net connection: The Two-Site Model Simulation Analysis, URL: <https://twosite-model.com>.
- [26] R. Ohashi, M. Saito, T. Fujita, T. Nakai, H. Utsumi, K. Deguchi, M. Tansho and T. Shimizu, *Chem. Lett.*, **41**, **12**, 1563 (2012).
- [27] Takahiro Iijima, Tadashi Shimizu, Atsushi Goto, Kenzo Deguchi, Toshihito Nakai, Ryutaro Ohashi and Masayoshi Saito, *Journal of Physics and Chemistry of Solids*, **135**, 109088 (2019).
- [28] <https://www.pslc.ws/mactest/ziegler.htm#com>.
- [29] T. Taniike et al., *ACS Catal.* **11**, 15, 9949–9961 (2021).
- [30] M. Saito, M. Murata, T. Kataoka, Y. Sakuda, H. Takahashi, *Bull. Chem. Soc. Jpn.*, **95**, 367-373 (2022).
- [31] M. Saito, T. Uozumi, M. Murata, T. Kataoka, R. Chujo, *Polyolefins Journal*, Vol. **9**, No. 2 (2022).
- [32] M. Shibata, *JEOL NEWS*, **39**, p28 (2004).
- [33] N. Erdman, et. al., *Microscopy today*, **12** (s02) (2006).
- [34] Y. Nakajima, et. al., *Microscopy and Microanalysis*, p. 1194-1195 (2011).
- [35] M. Terauchi, H. Takahashi, N. Handa, T. Murano, M. Koike, T. Kawachi, T. Imazono, M. Koeda, T. Nagano, H. Sasai, Y. Oue, Z. Yonezawa and S. Kuramoto, *Journal of Electron Microscopy*, vol. **61**, 1-8 (2012).
- [36] M. Terauchi, "Valence Electron Spectroscopy for Transmission Electron Microscopy," In: Kumar C. (eds) *Transmission Electron Microscopy Characterization of Nanomaterials*. Springer, Berlin, Heidelberg.
- [37] H. Takahashi et al., "Development of soft X-ray emission spectrometer for EPMA/SEM and its application," IOP Conf. Ser. Mater. Sci. Eng.
- [38] M. Terauchi, S. Koshiya and K. Kimoto, IOP Conf. Series: *Materials Science and Engineering*, **304**, 012018-1-6 (2017).
- [39] M. Terauchi and Y. Sato, *JEOL NEWS*, **53**, 30-35 (2018).
- [40] Handbook of Soft X-ray Emission Spectra Version 6.0 (Sep. 2020), URL: https://www.jeol.co.jp/download_soft_x-ray.html.
- [41] J. E. HOLLIDAY, Soft X-Ray Emission Bands and Bonding for Transition Metals, Solutions and Compounds, 101-132, "Soft X-Ray Band Spectra and the Electronic Structure of Metals and Materials", 1968, Edited by Derek J. Fabian, ACADEMIC PRESS London and New York.
- [42] J. A. Bearden, *Review of Modern Physics*, **39**, 1 (1967).
- [43] Lisa Falco, Markus Burkhart, SCANCO Medical AG, Fabrikweg 2, 8306 Brüttsellen, Switzerland.
- [44] Apichart Jinnapat, Andrew Kennedy, *Metals*, **1**, 49-64 (2011).
- [45] K. Smolana, T. Gregor, J. Kosek, *European Polymer Journal*, **49**, 3966 (2013).
- [46] A. Zubov, L. Pechackova, L. Seda, M. Bobak, J. Kosek, *Chemical Engineering Science*, **65**, 2361 (2010).
- [47] Klara Smolna, Tomas Gregor, Juraj Kosek, *European Polymer Journal*, **49**, 3966 (2013).
- [48] Alexandr Zubov, Lucie Pecháčková, Libor Šedá, Marek Bobák, Juraj Kosek, *Chemical Engineering Science*, **65**, 2361 (2010).

A Practical Method for the Measurement of ^{183}W NMR Signals in Solution: Challenge to Multinuclear Solution NMR

Toshiyuki Oshiki Okayama University

We tried to measure ^{183}W solution NMR to develop a new tungsten catalyst system for bulk metathesis polymerization of cycloolefins. ^{183}W nucleus is $I = +1/2$ and has a receptivity relative to ^{13}C is 6%. Unlike routinely measured ^1H and ^{13}C NMR, few works of literature have described detailed measurement conditions for low-frequency nuclei such as ^{183}W . There needs to be more practical information available for ^{183}W NMR, including the amount of sample, the most critical issue for the measurement, and how much measurement time is needed. We have examined ^{183}W solution NMR measurement with a 10 mm low-frequency probe since 2014. We finally observed a ^{183}W signal in 2018 using about 500 mg sample. We can now perform routine ^{183}W NMR measurements where the signal can be observed in about 3 hours. This paper describes detecting the ^{183}W signal and establishing standard measurement conditions in a few hours.

What part do we want to observe of a soluble transition metal complex?

Solution NMR measurements are mostly ^1H and ^{13}C nuclei as a target. An organic molecule comprises an organic ligand of hydrogen, carbon, and other elements. Elucidating the carbon skeleton, i.e., the molecular structural framework, and observing the hydrogen bonded to the carbon will ultimately lead to understanding the overall structure of the organic moiety.

On the other hand, the case of metal complexes should be different. A metal complex is an ion bound to a ligand, either an inorganic ion or an organic molecule. In most cases, ^1H and ^{13}C in the organic ligands are measured.

Since the essence of the function of metal complexes is produced from the metal ion itself. The first approach should be the direct observation of the metal ion, and the second approach should be to observe the atoms directly bonded to the metal ion.

Tungsten complexes for metathesis polymerization of dicyclopentadiene

Since 2009, we have developed an excellent practical tungsten catalyst system for the metathesis polymerization of cycloolefins, especially dicyclopentadiene. Hercules commercialized the bulk (solvent-free) metathesis polymerization of dicyclopentadiene as a monomer in the 1980s [1, 2]. The dicyclopentadiene molded resin is still produced commercially today because of its suitability for industrial applications such as the body for large construction machinery. The catalyst system used in this polymerization consists of a tungsten complex generated by the reaction of a

tungsten salt and an organic ligand. The catalytic activity is exhibited when the tungsten complex as a precatalyst reacts with an organoaluminum compound as a co-catalyst. Thus, the tungsten catalyst system is the so-called Ziegler type.

Figure 1 shows the historical evolution of tungsten catalysis for the bulk polymerization of dicyclopentadiene. In 1985, Basset and co-workers reported well-defined tungsten catalysts (Fig. 1(b)). In 1992, Bell and co-workers reported a similar oxo-tungsten complex system [4]. In an industrial process for the bulk polymerization of dicyclopentadiene, the obtained dicyclopentadiene resins have long been used because of their suitability for body parts of construction machinery for impact resistance. The industrial tungsten catalyst has been synthesized from tungsten hexachloride, *t*-butyl alcohol, dodecylphenol, and acetylacetone. (Fig. 1(c)) [5]. The molecular structure of the soluble precatalyst has been unknown since its birth. To produce better resins with excellent physical properties, the molecular precatalyst must be improved, which requires the development of new industrial complexes for the bulk polymerization.

As is widely known, the metathesis reaction of olefins was awarded the Nobel Prize in Chemistry in 2005 [6]. Group 6 catalyst systems are well-known molybdenum and tungsten systems developed by Schrock [7]. Excellent results, including stereoselective metathesis reactions, have been reported by so many research groups worldwide [8]. Even though the Nobel Prize was awarded, many research subjects remain in the olefin metathesis, especially in large-scale industrial production of resins. One of the targets is the tungsten complex for the precatalyst for the bulk polymerization of dicyclopentadiene [9, 10].

¹H NMR analysis of the commercial tungsten complexes of the bulk metathesis polymerization.

First, we attempted to analyze the tungsten precatalyst by ¹H NMR in the solution directory. The dark red oil precatalyst dissolves well in liquid hydrocarbon monomers. **Figure 2** shows the ¹H NMR spectrum of the catalyst obtained by the

reaction described in Fig. 1(d). Two samples synthesized under the same condition gave different signals, the red and the blue, respectively. The two spectra are mismatched chemical shifts, and it is clear that the preparation of the precatalyst is not reproducible. In addition, no reproducibility was observed in the ¹H NMR, even after repeated experiments such as changing the concentration and reaction temperature. The physical properties of the resin obtained by bulk polymerization of dicyclopentadiene

Fig. 1 Historical evolution of tungsten catalysis for the production of dicyclopentadiene resin.

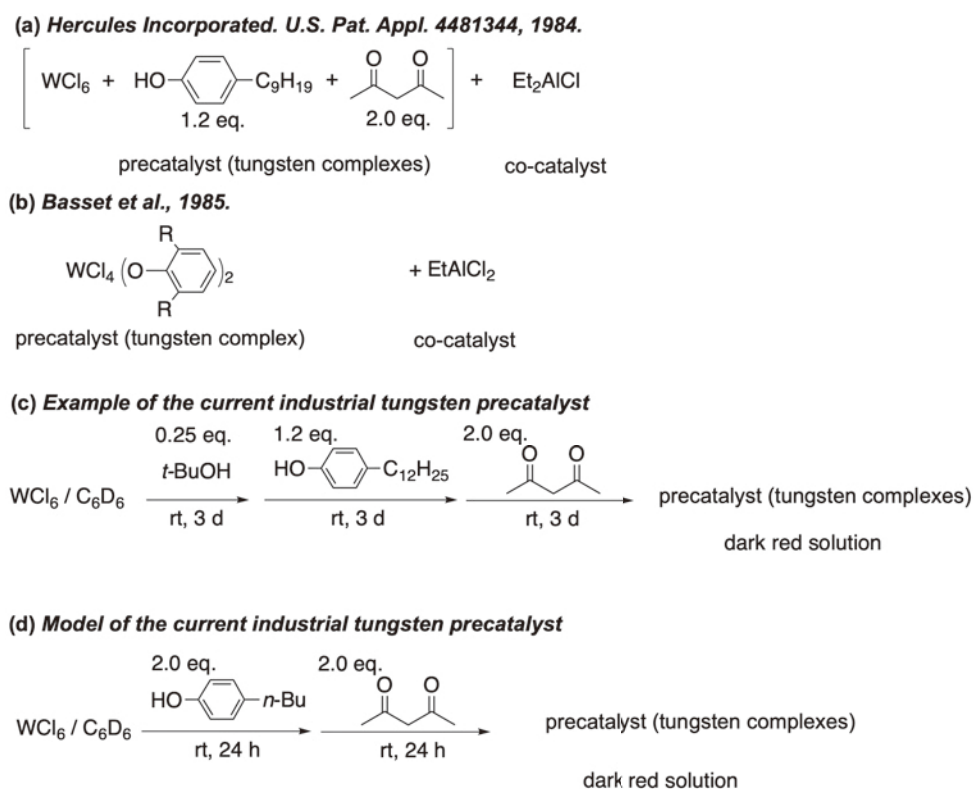
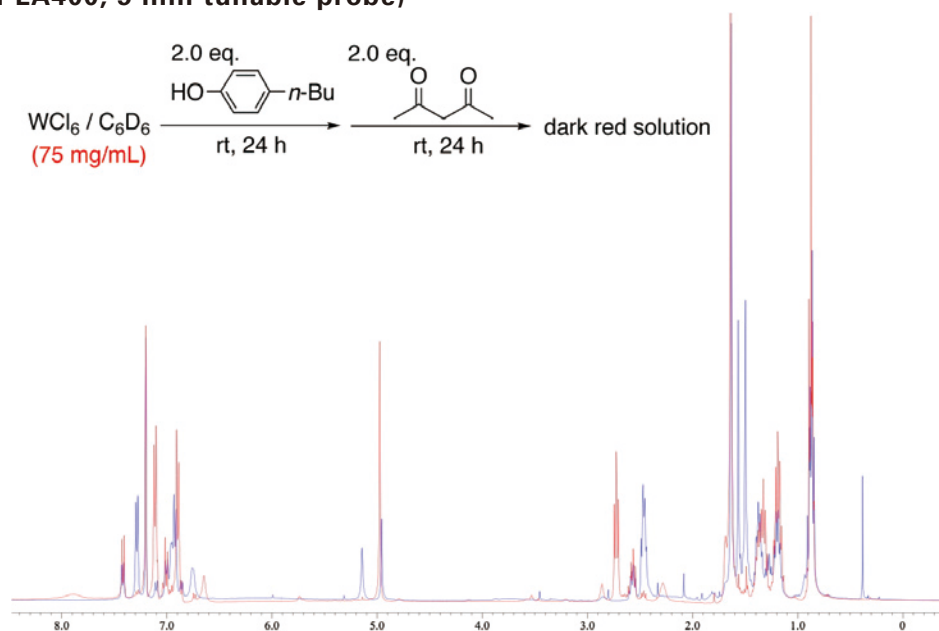


Fig. 2 ¹H NMR spectra of the tungsten precatalyst similar to the current industrial precatalyst. (JNM-LA400, 5 mm tunable probe)



using this tungsten precatalyst were reproducible. Thus, the complex signals observed in ^1H NMR (Fig. 2) do not directly correspond to the catalytic performance. Most of the components observed in the solution may not function as catalysts and are buried in a myriad of signals. We also attempted the stepwise preparation of the precatalyst. However, the results were not reproducible, and the molecular structure of the precatalyst remained unknown.

The challenge of ^{183}W ($I = +1/2$) NMR in solution

The reaction center of the catalytic component is undoubtedly tungsten. As described above, our efforts focused on observing protons by ^1H NMR. Direct observation of the tungsten atom should be a straightforward approach to detecting how many tungsten species exist in the solution. At sometime, we noticed that ^{183}W is $I = +1/2$.

The resonance frequency of ^{183}W is 25 MHz (at ^1H 600 MHz), and its relative sensitivity is 6% of ^{13}C . A ^{183}W NMR spectrum indicates a sharp signal due to $I = +1/2$ [11], despite its low sensitivity. The relaxation time of ^{183}W is reported as very long. A longer relaxation delay after each scan is required, thus resulting in a longer measurement time.

In February 2014, we visited the Instrument Center of the Institute for Molecular Science, Okazaki, in Japan, where a 10 mm low-frequency probe available with the 600 MHz magnet system. We heard the NMR system successfully detected the ^{183}W signals of heteropolyacids in water. After manually tuning the 10 mm probe the NMR myself, the ^{183}W signal of the NaWO_4 in D_2O was immediately detected. In contrast with the standard sample, our tungsten samples (100 mg in a 10 mm tube) showed no signal even after one day. ^{183}W NMR measurements are relatively common for an heteropolyacid, as mentioned above, but there are a few examples for organometallic complexes [11]. For example, the book published in 2012 [12] describes ^{183}W NMR of heteropoly acids of tungsten [13]. In addition, the results of measurements of tungsten imido complexes are

given in the section on ^{15}N NMR, where the ^{15}N - ^{183}W coupling constant is provided [14]. Braun *et al.* [15] describe detailed measurement conditions for ^{47}Ti and ^{49}Ti measured with a 500 MHz spectrometer, including the measurement time required. For ^{183}W , some references describe the measurement conditions in some detail [16, 17]. It was hard to believe that only 10 mg of sample in a 5 mm tube could be measured even though the molecule had hydrogen atoms directly bonded to tungsten. We needed help finding more practical information for us.

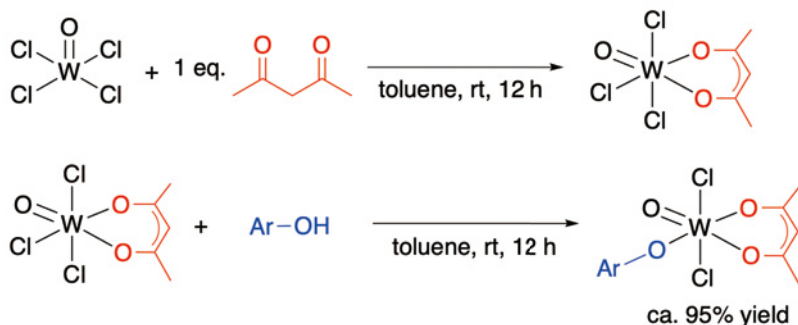
In March 2014, we tried to measure the same samples for three days and still saw no signal. We asked JEOL Ltd. to help measure the samples because we wondered if our measurement conditions needed to be more appropriate. No signal was observed despite the dedication of the technicians. Due to the situation, we decided to give up the ^{183}W NMR measurement and concentrate on another tungsten complex synthesis.

Concerning the conventional method shown in Fig. 2, phenols and diketones were chosen as organic ligands for synthetic studies of new tungsten complexes. Oxotetrachlorotungsten (WOCl_4) was chosen as a starting tungsten material, and a known diketone complex [18] was obtained successfully. Treatment of the acetylacetonate complex with a phenol derivative afforded a six-coordinate tungsten complex in high yield (two-step synthesis method (Fig. 3(a)). In addition, one-pot synthesis was also achieved. (Fig. 3(b)). The new one-pot method for oxotungsten complexes gave the multi-gram-scale synthesis of desired tungsten complexes. These obtained tungsten complexes are extremely soluble in hydrocarbon as a solvent. This is because our target tungsten complexes are for bulk polymerization, and the liquid phase, dicyclopentadiene, is an aliphatic hydrocarbon. The insoluble tungsten complexes are unsuitable, and the synthesis of tungsten complexes easily soluble in hexane has been several years of our synthetic work (Fig. 3) [19].

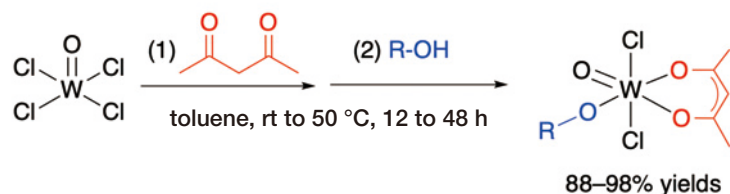
We again asked JEOL Ltd. to perform ^{183}W NMR measurements of the newly synthesized tungsten complexes. The sample weight was five times (500 mg) than four years ago, and a photograph of the powdered tungsten complex in 10

Fig. 3 Synthetic method for new tungsten complexes as a precatalyst.

(a) Two step synthesis



(b) One-pot synthesis



mm tubes is shown in **Fig. 4**. The solubility of the sample was greatly enhanced by replacing the acetylacetonate (red part in Fig. 3) with dipivaloylmethane. Surprisingly, a singlet signal of sufficient intensity was observed the next day by the overnight measurement of 400 MHz NMR (**Fig. 5**). The reason why the intense signal was visible was quite simple. In NMR, a low-sensitive analytical technique, we filled the sample tube with a high-purity sample in a high concentration.

In 2019, we synthesized a tungsten complex containing a silicon atom and determined its molecular structure, including single crystal X-ray structure analysis (**Fig. 6**). ^{183}W NMR of this tungsten complex at JEOL Ltd. showed that the signal splits into two in the case of non-decoupling conditions (**Fig. 7(b)**). The coupling constant is 3 Hz. In ^1H decouples conditions, $^{183}\text{W}\{^1\text{H}\}$, the signal appeared as a singlet signal (Fig. 7(a)). ^1H decoupling sequence, “single_pulse_dec.jp”, is often used in multinuclear NMR. There are no protons near the tungsten atom of the silicon-containing tungsten complex. Hence, the structural formula seems to be irrelevant without decoupling. The 3 Hz coupling indicated that the structural formula suggests a $^4J_{\text{HW}}$ long-range coupling.

Next, we prepared a tungsten complex with the expected $^3J_{\text{HW}}$ coupling observed. The results with a non-decoupling measurement are shown in **Fig. 8**. Three peaks were observed ($^3J_{\text{HW}} = 3$ Hz), just as we predicted. Moreover, Dr. Koshino at RIKEN measured these samples using a special 5 mm probe (JEOL JNM-ECZ600R, 60T5L/FG3 probe), including NOE and HMBC measurements. These long-range coupling, such as $^3J_{\text{HW}}$ and $^4J_{\text{HW}}$, are not always observed in the corresponding tungsten complexes. It should be noted that these well-defined molecular precatalysts have been experimentally confirmed to perform well in the bulk polymerization of dicyclopentadiene [19].

Effects of a relaxation agent and setting of the relaxation delay time

Adding a relaxation agent, a paramagnetic reagent, can shorten the relaxation time of the nucleus to be observed. This makes it possible to shorten the one scan time and gain the number of measurement samples within a certain period of time. **Figure 9** shows the $^{183}\text{W}\{^1\text{H}\}$ NMR charts with the relaxation delay time changed from the usual 20 s to 1 s. The 500 mg tungsten complex with 20 mg of $\text{Cr}(\text{acac})_3$, a total of 500 scans, and the measurement time was only 30 minutes with a relaxation delay of 2 s. The S/N value is about 9, sufficient to confirm the

Fig. 4



500 mg tungsten complex in 10 mm NMR tubes (left and center).
Conventional 5 mm NMR tube.

Fig. 5 Our first signal of ^{183}W NMR measurement.

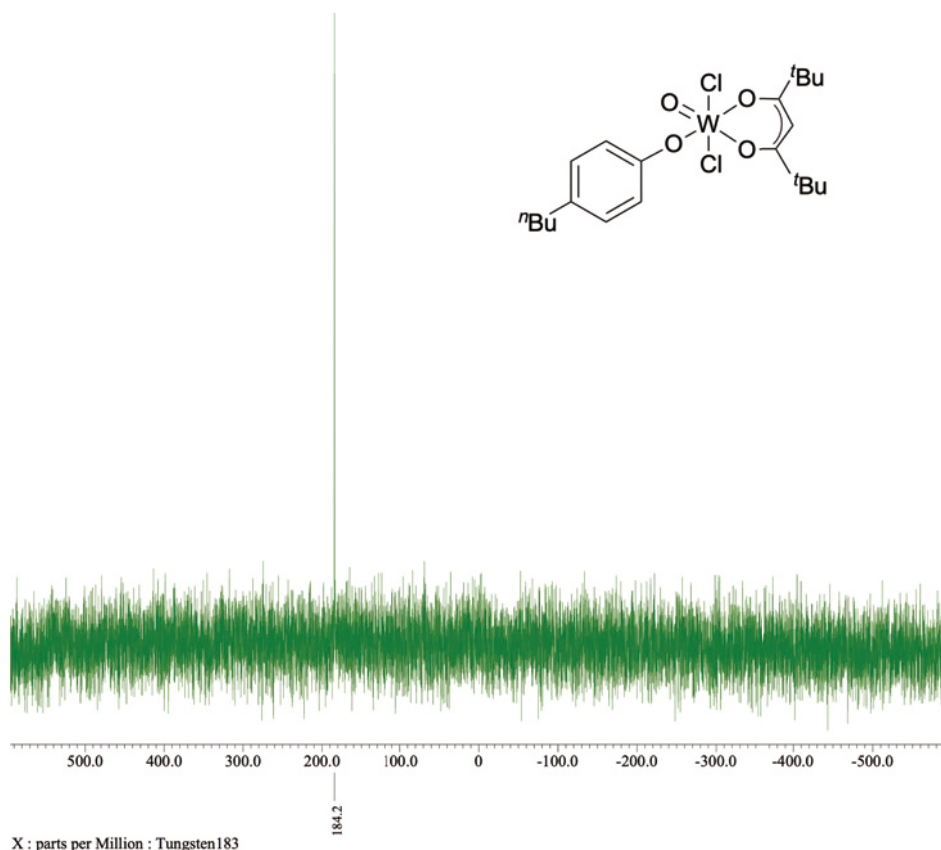
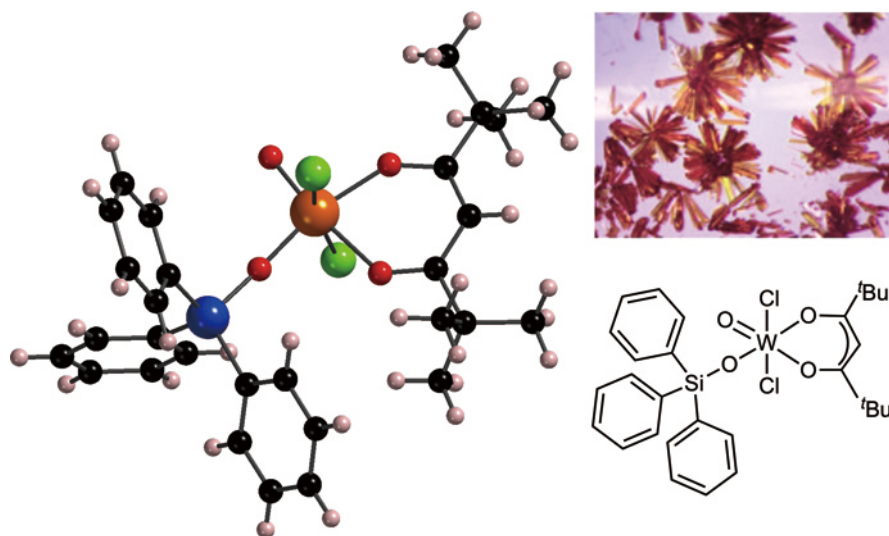
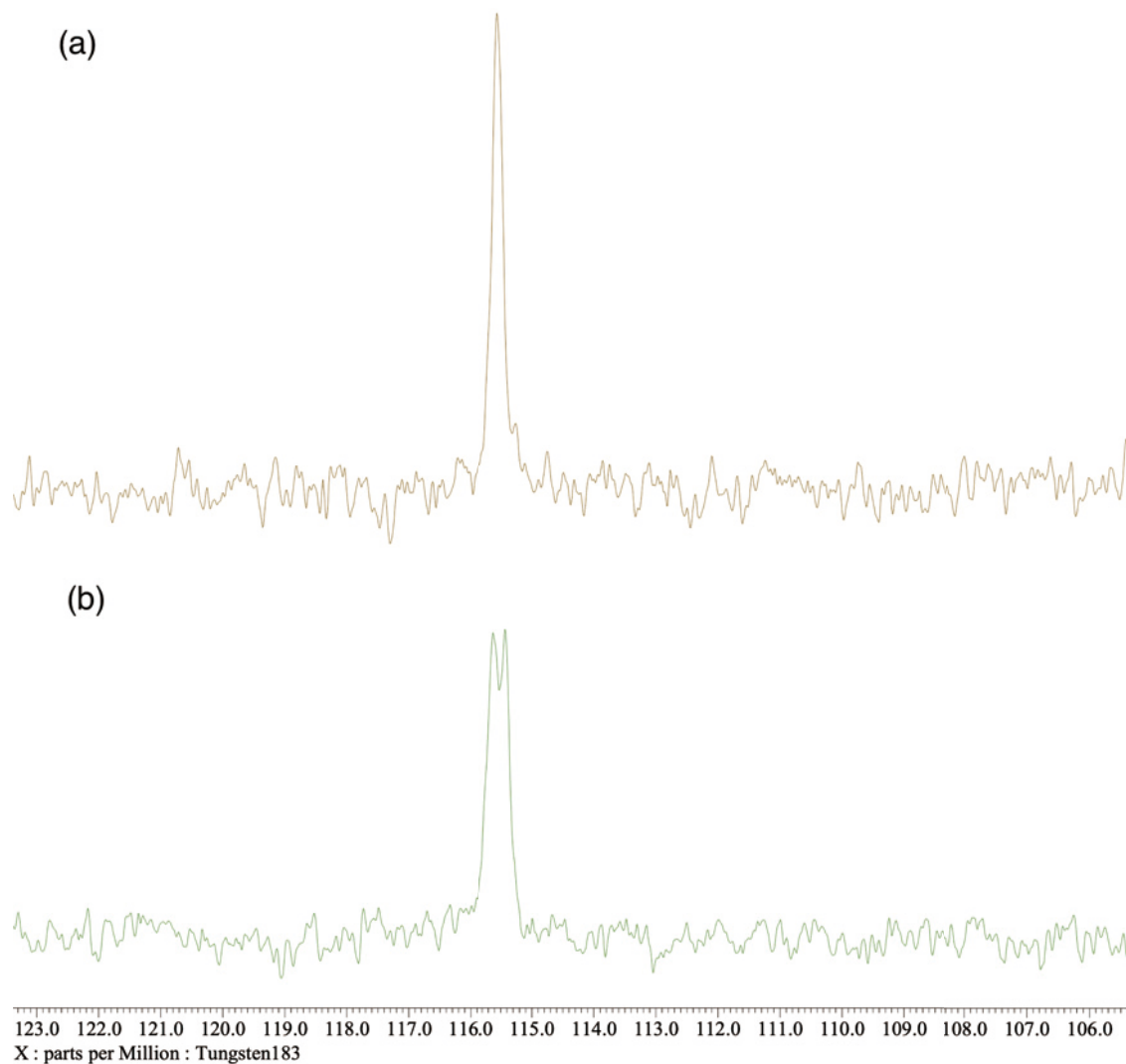


Fig. 6 Molecular structure of the tungsten complex containing Si atom.



The molecular structure was determined by X-ray crystallographic analysis (left). Photo of the crystals (upper right).

Fig. 7 ^{183}W NMR signals of the tungsten complex containing Si atom. (JNM-ECZ400S, T10L probe)



(a) ^1H decouple, (b) non-decouple.

^{183}W chemical shift. Of course, a relaxation delay time can be estimated by measuring the relaxation time for ^{183}W only on the premise that the ^{183}W signal is visible.

The problem with the relaxation agent is that it may react with the sample to be measured. It is necessary to compare the spectra measured with no relaxation agent. Having understood this point, the question arises whether the relaxation reagent is unnecessary. We detected the $^{183}\text{W}\{^1\text{H}\}$ signals under the measurement conditions with 2 s relaxation delay without using $\text{Cr}(\text{acac})_3$. It was found that these tungsten complexes can be measured with relaxation delay time of 1 s, which is only one-tenth of 20 s.

Routine measurement of ^{183}W NMR and complexes with no signal

After such a trial and error, we can now routinely measure ^{183}W solution NMR. The standard conditions are as follows.; the sample weight is about 500 mg, 30-degree flip angle, 2 s relaxation delay time. About 1024 scans take 1 to 3 hours, depending on decouple conditions. The setting is simple; we select standard single_pulse_dec.jxp, chose ^{183}W as the observed nuclei, and set a relaxation delay of 20 s. Using deuterio solvents in terms of a stable lock signal is preferable. If an automatic sample changer, JackBean 30, is available, the measurement can be fully automated, except for manual tuning for a nuclei observation. The most crucial point for observing low-sensitive nuclei is how to obtain high-purity samples on a gram scale.

On the other hand, there are some complexes with similar structures for which no signals were observed. We attempted various measurement conditions, such as solvent and the relaxation delay time of 100 s. Searching the signals from +3000

to -4000 ppm, there were no resonances. Typical examples are summarized in Fig. 10.

Conclusions

We have observed ^{183}W solution NMR of tungsten precatalysts for homogeneous metathesis polymerization of cycloolefins. The critical point in detecting the low-sensitive ^{183}W nuclide was to obtain pure samples in a multi-gram scale. We reaffirmed that NMR spectroscopy is inherently a low-sensitive analytical method in principle. In addition, we recognized the importance of multinuclear NMR measurement. There are great possibilities for multinuclear NMR; for example, we tried ^{29}Si solution NMR to clarify the problem in preparing the silicon-containing complex in Fig. 6.

The correlation between chemical shifts and molecular structures in ^{183}W NMR still needs to be clarified, and we must continue accumulating examples. Copért, Fürstner, and co-workers reported the ^{183}W solution NMR measurements of tungsten alkylidyne complexes [20]. Recently, ^{95}Mo NMR measurements and catalytic properties of molybdenum complexes have been reported. Theoretical calculations have also analyzed the ^{95}Mo chemical shift tensor and ^{95}Mo solid-state NMR spectra. The observed chemical shift values have been correlated with the HOMO and LUMO of the molybdenum center [21]. In an earlier paper, ^{95}Mo solution NMR measurements were presented [22]. These reports show that an NMR spectroscopy of low-frequency nuclei provides scientifically valuable information. We will continue to study the structure of transition metal complexes in the liquid phase utilizing multinuclear NMR.

Fig. 8 ^{183}W NMR spectrum of the tungsten complex having a hexyloxy ligand. (JNM-ECZ600R, T10L probe)

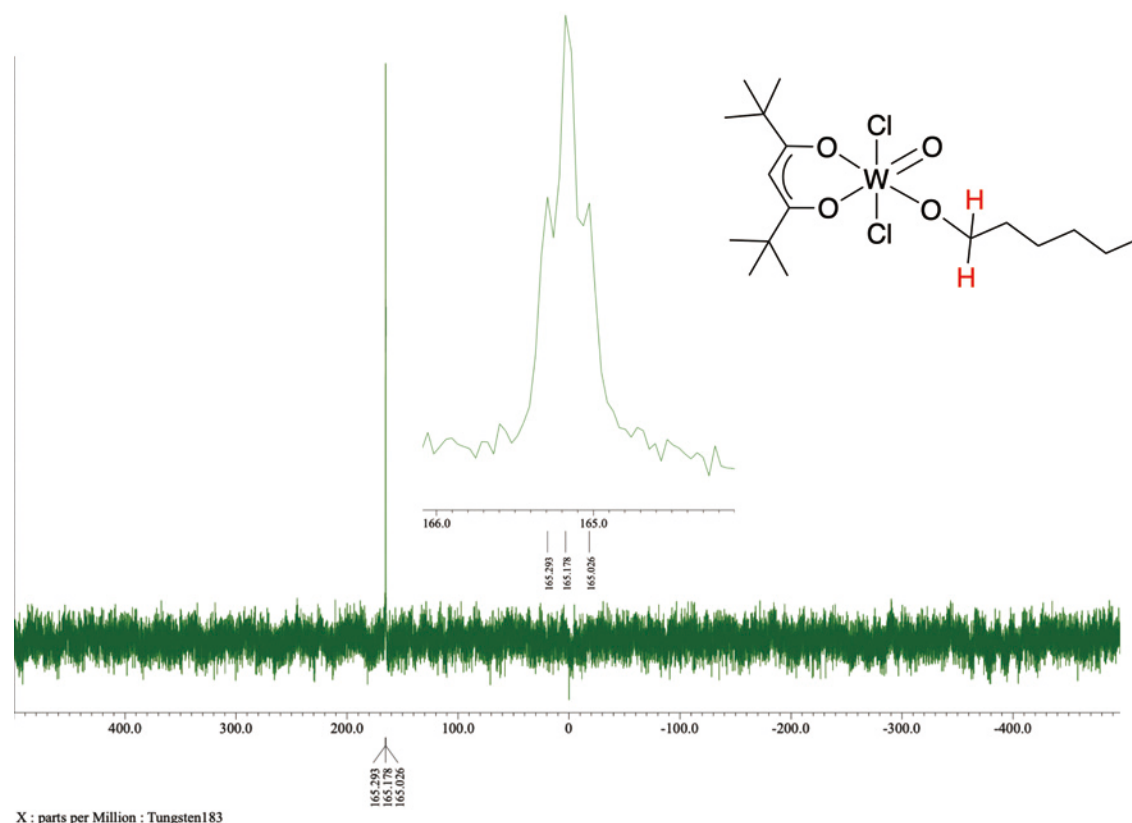
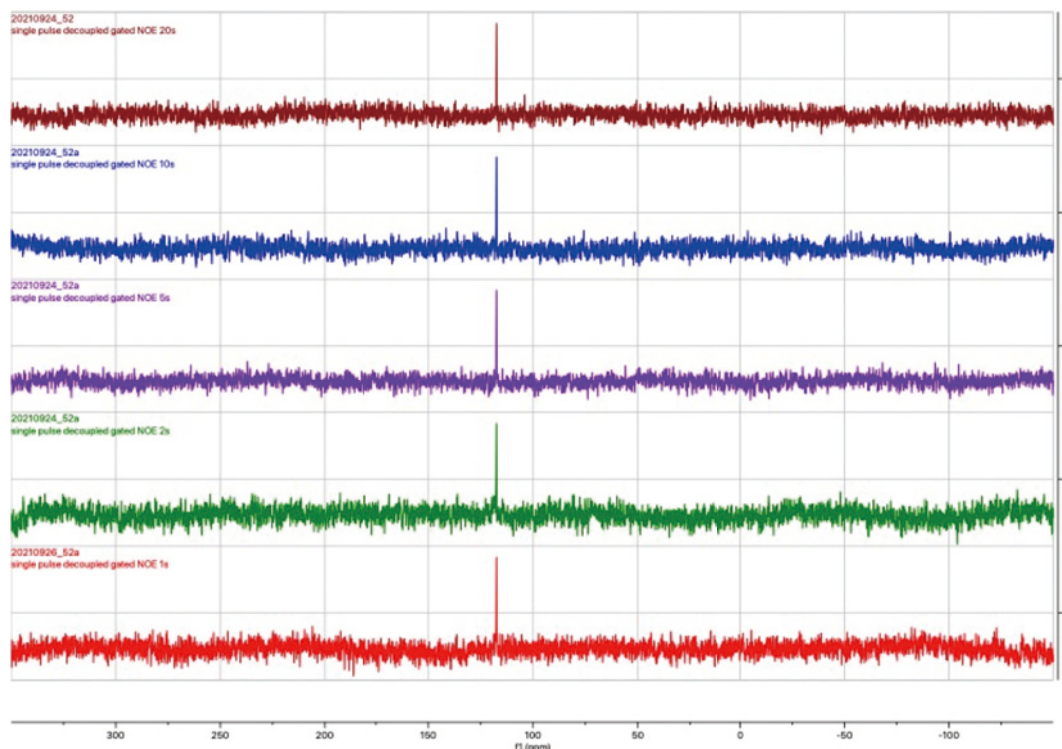
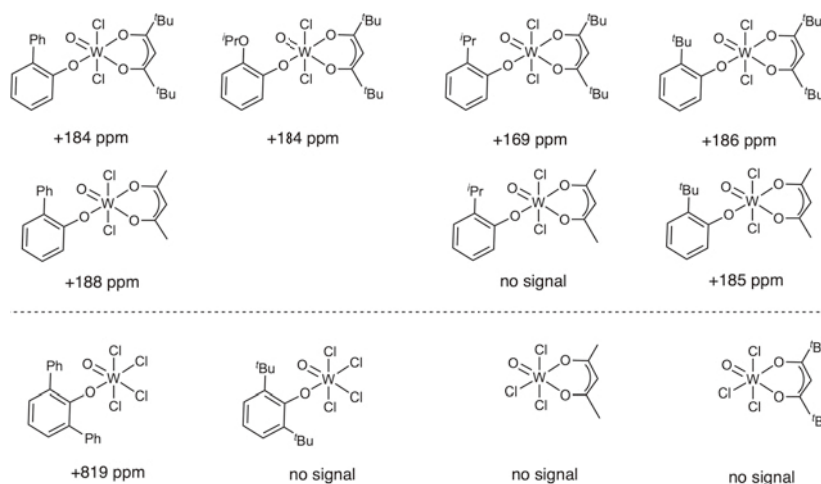


Fig. 9 $^{183}\text{W}\{^1\text{H}\}$ NMR spectrum with $\text{Cr}(\text{acac})_3$ as a relaxation agent. (JNM-ECZ600R, T10L probe)



Relaxation times are from 20, 10, 5, 2, 1s.

Fig. 10 Examples of ^{183}W NMR chemical shifts in C_6D_6 . (JNM-ECA600, T10L probe and JNM-ECZ600R, T10L probe)



Acknowledgments

A part of this work was conducted in Institute for Molecular Science, supported by "Advanced Research Infrastructure for Materials and Nanotechnology in Japan (ARIM)" of the Ministry of Education, Culture, Sports, Science and Technology (MEXT)." Proposal Numbers JPMXP1222MS1041b and JPMXP1222MS1041. A part of this work was conducted in Institute for Molecular Science, supported by Nanotechnology Platform Project (JPMXP09S21MS1068, JPMXP09S20MS1040, JPMXP09S19MS1086) from the Ministry of Education, Culture, Sports, Science and Technology of Japan.

The Science and Technology Promotion Project of Okayama Prefecture supported the synthesis of tungsten complexes. RIMTEC Corporation invested in part of this work (e.g., complex synthesis). We are deeply grateful to Haruyo Nagao at the Instrument Center, Institute for Molecular Science, Dr. Hiroyuki Koshino at the Center for Sustainable Resource Science, and Masato Taki at the Nagoya Institute of Technology for ^{183}W NMR measurements. We thank Associate Professor Kosuke Katagiri, Faculty of Science and Engineering, Konan University, for single crystal X-ray structure analysis. We thank and honor the many employees of JEOL Ltd. for their dedicated cooperation over the years.

References

- [1] Hercules Incorporated. U.S. Pat. Appl. 4481344, 1984.
- [2] Breslow, D. S. Metathesis Polymerization. *Prog. Polym. Sci.* **18**, 1141–1195 (1993).
- [3] Quignard, F.; Leconte, M.; Basset, J. M. *J. Mol. Catal.* **28**, 27–32 (1985).
- [4] Bell, A. Aryloxide Derivatives of Tungsten Oxytetrachloride as Ring-Opening Metathesis Polymerization Catalysts. *J. Mol. Catal.* **A76**, 165–180 (1992).
- [5] Ivin, K. J.; Mol, J. C. Olefin Metathesis and Metathesis Polymerization, Academic Press (1997).
- [6] (a) Chauvin, Y. Olefin Metathesis: The Early Days (Nobel Lecture). *Angew. Chem. Int. Ed.* **45** (23), 3740–3747 (2006). <https://doi.org/10.1002/anie.200601234>. (b) Schrock, R. R. Multiple Metal–Carbon Bonds for Catalytic Metathesis Reactions (Nobel Lecture). *Angew. Chem. Int. Ed.* **45** (23), 3748–3759 (2006). <https://doi.org/10.1002/anie.200600085>. (c) Grubbs, R. H. *Angew. Chem. Int. Ed.* **45**, 3760 (2006). DOI:10.1002/anie.200600680
- [7] (a) Schrock, R. R. High-Oxidation-State Molybdenum and Tungsten Alkylidyne Complexes. *Acc. Chem. Res.* **19** (11), 342–348 (1986). <https://doi.org/10.1021/ar00131a003>. (b) Schrock, R. R. High Oxidation State Multiple Metal–Carbon Bonds. *Chem. Rev.* **102** (1), 145–180 (2002). <https://doi.org/10.1021/cr0103726>. (c) Copéret, C.; Berkson, Z. J.; Chan, K. W.; Silva, J. de J.; Gordon, C. P.; Pucino, M.; Zhizhko, P. A. Olefin Metathesis: What Have We Learned about Homogeneous and Heterogeneous Catalysts from Surface Organometallic Chemistry? *Chem. Sci.* **12** (9), 3092–3115 (2021). <https://doi.org/10.1039/d0sc06880b>. (d) Schrock, R. R.; Copéret, C. Formation of High-Oxidation-State Metal–Carbon Double Bonds. *Organometallics* **36** (10), 1884–1892 (2017). <https://doi.org/10.1021/acs.organomet.6b00825>.
- [8] (a) Dawood, K. M.; Nomura, K. Recent Developments in Z-Selective Olefin Metathesis Reactions by Molybdenum, Tungsten, Ruthenium, and Vanadium Catalysts. *Adv. Synth. Catal.* **363** (8), 1970–1997 (2021). <https://doi.org/10.1002/adsc.202001117>. (b) Buchmeiser, M. R. Functional Precision Polymers via Stereo- and Regioselective Polymerization Using Group 6 Metal Alkylidene and Group 6 and 8 Metal Alkylidene N-Heterocyclic Carbene Complexes. *Macromol. Rapid Commun.* **40** (1), 1800492 (2019). <https://doi.org/10.1002/marc.201800492>. (c) Buchmeiser, M. R. Molybdenum Imido, Tungsten Imido and Tungsten Oxo Alkylidene N-Heterocyclic Carbene Olefin Metathesis Catalysts. *Chem. Eur. J.* **24** (54), 14295–14301 (2018). <https://doi.org/10.1002/chem.201802497>.
- [9] (a) Slugovc, C. Industrial Applications of olefin metathesis polymerization. In *Olefin Metathesis*; Grell, K. Ed.; John Wiley & Sons, 2014; pp 329–333. (b) Dragutan, V.; Dragutan, I.; Dimonie, M.; Couve, C.; Abadie, M. Catalyst activity and selectivity in ROMP of dicyclopentadiene induced by some tungsten systems. In *Ring Opening Metathesis Polymerization and Related Chemistry*; Khosravi, E.; Szymanska-Buzar, T. Eds.; Kluwer Academic Publishers, 2000; pp 465–476.
- [10] Kamada, M.; Oshiki, T., *J. Synth. Org. Chem. Jpn.* **75**, 111–120 (in Japanese) (2017).
- [11] (a) Murnakata, M.; Kitagawa, S.; Shibata, S. Introduction of multinuclear NMR (1991) Kodansha scientific books (in Japanese). (b) Kitagawa, S.; Mizuno, M. Maekawa, M. Multinuclear NMR in solution and solid state (2008) Sankyo Shuppan Co., Ltd. (in Japanese).
- [12] Pregosin, P. S. NMR in Organometallic Chemistry (2012) WILEY-VCH.
- [13] Kazansky, L. P.; Yamase, T. Electronic Population on Tungsten, Molybdenum, and Vanadium Atoms and ¹⁸³W, ⁹⁵Mo, and ⁵¹V NMR in Polyoxometalates. *J Phys Chem* **108** (30), 6437–6448 (2004). <https://doi.org/10.1021/jp0485993>.
- [14] Glassman, T. E.; Vale, M. G.; Schrock, R. R. Synthesis and Characterization of a Series of (Pentamethylcyclopentadienyl) Tungsten(V) and -(VI) Amino, Amido, Imido, and Bridging Nitrido Complexes and Molybdenum Analogs. *Organometallics* **10** (12), 4046–4057 (1991). <https://doi.org/10.1021/om00058a020>.
- [15] Braun, S.; Kalinowski, H. -O.; Berger, S. 150 and more Basic NMR Experiments 1996. WILEY-VCH.
- [16] (a) Benn, R.; Brevard, C.; Rufinska, A.; Schroth, G. Direct and Indirect Recording of Tungsten-183 NMR Spectra, and Structure Determination of (Diene)3M (M = Tungsten, Molybdenum) Compounds in Solution. *Organometallics* **6** (5), 938–942 (1987). (b) Benn, R.; Brenneke, H.; Heck, J.; Rufinska, A. Rapid Access to Tungsten-183 NMR Parameters of Tungsten Complexes via Reverse 2D Proton-Tungsten-183 and Phosphorus-31-Tungsten-183 NMR Spectroscopy. *Inorg. Chem.* **26**, 2826–2829 (1987). <https://doi.org/10.1021/ic00264a021>. (c) Benn, R.; Rufinska, A. Indirect Two-dimensional Heteronuclear NMR Spectroscopy of Low-γ Metal Nuclei (M = ¹⁸³W, ⁵⁷Fe, ¹⁰³Rh, ⁶¹Ni). *Magn. Reson. Chem.* **26** (10), 895–902 (1988). <https://doi.org/10.1002/mrc.1260261015>.
- [17] Templeton, J. L.; Philipp, C. C.; Pregosin, P. S.; Rügger, H. ¹⁸³W–H Long-range Shift Correlation and ¹H NOESY Studies on Tungsten(II) Hydrido–Pyrazolylborate Complexes. *Magn. Reson. Chem.* **31** (1), 58–62 (1993). <https://doi.org/10.1002/mrc.1260310112>.
- [18] (a) Drew, M. G. B.; Fowles, G. W. A.; Rice, D. A.; Shanton, K. J. Dimerization and Condensation of Pentane-2,4-Dione by MOC1, [M=Mo or W]. *J. Chem. Soc., Chem. Commun.* **5** (47), 614–615 (1974). <https://doi.org/10.1002/chin.197447322>. (b) Sergienko, V. S.; Abramenko, V. L.; Churakov, A. V. Specific Features of the Structure of Tungsten(VI) Mononuclear Six-Coordinate Oxohalide Complexes: A Review. *Crystallography Reports* **54** (5), 770–792 (2009). <https://doi.org/10.1134/s1063774509050095>.
- [19] RIMTEC Corporation, Kamada, M.; Oshiki, T. PCT/JP2019/041320.
- [20] Hillenbrand, J.; Leutzsch, M.; Gordon, C. P.; Copéret, C.; Fürstner, A. ¹⁸³W NMR Spectroscopy Guides the Search for Tungsten Alkylidyne Catalysts for Alkyne Metathesis. *Angew. Chem. Int. Ed.* **59** (48), 21758–21768 (2020). <https://doi.org/10.1002/anie.202009975>.
- [21] Berkson, Z. J.; Lätsch, L.; Hillenbrand, J.; Fürstner, A.; Copéret, C. Classifying and Understanding the Reactivities of Mo-Based Alkyne Metathesis Catalysts from ⁹⁵Mo NMR Chemical Shift Descriptors. *J. Am. Chem. Soc.* **144** (33), 15020–15025 (2022). <https://doi.org/10.1021/jacs.2c06252>.
- [22] Hillenbrand, J.; Leutzsch, M.; Yiannakas, E.; Gordon, C. P.; Wille, C.; Nöthling, N.; Copéret, C.; Fürstner, A. “Canopy Catalysts” for Alkyne Metathesis: Molybdenum Alkylidyne Complexes with a Tripodal Ligand Framework. *J. Am. Chem. Soc.* **142** (25), 11279–11294 (2020). <https://doi.org/10.1021/jacs.0c04742>.

Introduction of Various Application Examples Obtained by Multi-Purpose TEM (JEM-F200) with Various Attachments

Kei-ichi Fukunaga EM Business Unit, JEOL Ltd.

Examples of observations, using the JEM-F200 with a field emission electron gun as a multi-purpose TEM and in-situ observation holders (heating, gas and liquid environments), will be presented. In addition, examples of electron holography analysis, which is effective for observation of magnetic domain structures in magnetic materials, and crystal orientation analysis using polycrystalline samples, will also be presented.

Introduction

A transmission electron microscope (TEM) is an observation instrument in which electrons are accelerated at a voltage of approximately 100 kV to 1000 kV to pass through a sample placed in a vacuum, and the transmitted electron beam is imaged to provide information on the shape and structure of the sample. The higher the accelerating voltage of the electron beam, the greater the penetration ability of the electron beam, making it possible to observe samples as thick as 1 μm , depending on the sample density. In addition, the higher the accelerating voltage, the shorter the wavelength of the electron beam, which allows finer spatial resolution and observation of finer structures. On the other hand, the accelerating tube for electron-beam acceleration becomes larger and the speed of the electron increases (about 94% of the speed of light at an accelerating voltage of 1000 kV), so the energy of the electron beam increases and the electromagnetic lens for refracting the electron beam needs to be enlarged accordingly. The 200 kV transmission electron microscope, the most widely available microscope on the market, which is reasonably sized to fit in a laboratory-level room, can perform observation at lower accelerations of 100 kV or less, and is used for observation and analysis in a wide range of fields including biology, polymers, semiconductors, ceramics, and metals. The JEOL JEM-F200, used as a general-purpose TEM, is a transmission electron microscope with a field emission electron gun and a maximum accelerating voltage of 200 kV. This TEM has various optional attachments. For example, the HR (High Resolution) pole piece has a spatial resolution of 0.1 nm for TEM lattice images and 0.14 nm for STEM (Scanning Transmission Electron Microscopy) images, and is used for tissue analysis in various fields as mentioned above. It is also used for microstructural analysis in the various fields mentioned above.

A sample holder is required for TEM observation for a variety of samples. Sample holders include holders that allow multiple samples to be placed simultaneously and double-tilt holders with a mechanism to tilt the sample. In addition, holders that can cool or heat samples and holders specialized for in-situ observation in gaseous

or liquid environments have also been developed. In addition, transmission electron microscopes have built-in ports for attachments, making it possible to retrofit special third-party cameras and other equipment. This paper describes examples of observations using various holders and various samples obtained by using attachments that can be attached to the main body of the TEM.

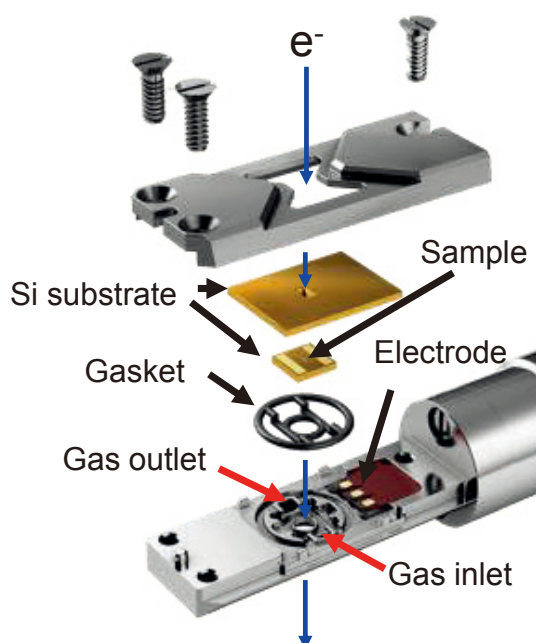
In-situ observation

In-situ observation has been used for many years to record how a sample changes over time by applying some physical action to the sample, such as temperature change, stress application, or charged particle irradiation. There are several objects to be observed and monitored in this "in-situ" observation, including changes in sample morphology (grain size change, precipitation, recrystallization, etc.) by microscopic images, changes in crystal structure (lattice constant, phase change, etc.) by electron diffraction patterns, composition changes by energy dispersive X-ray spectroscopy (EDS) and electron energy loss spectroscopy (EELS), and spectral changes reflecting bonding states by EELS, etc.

In-situ observation requires a special sample holder to provide physical stimuli to the sample. A gaseous environment requires modifications to the TEM main body, such as a vacuum system, or special devices, and was considered difficult to introduce and operate only at universities and large research facilities. In recent years, however, even commercially available standard TEMs can be used for observation in gaseous environments and in liquids using a dedicated specimen holder. These holders are fabricated using MEMS (Micro Electro Mechanical System) technology, which is a semiconductor integrated circuit manufacturing technology. The sample is held in the tiny environmental cell of the MEMS chip at the tip of the holder, and the environmental gas layer is made as thin as possible to enable observation of the sample in gas. By incorporating a heater for heating and electrodes capable of electrochemical measurement in this environmental cell, electrochemical reactions that occur in batteries, etc., can be observed at a set temperature. When heating, the sample is placed on or very

close to a thin-film heater. The thin-film heater has a smaller heat capacity than conventional furnace-type heating holders, resulting in faster temperature rise and lower sample drift. Various other specialized holders for in-situ observation are available from the manufacturer of the electron microscope itself or from third parties such as Protochips [1], DENS solutions [2], Hummingbird Scientific [3], or Mel-Build [4], for example. **Figure 1** shows a gas inlet system for a dedicated gas supply system, and shows a schematic diagram of the tip of a dedicated holder into which gas can be introduced. The tiny tip on which the sample is placed is separated from the vacuum region of the TEM column by a gasket, and the top and bottom of the sample are covered with a very thin silicon nitride film (several tens nm thick) on the tiny tip and the Si tip above the sample to allow transmission of electron beams. There are gas inlets and outlets around the sample, and these are connected to the holder handle by a thin tube.

Fig. 1 Schematic diagram of the tip of the holder for in-situ observation of gas environment.



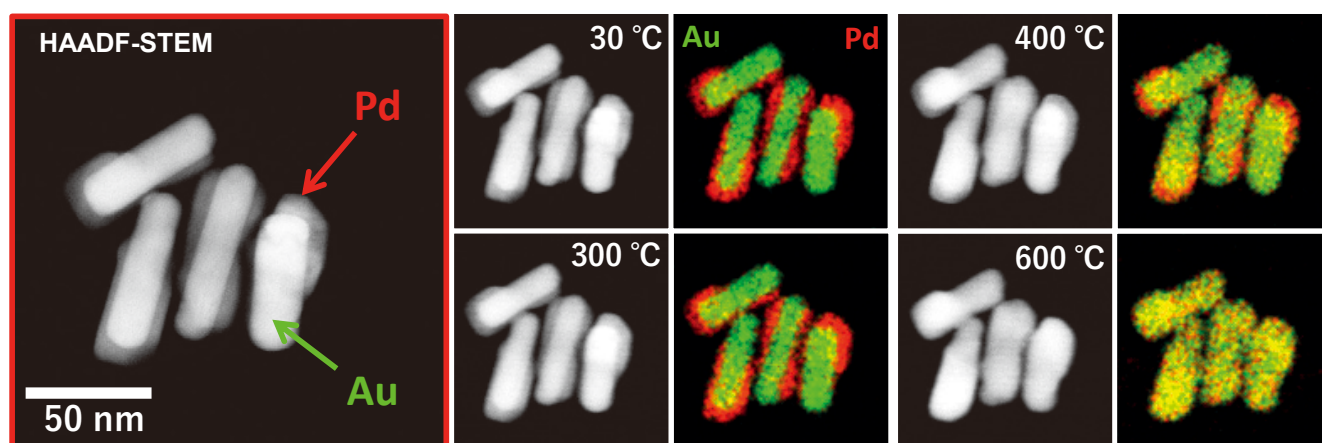
1. Observation of alloying process of core-shell metal nanoparticles in vacuum using a heating holder

Heating holders can be used to observe the sintering and alloying processes of ceramics and other materials. In this section, we present the results of in-situ observation of palladium-gold nanoparticles with a core-shell structure when heated. **Figure 2** shows the results of HAADF (high angle annular dark field)-STEM observation and EDS analysis at each temperature during heating from room temperature to 600 °C at a rate of 1000 °C/s. In the HAADF-STEM image at room temperature (left panel of Fig. 2), the core appears more intense (brighter) than the shell, suggesting that the core is Au (atomic number 79) and the shell is Pd (atomic number 46). When the sample temperature is increased in the order of 30, 300, 400, and 600 °C, the contrast of the core/shell boundary becomes unclear at 400 °C in HAADF-STEM, and this contrast disappears at 600 °C, and the core/shell structure seems to have disappeared. Elemental maps at each temperature by EDS in the same field of view area are shown to the right of each HAADF-STEM image. Green indicates Au and red indicates Pd. At room temperature of 30 °C, the core and shell are clearly color-coded. From 300 °C to 400 °C, the trend is the same, but the red part of the shell becomes indistinct. At 600 °C, the entire particle can be judged to be alloyed, consistent with the results from the HAADF-STEM image.

2. In-situ observation using a gas environment holder

Many examples of in-situ observation of catalyst particles using a gas environment holder have been reported for redox reactions [5, 6]. This holder also allows sample heating and gas partial pressure control in a gas environment, enabling in-situ observation under experimental conditions that are closer to real-world conditions. In this section, we present the results of in situ observations of the reduction-oxidation reaction of copper powder particles. The reaction temperature was 300 °C, and the initial condition was a nitrogen gas pressure of 10³ Pa. The reduction atmosphere was hydrogen gas at 10⁴ Pa, and the oxidation atmosphere was oxygen gas at 10⁴ Pa. The gas atmospheres were maintained for approximately one hour each, and STEM imaging and elemental mapping by EDS were performed. The results are shown in **Fig. 3**. Initially, an oxide layer was observed on the particle surface. The reduction reaction eliminates the oxide layer on the surface of the particles, and the copper particles tend to break down into smaller particles. It can be inferred that

Fig. 2 In-situ high-temperature observation of Au/Pd core-shell structure nanoparticles.



HAADF-STEM images and EDS elemental maps.

copper particles of several micrometers in size were originally agglomerated in the initial state. In the oxygen gas atmosphere, the oxygen signal becomes stronger and the oxygen is more uniformly present in the particles than in the initial state, suggesting that these particles are oxidized to copper oxide.

3. In-situ observation of electrochemical reactions using a holder with liquid cell

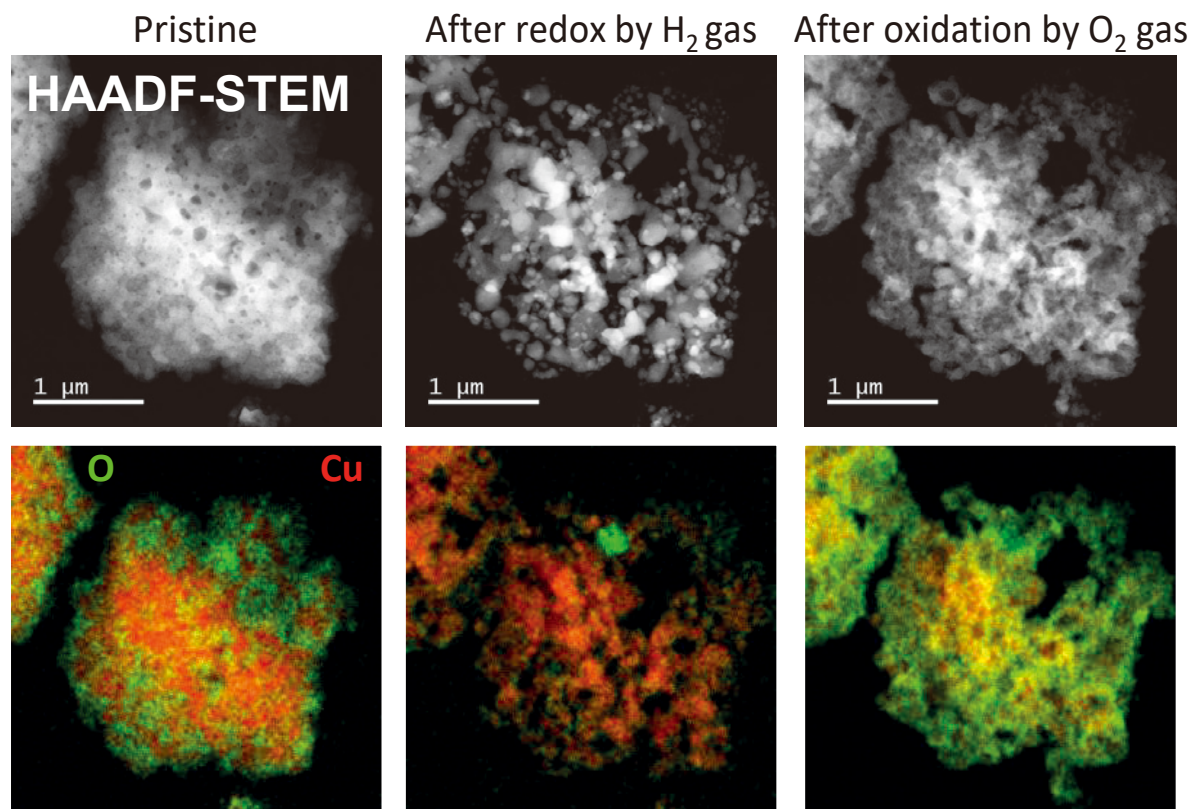
The liquid cell holder enables observation of nanoparticle dispersion in solution, and if an electrode can be introduced into the holder, in-situ TEM can be used to observe electrochemical reactions that occur in solution, such as plating processes and battery charging and discharging processes. In this section, we show the results of in-situ observation of the copper plating process. An aqueous copper sulfate solution was used as the electrolyte, and this solution was introduced into a cell equipped with electrodes. The electrodes were connected to an electrochemical measurement device with controllable voltage and current, and the process of copper deposition on the electrode surface was observed. **Figure 4** shows a series of bright-field images of the process. The dark contrast area from the center to the lower right is the electrode, and copper is deposited from its surface, with the thickness of the deposited layer increasing with time.

Crystal orientation analysis using precession electron diffraction patterns

Precession electron diffraction is a technique for acquiring electron diffraction patterns that are less affected by kinetic

effects by obliquely irradiating an electron beam onto a sample [7]. To acquire data, a circuit that enables oblique irradiation is built into the deflection coil of the electron microscope body as an attachment. In addition, an exclusive camera is attached to the port of the electron microscope to acquire electron diffraction patterns. The device used for this analysis is a Manomegas P-2010. **Figure 5** shows the appearance of the camera, which is equipped with a retractable camera as indicated by the arrow. To acquire precession electron diffraction patterns, the electron beam is focused and scanned two-dimensionally on the sample like a STEM (Scanning Transmission Electron Microscope), and electron diffraction patterns from each position are captured at high speed to create a data cube. The converged electron beam has precession, but the spatial resolution is approximately the same because the electron beam is narrowed to about 1 nm on the sample. The electron beam is preset to be focused but with a small angle, so the diffraction spots do not have the disk-like spread seen in CBED (Convergent-Beam Electron Diffraction), but are almost spotted. The crystal orientation can be determined from the obtained data cubes, and a crystal map can be created accordingly. **Figure 6** shows an example of crystal orientation analysis of a commercially available Au nanoparticle with a diamond shape. The center of the figure shows a color map of the crystal orientation. The color map is red for $\langle 001 \rangle$, green for $\langle 011 \rangle$, and blue for $\langle 111 \rangle$. Each rhombic particle has a different crystallographic orientation on the right side (blue) and on the left side (green), indicating that the rhombic particles are composed of multiple crystals. Since Au has a face-centered cubic crystal structure, we analyzed Au in detail and found that the grain boundaries indicated by the green-red and red-blue

Fig. 3 In-situ observation of reduction by hydrogen and oxidation by oxygen using a gas environment holder.



The upper panel shows HAADF-STEM images and the lower panel shows EDS elemental maps. Green and red indicate the distribution of oxygen and copper, respectively.

relationships are $\Sigma 3$ and $\Sigma 9$ grain boundaries, respectively. The Au crystal structure is a face-centered cubic structure.

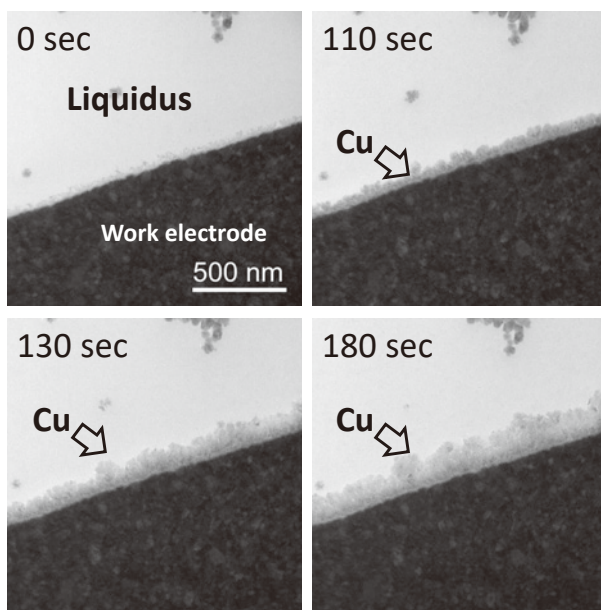
Magnetic field analysis by holography

Electron holography is a technique that can measure electric and magnetic fields [8, 9]. **Figure 7** shows a schematic diagram. A conductive thin wire of less than a few micrometers called a bi-prism is introduced into the electron beam path in a transmission electron microscope. When a positive voltage is applied to it, the electron beam is deflected toward the biprism, as shown in the figure, because electrons are negatively charged.

In the area where the left electron beam (Φ_1) transmitted through the vacuum and the right electron beam (Φ_2) overlap in the image plane, interference fringes are formed as shown in the schematic diagram. Since the phase of the electron beam penetrated through the sample is modulated (wavelength changes) by the electric and magnetic fields, the interference fringes formed by the overlap of Φ_1 and Φ_2 are shifted or bent to reflect it. By analyzing the degree of the shift, the magnetic and electric fields within the sample can be visualized.

Figure 8 shows a series of electron holography results obtained by preparing a thin film from a commercial neodymium magnet for TEM observation using a JEOL FIB system (JIB-

Fig. 4 In-situ observation of the copper deposition process using a liquid cell holder.



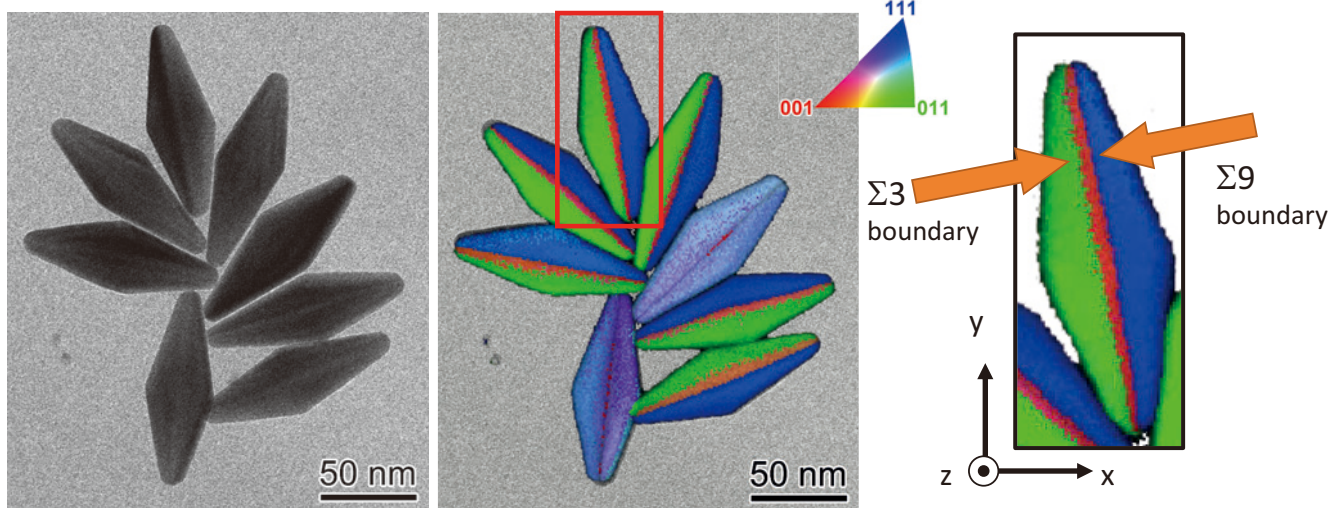
The lower right in each image is the electrode, and a gray contrasting copper precipitation layer is observed growing from the electrode surface.

Fig. 5 External view of the attachment for acquiring precession electron diffraction.



A camera for acquiring diffraction patterns is built in the area indicated by the arrow.

Fig. 6



TEM image of diamond-shaped Au nanoparticles (left). In the middle is a crystallographic orientation map in the same field of view. The color definition in the direction toward the surface of the paper is also shown.

Fig. 7 Diagram of the electron beam path in hologram formation using an electron beam biprism.

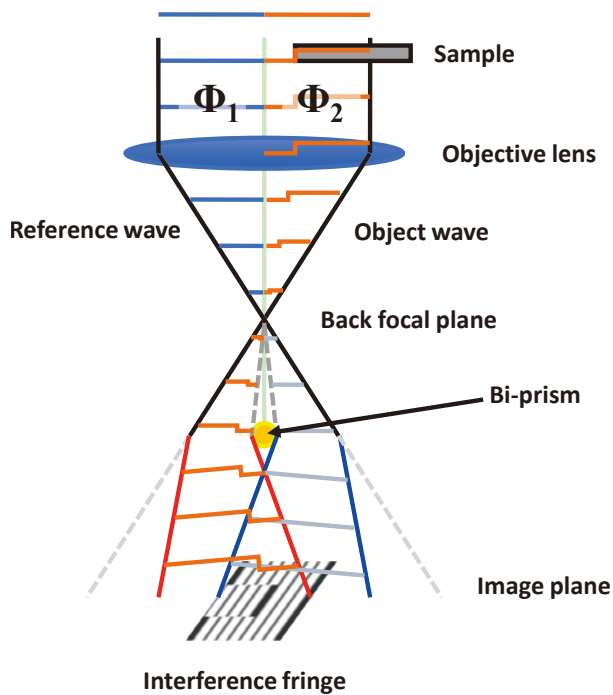
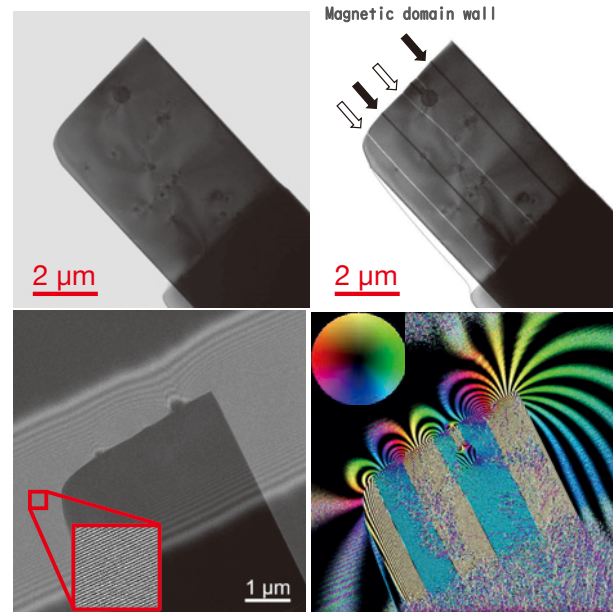


Fig. 8 Thin film for TEM observation prepared by FIB from a commercial NdFeB magnet.



The upper left image is a TEM image and the upper right image is a focus-shift image by the Lorentz method. The lower left is a hologram. The lower right image is an interference microscope image reproduced from the hologram.

4700F) and observing the magnetic domain structure. The upper left panel shows a TEM image at low magnification. Although some defects can be seen in the thinned portion of the sample, the contrast is uniform. On the other hand, when the focus is shifted, the magnetic walls existing in the sample appear in white or black straight-line contrast as shown by the arrow in the upper right figure, indicating that the magnetic domain structure is strip-shaped. The lower left figure shows a hologram of interference fringes formed by a biprism at the edge of the sample. The magnified image of the red square region in the vacuum region is shown in the figure, and the interference fringes are clearly observed. The interference microscope image obtained by computer analysis from this hologram is shown at the lower right. Within each magnetic domain structure, the direction of the contour lines indicates the direction of magnetization, and the spacing indicates the strength of magnetization. The color wheel in the figure indicates the orientation of the magnetization. Contour lines parallel to the long axis direction are observed inside the strip-shaped magnetic domain, indicating that the direction of magnetization differs by 180° between neighboring magnetic domains and that the magnetic wall is a 180° magnetic wall. On the other hand, magnetic field lines leak into the vacuum region from the edge of the sample.

Conclusion

When considering the introduction of a large measuring instrument, regardless of whether it is a transmission electron microscope or not, it is likely that the configuration and options of the instrument are considered based on the expectation of long-term operation over a period of 10 years or more. However, it is rare that the subject of observation remains the same for a long period of time, and the information that must be obtained using measurement equipment often changes significantly from the

initial installation. The applications reported here are examples using in-situ observation holders that can reproduce heated, gaseous, or liquid environments, crystal orientation analysis using precession electron diffraction, and magnetic field analysis using holography with electron beam biprisms, which were obtained using so-called "retrofit" equipment. These results were obtained using so-called "retrofitted" equipment. In some cases, it is possible to install these instruments in existing transmission electron microscopes, making it possible to obtain scientific findings such as those described here at a low installation cost. In addition, it is also possible to meet the request of "What can we do in addition to the existing equipment?"

Acknowledgments

Dr. Yaofeng Guo of Protochips and Dr. Ichiro Ohnishi of JEOL's EM Business Unit assisted with in-situ observation. Mr. Seiichi Suzuki of TSL Solutions, Inc. assisted in the crystal orientation analysis by precession electron diffraction, and Mr. Masateru Shibata of the EP Business Unit, JEOL Ltd. assisted in the FIB sample preparation.

References

- [1] Protochips: <https://www.protochips.com/>
- [2] DENS solutions: <https://denssolutions.com/>
- [3] Hummingbird Scientific: <https://hummingbirdscientific.com/>
- [4] Mel-Build: <https://www.melbuild.com/>
- [5] S. Singh, et al, *Scientific Reports*, **7** (2017).
- [6] S. Zhang, et al., *Nano letters*, **16**, 7, 4528-4534 (2016).
- [7] S. Suzuki, *Materia*, **61**, 27-34 (2022).
- [8] Z. Wang, T. Hirayama, *Applied Physics Letters*, **80**, 246-248 (2002).
- [9] K. Fukunaga and A. Sugawara, *Journal of Applied Physics*, **103**, 053909 (2008).

TEM Sample Preparation Using JIB-PS500i and Multi-Purpose FIB-SEM

Misumi Kadoi, Tatsuhiro Kuramoto, Masateru Shibata, Osamu Suzuki, and Yuichiro Ohori
EP Business Unit, JEOL Ltd.

FIB-SEM is an essential tool for TEM sample preparation used in a wide range of applications. Since objects of observation and analysis in TEM are increasingly miniaturized, TEM samples are required to be extremely thin to enable high accuracy object identification while being more resistant to damage during FIB processing. Linkage with TEM is also critical as the sample transfer between the systems ought to involve as few steps as possible.

The JIB-PS500i (**Fig. 1**) is the latest model of our FIB-SEM series for high quality TEM sample preparation. Featuring high resolution/high quality SEM imaging that facilitates determination of the end point of FIB processing, the system incorporates a double tilt cartridge for easy sample loading onto TEM, a specimen chamber accommodating large samples, and a high tilt stage that provides greater flexibility for the direction of FIB processing. These features are designed for a simple, stress-free process sequence for high quality TEM sample preparation.

Introduction

Today, high density 3D Fin Field-Effect Transistors (FinFET), which are used for numerous semiconductor devices, feature a fin width of 10 nm or less. In process control and failure analysis for such devices, it is essential to measure pattern sizes and analyze defects by high spatial resolution TEM (Transmission Electron Microscopy). As a result, FIB-SEM systems as a sample preparation device are in ever increasing demand. Samples subjected to TEM analysis are required to:

- Clearly capture intended areas;
- Be thin and without any structures other than the intended areas;
- Be contamination free

To produce such samples, it is important for the FIB-SEM to combine SEM functions to accurately identify the desired position with superior FIB performance at low accelerating voltages to minimize sample damage. Also, as TEM analysis is used widely, throughput of the TEM sample preparation process is increasingly important. This requires a stage large enough to accommodate multiple samples at a time, featuring high tilt angles for greater flexibility during processing.

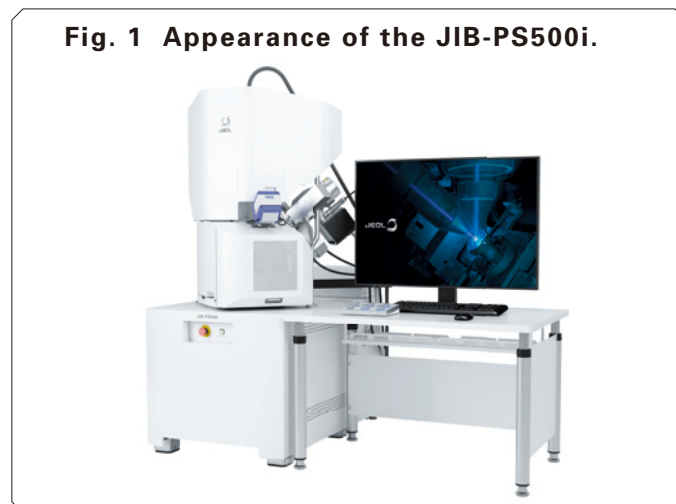
Basic Performance as FIB-SEM

For any FIB-SEM, basic capabilities and safety features of its SEM, FIB, and specimen stage are essential. Features of the JIB-PS500i will be described in detail below.

1. Super Conical Objective Lens

High resolution and superior image quality provided by the SEM are essential for determination of accurate milling positions. The JIB-PS500i incorporates a new super conical objective lens with shorter focal lengths, enhancing resolution significantly over the existing model. A new detector has also been developed, optimized for this objective lens. **Figure 2** shows a secondary electron image

Fig. 1 Appearance of the JIB-PS500i.



(detector: SED) and a backscattered electron image (detector: UED) of a TEM sample being processed. The images were acquired at an accelerating voltage of 2 kV. The sample was a commercial semiconductor device. The secondary electron image shows a well-contrasted Fin structure, making it easier to determine the milling position. The backscattered electron image visualizes a compositional contrast, showing the shapes of metal connects and barrier metal formation. For a device with ultra fine lines, a minute process step can often lead to disappearance of the target position. To avoid the disappearance, the operator is required to repeat a cycle of rapid FIB processing followed by SEM imaging in a meticulous manner. Therefore, clear imaging of FIB-processed sample surfaces is extremely important. Given the above, image quality at low accelerating voltages, specifically 2 kV or below, plays an important role, requiring a detection system capable of simultaneous acquisition of secondary electrons for surface information and backscattered electrons for compositional information.

2. Power Stabilization Lens

TEM sample preparation often requires STEM imaging at a high accelerating voltage in addition to secondary and backscattered electron imaging at a low accelerating voltage.

STEM imaging is used to determine whether or not the processed sample is thin enough for TEM analysis. The transition from TEM sample preparation to STEM imaging requires a significant change of the accelerating voltage from 2 kV to 30 kV. During the process, the amount of heat generated by the objective lens changes substantially, resulting in image drift that often compromises imaging stability for quite a while.

The JIB-PS500i incorporates a new objective lens, the Power Stabilization Lens, designed to minimize the effect of thermal drift resulting from the changes in objective lens excitation. The new lens controls heat dissipation at a constant level regardless of the lens conditions.

3. Enhanced FIB Performance at Low Accelerating Voltage

FIB processed samples are often marked with damage by the Ga ion beam on the processed surface, unfit for TEM imaging. It is known that the thickness of the damaged layer increases monotonously with the accelerating voltage of the ion beam [1]. Thus, finish processing at low accelerating voltages is needed to prepare high quality TEM samples.

The conical objective lens of the SEM in the JIB-PS500i provides shorter focal lengths for the FIB, enhancing resolution in the low accelerating voltage range. The lowest accelerating voltage is 0.5 kV, which is used for processing at the final process step.

Figure 3 shows TEM images of a blue LED featuring a multiple quantum well structure of GaN/InGaN. Figure 3(a) is a TEM image of the sample subjected to finish processing with the Ga ion beam at 5 kV, and Figure 3(b) is a TEM image of the sample subjected to finish processing with the Ga ion beam at 1 kV. A JEM-ARM200F was used for observation

at an accelerating voltage of 200 kV. The TEM image of the sample finished at 5 kV shows a dark spotted contrast, likely to represent FIB damage, over the entire area of view. Meanwhile, the TEM image of the sample finished at 1 kV is free from the dark spotted contrast seen in the sample finished at 5 kV. It also shows clear boundaries of multiple layers in the multiple quantum well structure. Furthermore, a lattice image was more clearly observed. This demonstrates that the processing at 1 kV produced a sample with minimum damage.

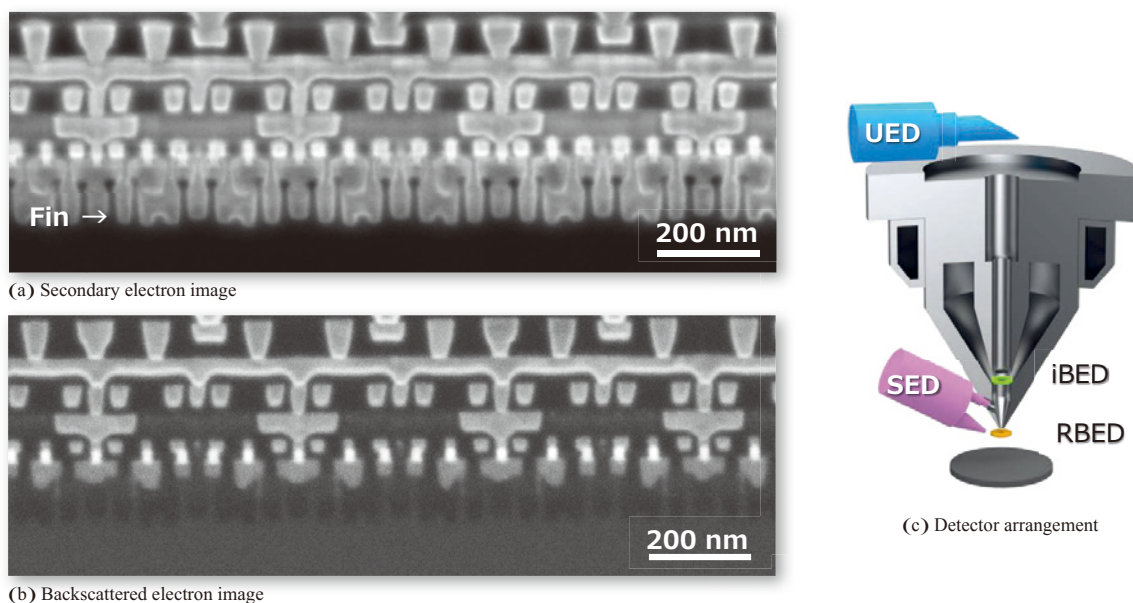
Figure 4 shows high resolution STEM images of GaN [211]. Final FIB processing conditions were 1 kV and 20 pA. A JEM-ARM300F was used for observation at an accelerating voltage of 300 kV. The STEM-HAADF image captured atomic columns of Ga (Fig. 4(b)), and the STEM-ABF image captured atomic columns of Ga and N (Fig. 4(c)). Also, a 49 pm spot was identified in the FFT pattern (Fig. 4(d)).

4. Large Specimen Chamber and High Tilt Stage

The JIB-PS500i incorporates a specimen chamber and stage capable of imaging and processing a sample of 130 mm in size. The maximum sample height supported is 80 mm. A large door on the left front is opened to enable specimen exchange from a large space. In many FIB-SEM systems, the stage is retracted from the chamber for specimen exchange. In the JIB-PS500i, the stage is stationary during specimen exchange, free from positional shifts of the stage when retracted. This allows the stage to maintain its pre-set eucentric position for a long period of time. The stage can also incorporate an optional specimen pre-evacuation chamber.

The new stage supports a wide range of specimen tilt angle from -40° to 93° for greater flexibility during FIB processing. This eliminates trimming and attitude control during TEM sample preparation as well as sample loading and replacement for post-process STEM imaging, resulting in a seamless, stress-free process sequence.

Fig. 2 SE and BSE images of a FinFET cross section and Detector Arrangement.



(a) Secondary electron image (detector: SED) (b) Backscattered electron image (detector: UED) (c) Detector arrangement

The secondary electron image shows a well-contrasted Fin structure, making it easier to determine the milling position.

The backscattered electron image visualizes the compositional contrast, showing the shapes of metal connects and barrier metal formation.

Fig. 3 TEM images of GaN/InGaN.

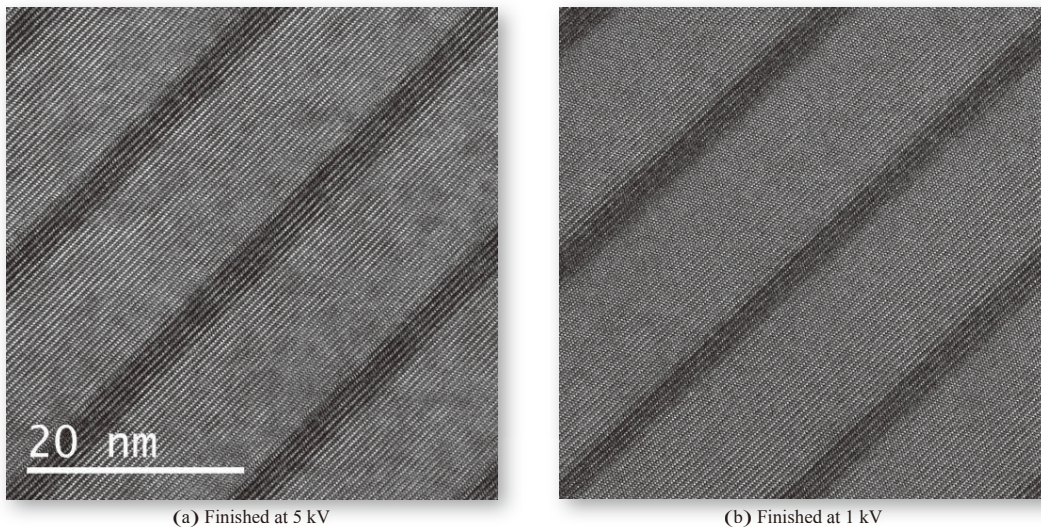
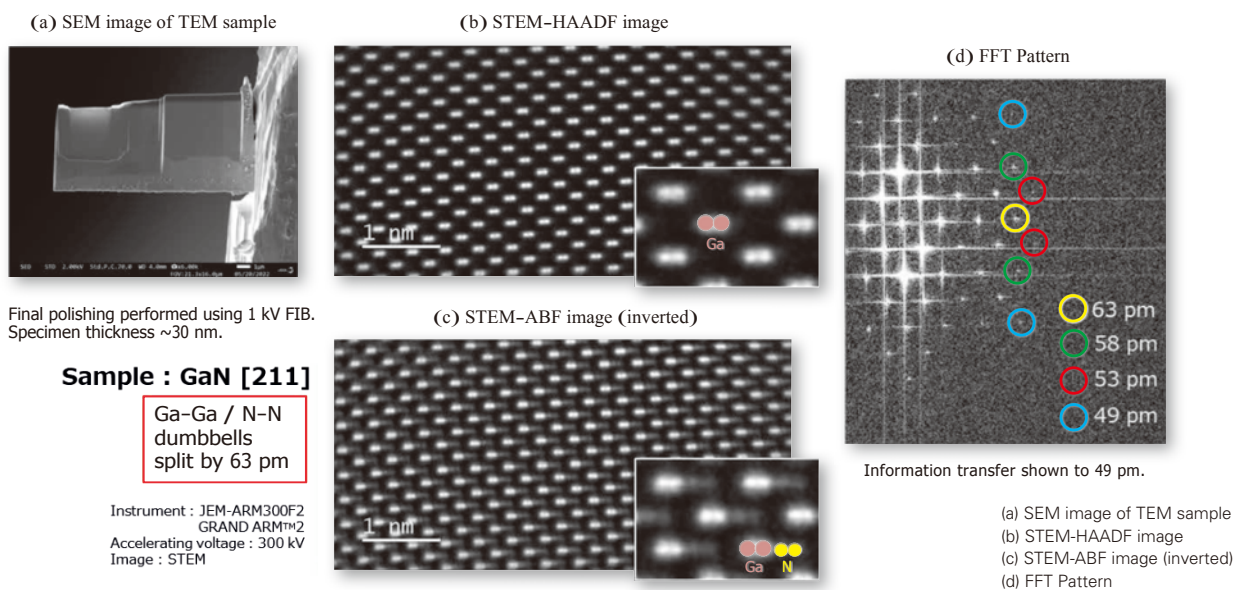


Fig. 4 TEM sample and STEM images of GaN [211].



5. Anti Collision Safety System: AVERT Engine

In the FIB-SEM, a sample is tilted at high angle during processing and observation. This means that multiple devices such as a gas injection nozzle and various detectors are used around the sample, often resulting in concerns about possible collision between the sample and objective lens. While the safety features of the FIB-SEM have been enhanced over time, traditional 2D identification of the specimen holder shape often fails to ensure safety, and as a result, excess limits on movement are being programmed for safety.

A new safety system called AVERT Engine features 3D modeling of all components inside the specimen chamber. It is designed to determine possible collision three dimensionally if any of the components is moved, ensuring safety in operation. **Figure 5** shows a 3D modeling image of a double tilt cartridge holder tilted at 52° for FIB processing while a gas injection nozzle is loaded. Avert Engine enables safe operation of the FIB-SEM when an intricately designed holder such as this is used.

Solutions for TEM Sample Preparation

The JIB-PS500i is provided with 3 powerful solutions to facilitate TEM sample preparation: 1) TEM-LINKAGE for easy sample loading to the TEM; 2) CHECK AND GO for close monitoring of the sample; and 3) STEMLING2, an auto TEM sample preparation system. These solutions will be described in detail below.

1. TEM-LINKAGE

In the TEM sample preparation process using FIB-SEM, sample handling is an operational step that is most prone to failure. This step was thoroughly reviewed, resulting in a high accuracy, high throughput workflow from sample preparation to TEM imaging. Conventionally, a TEM sample prepared by FIB-SEM needs to be removed from a FIB-SEM holder and mounted onto a TEM holder. The sample, mounted on a FIB grid 3 mm in diameter and 20 to 50 μm in thickness, is transferred to the TEM holder

using tweezers. This step is prone to failure and sample damage, as many users have often faced this problem. It is extremely frustrating to lose the TEM sample, which was subjected to multiple process steps from creating a sample block out of a bulk sample to loading to the FIB grid for thin film formation.

Figure 6(a) shows a new double tilt cartridge. A new TEM grid is loaded onto this cartridge using tweezers, which is the only manual handling of the TEM grid. At this point, because TEM sample preparation has not begun, handling errors of the TEM grid, including a fall or misalignment, are permissible. Figure 6(b) shows a FIB holder and Fig. 6(c) a TEM holder, respectively. Using a dedicated tool (jig), the cartridge loaded with the TEM grid is mounted to the FIB holder and loaded into the FIB-SEM. The FIB-SEM holder accommodates a pin stub, on which a bulk sample is mounted together with a FIB grid. On the bulk sample, a desired sample block is prepared and transferred to the TEM grid using in-situ pickup for TEM sample preparation.

After a TEM sample is prepared, the FIB holder is unloaded from the FIB-SEM specimen chamber, and the cartridge alone is removed. The sample is mounted to the TEM holder using a jig and loaded into the TEM.

This sequence has minimized the step for manual transfer of the TEM grid with tweezers, significantly reducing risks of sample damage during sample loading. It should be noted that both the double tilt cartridge and TEM holder are supported by most JEOL TEM models.

Figure 7 shows a TEM sample created by the TEM-LINKAGE process. The sample was FinFETs of a semiconductor

device, and the target area of observation was a cross section of fins intersecting with gates. A JEM-ARM200F was used for observation at an accelerating voltage of 200 kV.

The resulting TEM image demonstrates that the TEM sample satisfies its intended specifications. TEM-LINKAGE enables safe and efficient sample transfer from the FIB-SEM to TEM by eliminating manual handling of a TEM grid from the entire process of creating a sample block out of a bulk sample, loading of the sample onto the TEM grid by in-situ pickup, thin film formation, and sample loading to the TEM.

2. CHECK AND GO

A TEM sample prepared for a target area, such as defects, needs to be constantly examined to determine if the target area has been processed, is indeed present, and satisfies a specified film thickness. Thus, it is crucial to accomplish SEM imaging at each step of FIB processing. If observation of the rear surface is needed, the stage is rotated by 180° for SEM imaging, and the sample is continuously processed by the FIB to the target area. To determine if a desired thin film sample has been created, STEM imaging is also effective in addition to SEM imaging.

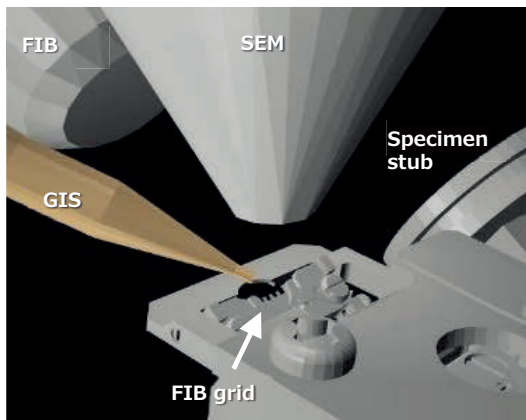
Figure 8 shows SEM and STEM images of a sample after it was subjected to thin film formation by FIB processing and the geometry around the holder at the time. Figure 8(a) shows the geometry at a FIB processing position of 52°, and Fig. 8(b) is a secondary electron image of the sample prepared under these conditions. Figure 8(c) shows the geometry, in which the stage was tilted by 90° for STEM imaging after the FIB processing in Fig. 8(a) was completed, and the STEM detector was loaded. Figure 8(d) shows STEM BF and DF images taken under these conditions. These data demonstrate a seamless, stress-free transfer from FIB processing to STEM imaging.

For successful TEM sample preparation, it is important to examine the sample on the spot at each step of the preparation process. The JIB-PS500i, with its flexible stage, STEM specific holder, and new STEM detector, enables examination of the sample on the spot in the entire process from TEM sample preparation to STEM imaging without loading and unloading of the sample.

3. STEMLING2 - Auto TEM Sample Preparation System

STEMPLING, an auto TEM sample preparation system, has been appreciated by many users since it was introduced in 2019 as a tool to provide a simpler, user-independent TEM sample preparation process [2]. A new upgraded version, STEMLING2, is an optional accessory for the JIB-PS500i. STEMLING2 is provided with finish processing at low accelerating voltages in addition to the existing capabilities. The new feature is essential for creating thinner samples with minimal beam damage.

Fig. 5 Side view.



Sample being subjected to FIB processing (deposition) on a double tilt cartridge holder; GUI provides 3D modeling of the geometry around the sample for monitoring of the operation.

Fig. 6 TEM-LINKAGE.

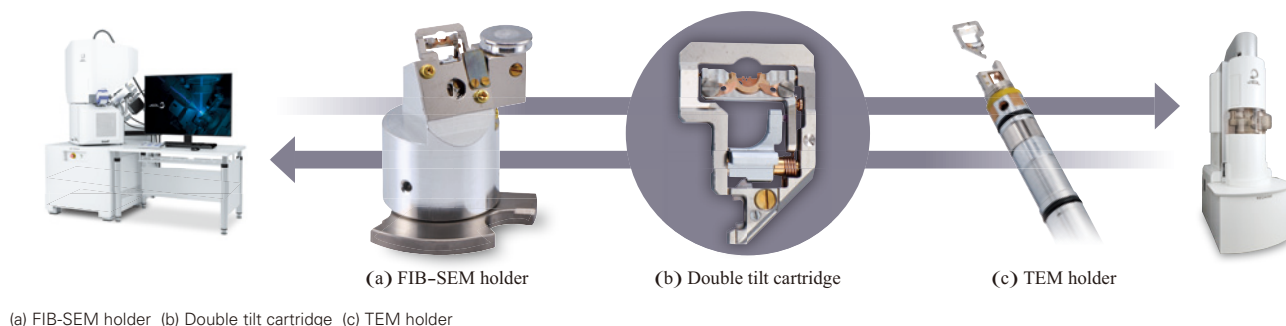
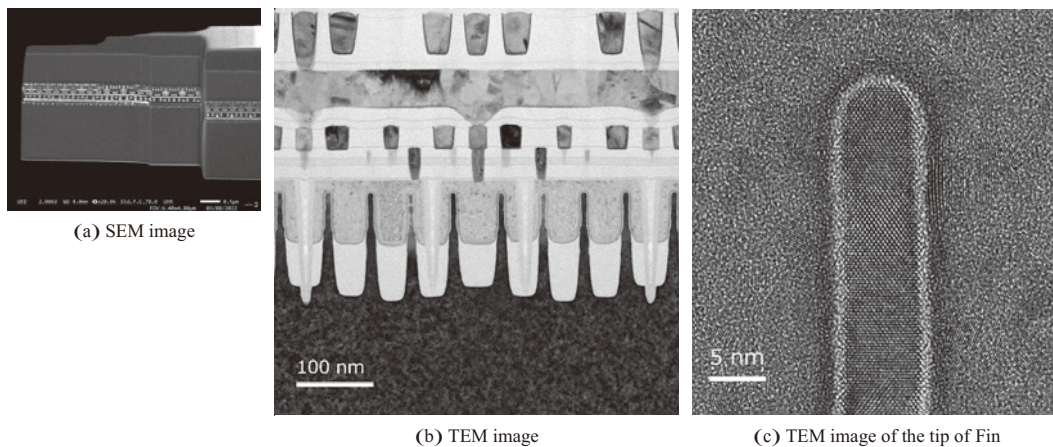
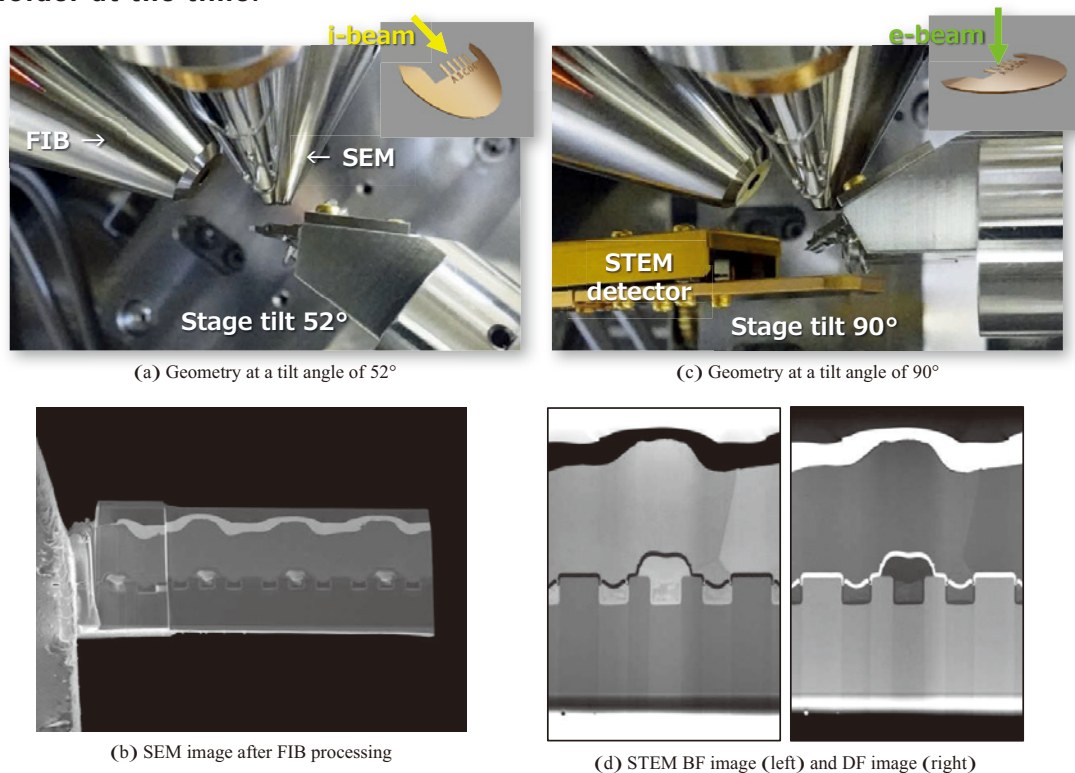


Fig. 7 TEM sample created by TEM-LINKAGE.



The TEM sample captured the desired Fin structure, demonstrating that TEM-LINKAGE enables stress-free double tilt control that is essential for TEM imaging.

Fig. 8 SEM and STEM images after thin film formation and the geometry around the holder at the time.



Summary

This article introduced the major features of the JIB-PS500i and some of the TEM samples created by the system. The JIB-PS500i, in addition to its enhanced performance as FIB-SEM, incorporates a number of powerful features, including a large, high tilt stage for greater flexibility, easy sample transfer to any JEOL TEM, and auto sample preparation with FIB finishing at low accelerating voltages, contributing significantly to minimizing users' frustration and stress during the sample preparation process.

Finally, it should be noted that the FIB-SEM is only a part of multi-step sample preparation and needs to be connected to

various devices such as mechanical polisher and CP (CROSS SECTION POLISHER™). JEOL's CP holder can be loaded in the JIB-PS500i without modification for atmosphere isolation sample transfer. This allows for a seamless sequence of operation from CP sample preparation to FIB-SEM processing to TEM analysis without unloading the sample.

References

- [1] Orloff, Jon, ed., Handbook of Charged Particle Optics, CRC press, 2017.
- [2] Yoshitaka Ishihara and Tomohiro Mihira: Automated TEM Lamella Preparation with JIB-4700F, *JEOL News*, Vol. 54, No. 1, 27-31 (2022).

msFineAnalysis AI Novel Qualitative Analysis Software for JMS-T2000GC with AI Structural Analysis

Ayumi Kubo MS Business Unit, JEOL Ltd.

JEOL developed msFineAnalysis as qualitative analysis software for our gas chromatograph time of flight mass spectrometer (GC-TOFMS). We implemented deconvolution detection, variance component analysis, and other features in the software through updates. We have recently developed a new version of the series called msFineAnalysis AI. msFineAnalysis AI is equipped with a structural analysis method using artificial intelligence (AI), called “AI structural analysis.” AI structural analysis enables the identification of molecular formulas as well as structural formulas of compounds that are not registered in the NIST 20 library (unknown compounds). The workflow of AI structural analysis is as stated below.

First, msFineAnalysis’s integrated analysis function identifies the molecular formula of an unknown compound. Next, based on the identified molecular formula, structural formula candidates are extracted from PubChem, the database containing over 100 million compounds. The AI predicts electron ionization (EI) mass spectra from the extracted structural formula candidates. Then, the structural formula candidates are ranked by comparing the predicted mass spectra with the measured mass spectrum. Finally, a candidate that ranks first is adopted as the analysis result.

Using the NIST 20 library, we trained the AI to predict mass spectra from structural formulas and evaluated its accuracy. From the results of accuracy evaluation, we confirmed that AI structural analysis is useful in the structural analysis of unknown compounds. In this report, we will introduce features of msFineAnalysis AI and provide our evaluation results.

Introduction

The electron ionization (EI) method is widely used as an ionization method for gas chromatograph mass spectrometry (GC-MS). Fragment ions are mainly observed in a mass spectrum obtained by the EI method (herein, an EI mass spectrum). Fragment ions reflect the structure of a compound and has a pattern unique to it. For this reason, in qualitative analysis of GC-MS, an EI mass spectrum is compared with libraries of EI mass spectra of reference compounds. The NIST library, the most widely used library of structural formulas and mass spectra, has about 300,000 registered compounds.

Meanwhile, PubChem, a major compound database, contains over 100 million substances as of 2023. However, EI mass spectra are not registered in PubChem. This means that most compounds in PubChem do not have EI mass spectral information, except for some also registered in the NIST library. When library searches are performed for EI mass spectra of such compounds, qualitative analysis results may not be obtained, or wrong compounds may possibly be identified. For these compounds that are not registered in the NIST 20 library, it is useful to combine [2] the field ionization (FI) and other soft

ionization methods with a mass spectrometer [1] that obtains accurate mass. The specific procedure is as follows:

1. The EI and soft ionization mass spectra are compared, and a molecular ion peak is determined.
2. Based on the accurate mass of the determined peak, molecular formula candidates are obtained.
3. For obtained molecular formula candidates, isotope pattern analysis and accurate mass analysis of fragment ions in the EI mass spectrum are performed. Based on the results of these two analyses, the molecular formula is determined.

The above method is implemented in msFineAnalysis, which enables the automated identification of the molecular formula of an unknown compound. We have newly developed a structural analysis method using artificial intelligence (AI), called “AI structural analysis,” with an aim to obtain not only molecular formulas but also structural formulas of unknown compounds. The new version of msFineAnalysis equipped with AI structural analysis, msFineAnalysis AI, was introduced to the market in January 2023. In this article, we will provide an overview of AI structural analysis and report the results of its accuracy evaluation. In addition, we will show the results of applying this function to compounds that are not registered in the NIST 20 library.

AI structural analysis

AI structural analysis uses two types of AI: main AI and support AI. **Figure 1** shows the procedures of integrated analysis and AI structural analysis for compounds that are not registered in the library. msFineAnalysis AI automatically performs the detection of a compound and steps 1 to 4 below. Details about two types of AI are described in the next section.

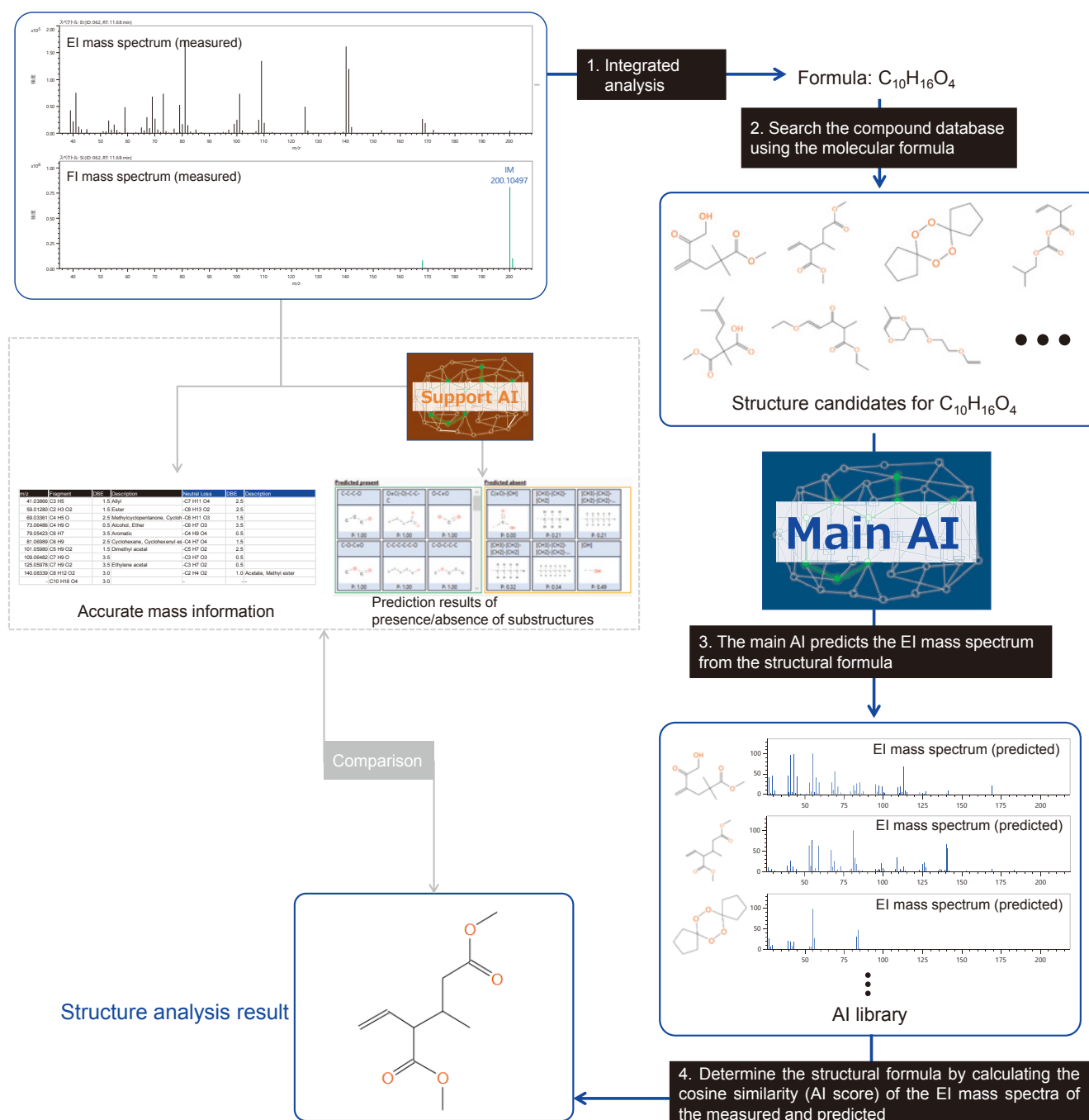
1. msFineAnalysis AI performs integrated analysis using the EI mass spectrum and the mass spectrum obtained by the FI method, a soft ionization method, to identify a molecular formula.
2. Based on the identified molecular formula, the software

extracts structural formula candidates from PubChem database that contains over 100 million compounds. Ten thousand or less candidates are extracted.

3. The main AI predicts EI mass spectra for the extracted structural formula candidates.
4. By comparing the predicted EI mass spectra with the actual measured EI mass spectrum, the software ranks the structural formula candidates using AI scores (cosine similarities). Finally, the candidate that ranks first is adopted as the analysis result.

*The software displays the structural analysis results obtained through steps 1 to 4, as well as accurate mass information and

Fig. 1 Overview of AI structural analysis.



the results of partial structure prediction by the support AI. Analysts can use this information and knowledge to interpret the structural analysis results. However, this process is performed independently, and the structural analysis results can be automatically obtained without it.

Features of AI structural analysis include the EI mass spectrum prediction by main AI, as well as narrowing down candidates based on a molecular formula identified with integrated analysis. Before the measured mass spectrum is compared with AI-predicted EI mass spectra, the molecular formula identified by integrated analysis helps narrow down structural formula candidates. This allows the scope of structural formula candidates to be narrowed from 100 million to 10,000 or less, making it possible to perform an efficient and highly accurate structural analysis.

If a molecular formula is not identified in advance, the measured EI mass spectrum must be compared against the entire compound database, or must be narrowed down using compound species. In comparison against the entire database, the measured spectrum must be compared with 100 million EI mass spectra, resulting in a time-consuming and less accurate analysis. The reason for a lower accuracy is that some compounds are difficult to distinguish from others based on EI mass spectral information alone. The four compounds shown in **Fig. 2** have different structural and molecular formulas, but exhibit highly similar EI mass spectra. Therefore, only comparing their EI mass spectra is not sufficient for identification and may lead to wrong qualitative analysis results. Meanwhile, to identify compound species, information about samples and analysts' experience and knowledge are required. If there is not enough sample information, identifying compound species will be difficult. Additionally, an incorrect selection of species can lead to wrong structural analysis results. Consequently, analysis might be dependent on individual skills of analysts, resulting in a low reproducibility. On the other hand, AI structural analysis

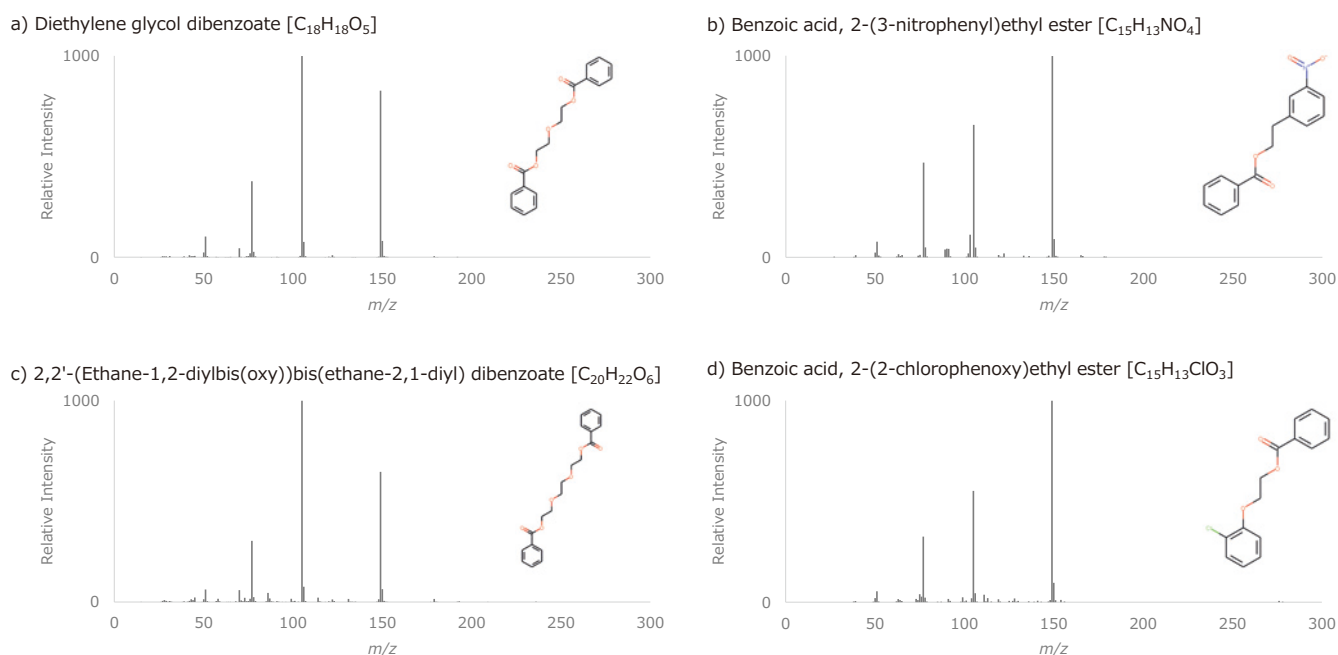
generates correct analysis results for the four compounds shown in Fig. 2, because it narrows down structural formula candidates beforehand using the molecular formula identified by integrated analysis as mentioned earlier.

msFineAnalysis AI is not equipped with the main AI. Instead, it is equipped with the "AI library," which contains structural formulas extracted from PubChem and mass spectra predicted from the structural formulas by the main AI. The AI library helps eliminate the need for mass spectrum prediction during analysis, improving the analysis throughput. After an analyst selects measurement data and presses the button to start the analysis, msFineAnalysis AI automatically performs all the processing to complete the structural analysis. The analyst can obtain structural analysis results for 100 compounds within 10 minutes. The AI library also eliminates the need for connecting to the compound database via the Internet during analysis, enabling a stable and stand-alone analysis.

Figure 3 shows the graphical user interface (GUI) of AI structural analysis. Structural formulas are listed in descending order of AI score at the lower part of the window. On the top left corner of the list is the structural analysis result. As the information about the structural formula, its IUPAC name and PubChem CID (identification number in PubChem database) are also displayed. The number of structural formula candidates for the molecular formula and the histogram created using AI score are displayed on the upper right of the window. These various kinds of information help the analyst see the whole picture of the structural analysis results.

In addition, if there is knowledge about the target compound, the analyst can filter structural formulas using partial structures such as benzene ring and methyl ester. When the analyst presses the button on the right edge of the window, it displays the mass spectrum and information for accurate mass as well as the prediction results of partial structures performed by the support AI. The analyst can confirm and interpret the structural analysis results.

Fig. 2 EI mass spectra of four compounds registered in the NIST 20 library.



Two types of AI

This section describes two types of AI used in AI structural analysis.

The main AI employs Graph Convolutional Networks (GCN) [3], a type of deep learning, as its model (Fig. 4, top). GCN operates as follows: First, the machine searches structural formulas for partial structures that produce signals characteristic of a mass spectrum, and generates a lot of partial structures. Then, the machine predicts a mass spectrum based on the generated partial structural information (Fig. 4, bottom).

The specific processing is as follows: First, the structural formula is converted to graph data before being input into GCN (Fig. 5). In graph data, atoms and bonds in the structural formula are treated as nodes and edges, respectively. In addition, nodes hold information on the elemental species of atoms, and edges hold information on the type of bonds, as their feature vector. For example, a node for the carbon atom has the feature vector (1, 0, 0, ...), a node for the oxygen atom has the feature vector (0, 1, 0, ...), and a node for the nitrogen atom has the feature vector (0, 0, 1, ...).

Next, the machine performs convolutions on the structural formula that was converted to graph data as shown in the top left of Fig. 4. Through convolutions, each node sifts through and obtains information on neighboring nodes and edges. The machine learns to recognize the connection of atoms as a block by repeating convolutions.

Then, the machine performs pooling of each atom as shown in the top right of Fig. 4. This enables the machine to grasp the characteristics of the structural formula and predict a mass spectrum.

The support AI employs the traditional machine learning (regression) instead of deep learning. The machine predicts the presence or absence of 48 partial structures from ions and neutral loss based on the accurate-mass mass spectra (Fig. 6). The support AI is simple and uses dozens of coefficients. Therefore, the machine can provide prediction results and their characteristic peaks at the same time.

Accuracy evaluation of AI structural analysis

— Accuracy evaluation of EI mass spectrum prediction —

AI structural analysis uses mass spectra that are predicted from the structural formulas by the main AI. The main AI was trained using the structural formulas and mass spectra of 270,000 compounds, which account for 90% of the NIST 20 library data. During training, the weight of the main AI was optimized so that patterns of mass spectra predicted from the structural formulas match those of mass spectra in the NIST 20 library. Out of the remaining 30,000 compounds, 10,000 were allocated for validation to prevent overfitting, and 20,000 were used to evaluate the accuracy of EI mass spectrum prediction.

We evaluated the accuracy of the main AI's EI mass spectrum

Fig. 3 GUI of AI structural analysis.

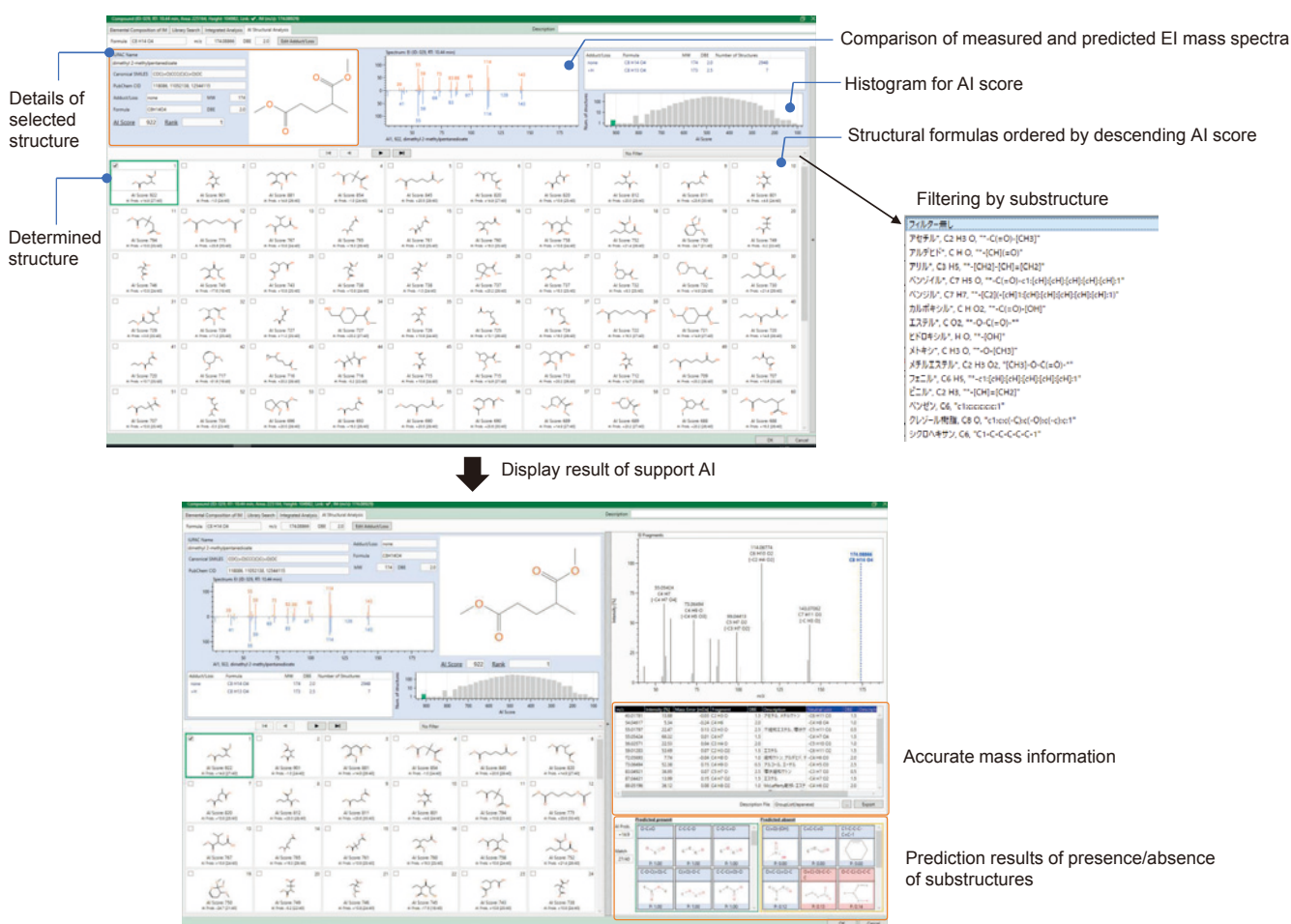


Fig. 4 Graph Convolutional Networks used in the main AI.

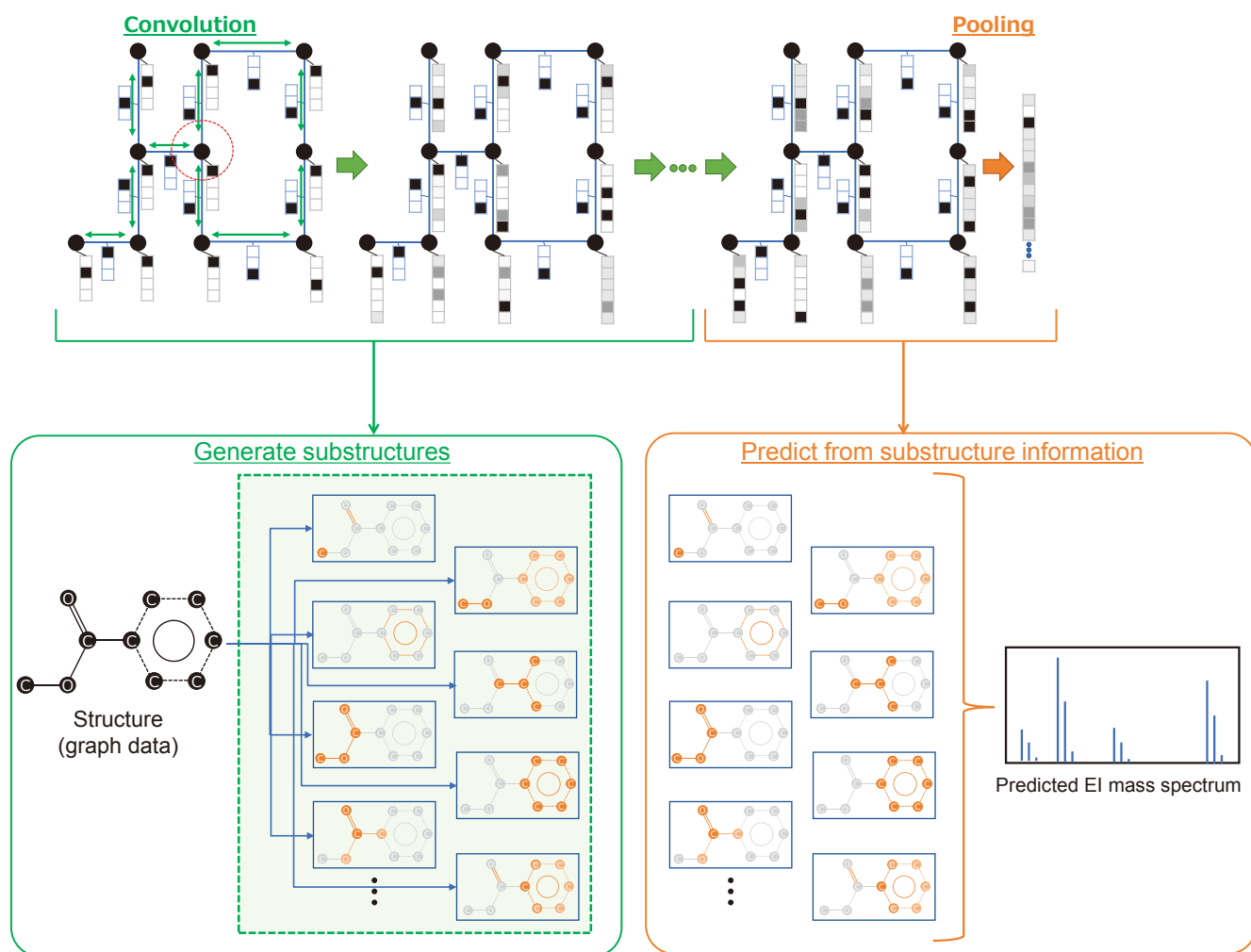
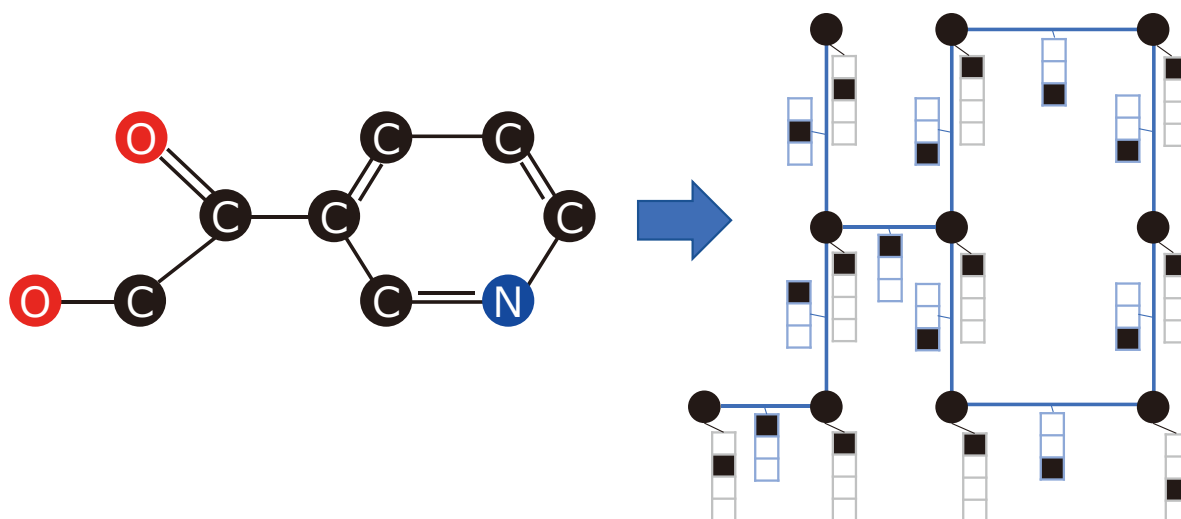


Fig. 5 Conversion of a structural formula to graph data.



prediction using 20,000 compounds that were not used in training. In the evaluation, the trained main AI predicted EI mass spectra from the structural formulas of the target compounds. We used the cosine similarity between the predicted EI mass spectrum and an EI mass spectrum registered in the NIST 20 library as the index of accuracy evaluation. A cosine similarity of 1 means the two EI mass spectra match perfectly. As the cosine similarity is closer to 0, they match less.

Figure 7 shows a histogram of cosine similarities calculated using 20,000 compounds. The histogram shows that more than 90% of the compounds had a cosine similarity of over 0.4. In addition, the 0.7-0.8 segment had the highest number of the compounds. The average cosine similarity was 0.72. We confirmed that the main AI can reproduce mass spectra with a high accuracy by predicting them from the structural formulas.

Figure 8 shows as examples the comparison between the measured and predicted EI mass spectra for each of the compounds with above-average, near-average, and below-average cosine similarities. For Benzamide, 3-methyl-N-decyl-, which had an above-average cosine similarity, the EI mass

spectrum was reproduced almost completely including mass peaks with low intensity. The reason is thought to be that this compound consists of only benzene rings, alkane chains, and amide groups, many of which are registered in the NIST 20 library. For N-Acetyl-3-(3-formyl-4-methoxyphenyl)-d-alanine methyl ester, which had a near-average cosine similarity, mass peaks with relatively high intensity were reproduced, and the overall patterns were similar. This compound has a somewhat complex structure, with multiple side chains attached to a benzene ring, compared with the structural formula of Benzamide, 3-methyl-N-decyl-. This is thought to be why a complete mass spectrum was not reproduced. For Cyclododecane, 1,5,9-tris(acetoxy)-, which had a below-average cosine similarity, the overall pattern was not well reproduced. A possible reason is that this compound includes a large 12-membered ring, and the NIST 20 library contains a small number of compounds that have this ring. This may have prevented the machine to be trained enough. However, some mass peaks, including the most intense one at m/z 43, were reproduced.

Fig. 6 Overview of the support AI.

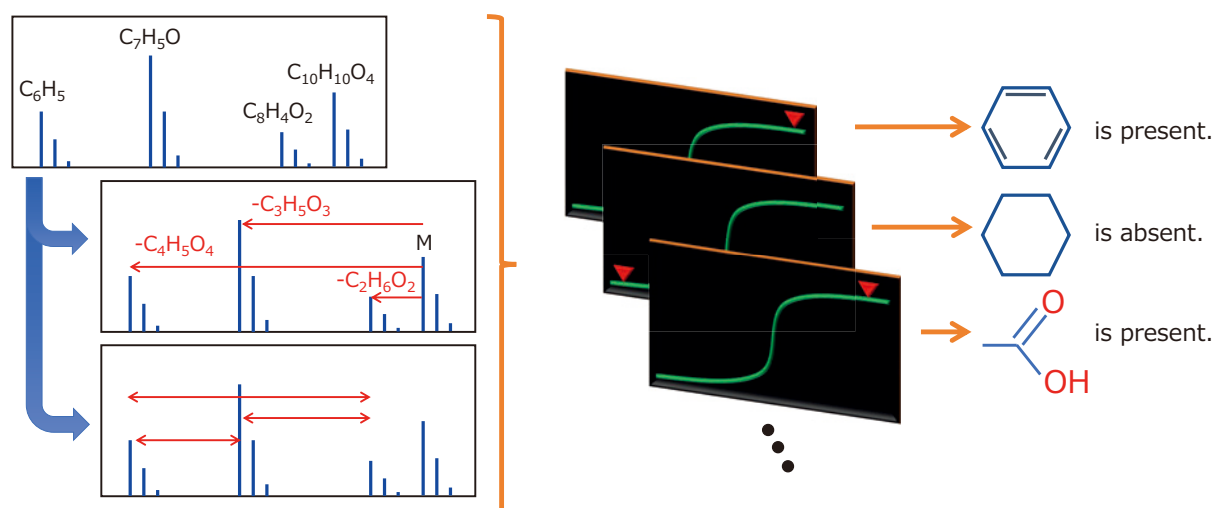


Fig. 7 Histogram of cosine similarities calculated using 20,000 compounds that were not used in training.

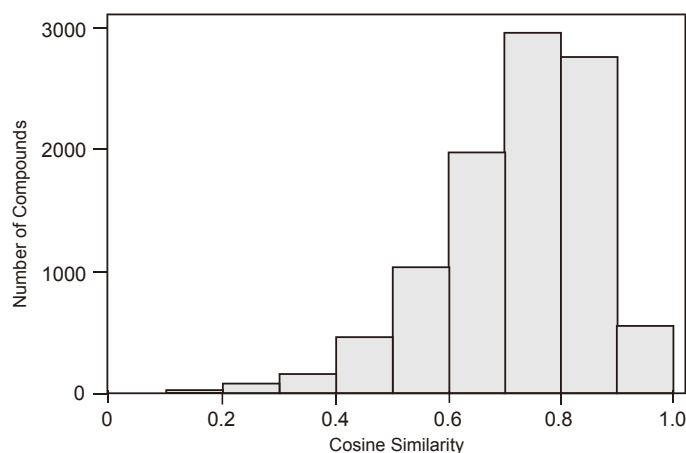
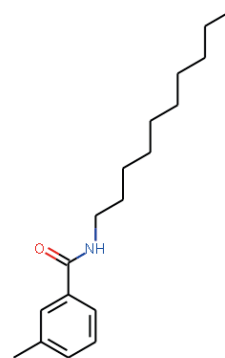
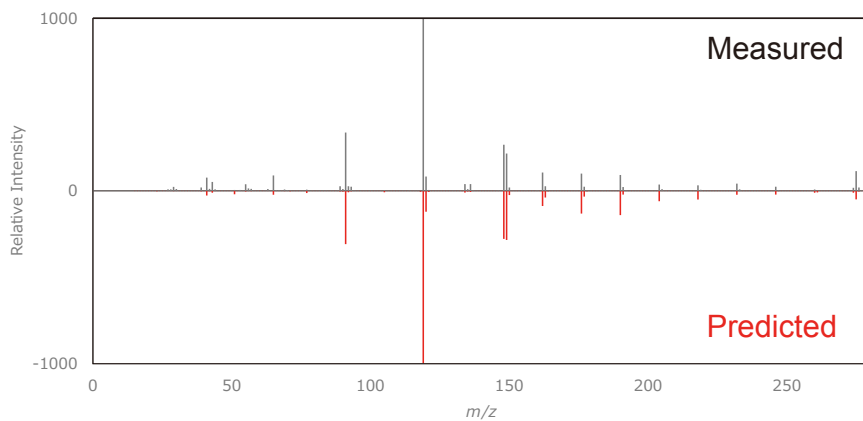
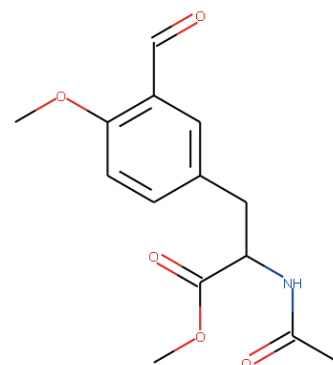
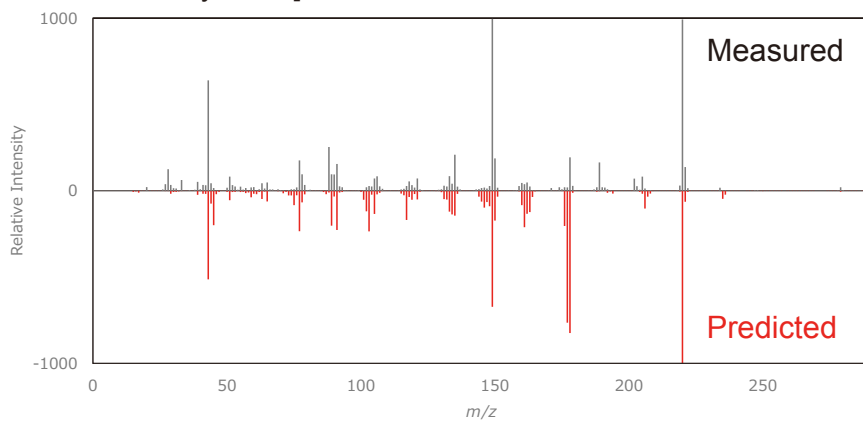


Fig. 8 Comparison between the measured and predicted EI mass spectra.

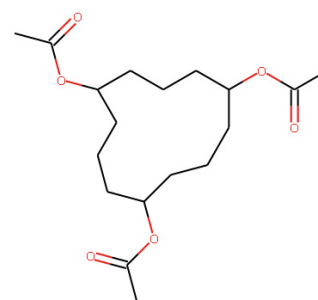
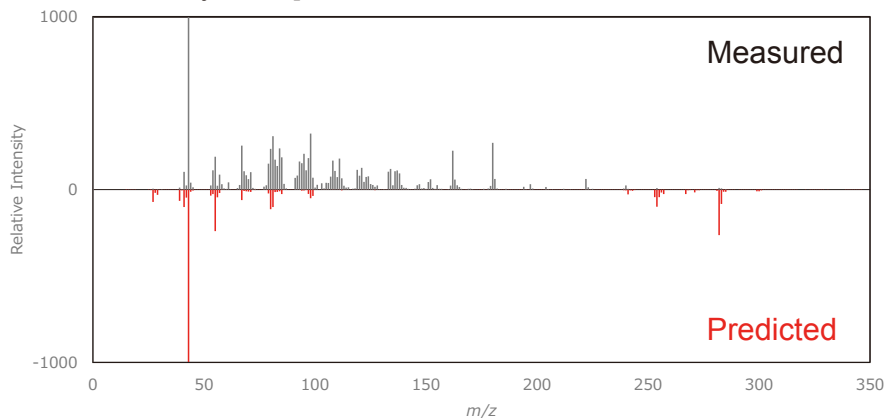
a) benzamide, 3-methyl-N-decyl-
[cosine similarity: 0.95]



b) N-Acetyl-3-(3-formyl-4-methoxyphenyl)-d-alanine methyl ester
[cosine similarity: 0.72]



c) cyclododecane, 1,5,9-tris(acetoxy)-
[cosine similarity: 0.34]



— Accuracy evaluation of structural analysis —

AI structural analysis compares EI mass spectra predicted from structural formula candidates with the actual measured EI mass spectrum to identify the structural formula. We evaluated the accuracy of this structural formula identification. The evaluation method is as follows: First, for the compounds in the NIST 20 library that were not used in training, structural formulas (compounds) that have the same molecular formula were extracted from the compound database. Next, the trained main AI predicted EI mass spectra for the correct structural formula and the extracted ones. The predicted EI mass spectra were compared with the ones registered in the NIST 20 library, and based on their cosine similarities, all the structural formulas, including the correct one, were ranked. We used the rank given by the correct structural formula among all the structural formulas as the index of accuracy evaluation. In this evaluation, to set certain criteria, we used only molecular formulas for which at least 100 compound candidates were extracted from the compound database.

Table 1 shows the results of ranking structural formulas for 14,581 compounds. The results indicate that the correct structural formula ranked top for 22% of the compounds. In addition, the correct structural formula ranked in the top 1% for 73% of the compounds. Ranking in the top 1% means that the

correct structural formula was placed within the top 10 out of 1,000 candidates. The PubChem compound database contains many compounds that have quite similar structural formulas. With taking this into consideration, this structural formula identification method is said to be highly accurate.

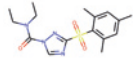
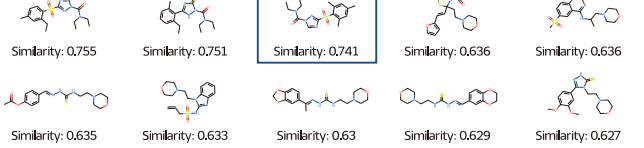
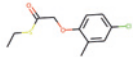
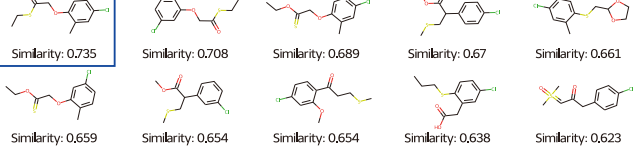
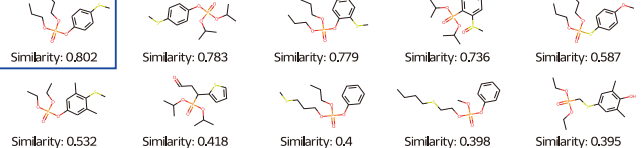
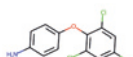
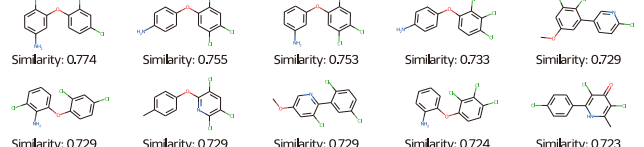
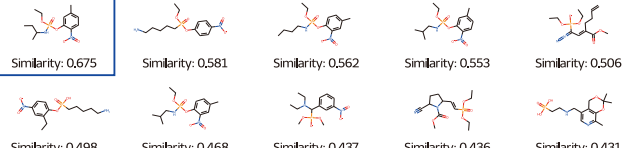
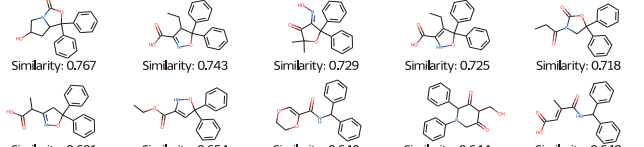
Next, we evaluated the effectiveness of this method for completely unknown compounds. We used model compounds that are not registered in the NIST 20 library to perform the evaluation. The following model compounds were used: Cafenstrole (CAS: 125306-83-4, Wako), MCPA-thioethyl (CAS: 25319-90-8, Wako), Propaphos (CAS: 7292-16-2, Wako), CNP-amino (CAS: 26306-61-6 Wako), Butamifos oxon (CAS: 56362-05-1 Wako), and Isoxadifen-ethyl (CAS: 163520-33-0, Wako).

The measured EI mass spectra for the model compounds were prepared by measuring standard samples. **Table 2** shows

Table 1 Results of accuracy evaluation on 14,581 compounds.

	Top	Within the top 1%	Within the top 5%	Within the top 10%
Number of Compounds	3215 (22 %)	10618 (73 %)	12934 (89 %)	13594 (93 %)

Table 2 Examples of structural analysis results.

Compound Name	Structure	Similarity	Rank	Top 10 structures
Cafenstrole		0.741	3 (2933)	 Similarity: 0.755 Similarity: 0.751 Similarity: 0.741 Similarity: 0.636 Similarity: 0.636 Similarity: 0.635 Similarity: 0.633 Similarity: 0.63 Similarity: 0.629 Similarity: 0.627
MCPA-thioethyl		0.735	1 (729)	 Similarity: 0.735 Similarity: 0.708 Similarity: 0.689 Similarity: 0.67 Similarity: 0.661 Similarity: 0.659 Similarity: 0.654 Similarity: 0.654 Similarity: 0.638 Similarity: 0.623
Propaphos		0.802	1 (27)	 Similarity: 0.802 Similarity: 0.783 Similarity: 0.779 Similarity: 0.736 Similarity: 0.587 Similarity: 0.532 Similarity: 0.418 Similarity: 0.4 Similarity: 0.398 Similarity: 0.395
CNP-amino		0.710	14 (618)	 Similarity: 0.774 Similarity: 0.755 Similarity: 0.753 Similarity: 0.733 Similarity: 0.729 Similarity: 0.729 Similarity: 0.729 Similarity: 0.729 Similarity: 0.724 Similarity: 0.723
Butamifos oxon		0.675	1 (56)	 Similarity: 0.675 Similarity: 0.581 Similarity: 0.562 Similarity: 0.553 Similarity: 0.506 Similarity: 0.498 Similarity: 0.468 Similarity: 0.437 Similarity: 0.436 Similarity: 0.431
Isoxadifen-ethyl		0.586	22 (5348)	 Similarity: 0.767 Similarity: 0.743 Similarity: 0.729 Similarity: 0.725 Similarity: 0.718 Similarity: 0.691 Similarity: 0.654 Similarity: 0.649 Similarity: 0.644 Similarity: 0.642

the rank given by the correct structural formula, its score, and top 10 structural formulas in descending order of score for each model compound. For three compounds out of the six, the correct structural formula ranked top. For Isoxadifen-ethyl, the correct structural formula ranked lowest compared with the other five model compounds. However, it was placed 22nd out of 5,348 candidates, within top 1%. The result suggests that this structural formula identification method is effective in narrowing down the correct structural formula from many candidates. The top-ranked structural formulas for Cafenstrole, CNP-amino, and Isoxadifen-ethyl have the same size and number of rings as their correct structural formulas do, and they show considerable similarity. The results of our evaluation on these six compounds reveal that this identification method is useful in structural analysis. **Figure 9** shows the comparisons between the measured and predicted mass spectra. The measured and predicted mass spectra exhibit the same peaks with high intensity, although they are different in detailed peak intensities and distributions of mild peaks.

These results confirm that this method is effective in the structural analysis of unknown compounds.

Conclusions

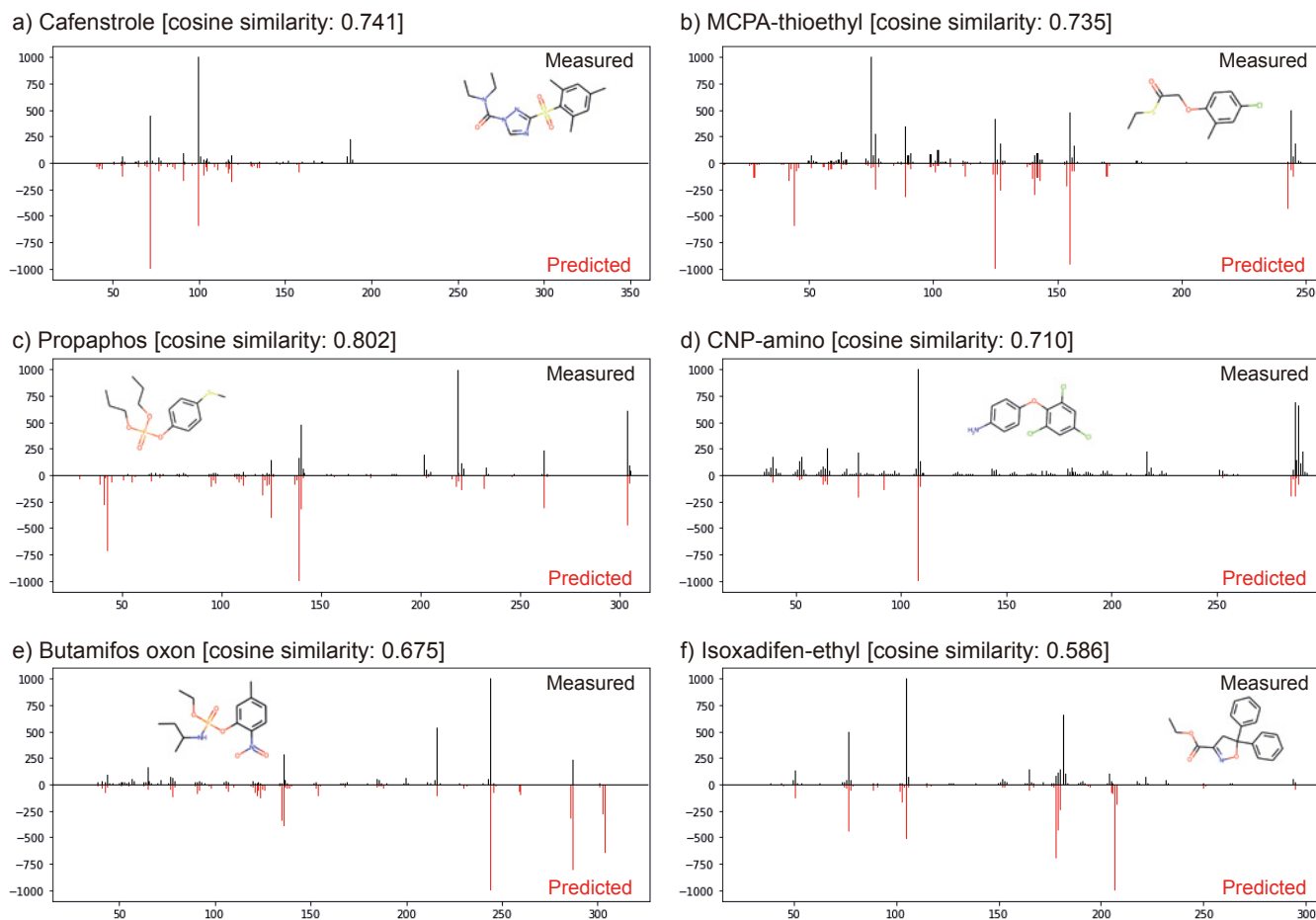
Previous msFineAnalysis software features integrated analysis based on accurate mass measurement and molecular ion observation using the soft ionization method, which are

features of the JMS-T2000GC. Integrated analysis enables the identification of molecular formulas of unknown compounds. The new version, msFineAnalysis AI, is equipped with structural analysis using artificial intelligence (AI), which enables molecular formulas as well as structural formulas to be automatically obtained. msFineAnalysis AI extracts structural formula candidates based on the molecular formulas identified by integrated analysis. Then, it uses the EI mass spectra predicted from the structural formula candidates by the AI to identify the structural formula. The combination of integrated analysis and AI enables a highly efficient and accurate structural analysis. All the processes are performed automatically and offline, leading to a stable analysis.

References

- [1] Masaaki Ubukata. MultiAnalyzer – Unknown Compounds Analysis System New Gas Chromatograph Time-of-Flight Mass Spectrometer JMS-T2000GC “AccuTOF™ GC-Alpha”. *JEOL news* Vol. **56**.
- [2] Masaaki Ubukata, Yoshihisa Ueda. Development of an Integrated Analysis Method for the JMS-T200GC High Mass-Resolution GC-TOFMS by Electron Ionization and Soft Ionization Methods. *JEOL news* Vol. **54**.
- [3] J. Gilmer, S. S. Schoenholz, P. F. Riley, O. Vinyals, G. E. Dahl. Neural message passing for Quantum chemistry. *Proceedings of the 34th International Conference on Machine Learning*. 2017;70:1263-1272.

Fig. 9 Comparison between the measured and predicted mass spectra.



He-less Light Element Analysis Using a Low-Vacuum Liquid Sample Capsule by X-ray Fluorescence Spectrometry

Genki Kinugasa¹, Naoki Muraya¹ and Hiroshi Onodera²

¹ SA Business Unit, JEOL Ltd. ² EP Business Unit, JEOL Ltd.

X-ray fluorescence analysis (XRF) is used to measure elements in solids, powders, and liquids. In X-ray fluorescence analysis, low energy X-rays (light elements) can be measured in the sample chamber in a vacuum atmosphere to reduce the absorption of X-rays by gas molecules. Liquid samples are difficult to measure in vacuum; therefore, replacing the air with helium gas is often used because helium has low X-ray absorption characteristics. Using this technique, XRF is used to analyze chlorine and sulfur in oil and mineral components such as magnesium in food. However, helium is in short supply and its price is rising. Alternative methods to the helium replacement method are desperately needed. Against this background, we have developed a "low-vacuum liquid sample capsule" that enables the measurement of liquid samples in a vacuum atmosphere without the need for helium gas. This paper introduces this method and its measurement examples.

Introduction

Detectable elements range from carbon (C) to uranium (U). Detection of light elements (carbon (C) to magnesium (Mg)) is difficult unless the sample chamber atmosphere is evacuated. Low-energy X-ray fluorescence is absorbed by the atmosphere and its intensity is significantly attenuated. Therefore, simultaneous detection of light and heavy elements is possible if the sample chamber atmosphere is under vacuum. However, a liquid sample cannot be measured when the sample chamber is in a vacuum. This is because liquid samples freeze or evaporate when measured in a vacuum atmosphere. For this reason, the measurement of liquid samples has been carried out under a helium atmosphere or by using the dry concentration method [1], in which the liquid is deposited onto a filter or film and dried. Although the dry concentration method is excellent for qualitative analysis; it is difficult to perform accurate quantitative analysis because it is difficult to fix the sample uniformly.

Analysis of liquid samples

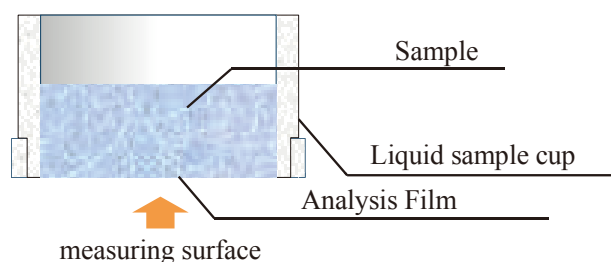
When measuring a liquid sample, the sample is filled into a dedicated cup as shown in **Fig. 1**, and measured in an atmosphere to maintain the liquid state. However, in atmospheric measurements, the fluorescent X-rays generated from the sample are absorbed by the atmosphere. In addition, low energy X-rays are also absorbed by the analysis film attached to the cup, since the detection of fluorescent X-rays is carried out through the analysis film supporting the liquid.

Absorption of X-rays

-Atmospheric absorption-

Figure 2 shows the effect of the sample atmosphere on the absorption of X-rays emitted from the sample. The figure is normalized by the X-ray fluorescence intensity measured in a vacuum atmosphere, and the intensity ratios in air and helium

Fig. 1 Liquid sample cup and usage.



atmospheres are plotted for each element. The results show that the lower energy X-ray (Na, Mg, Al, and Si) are more difficult to detect due to the higher absorption of X-rays by the atmosphere. On the other hand, in a helium atmosphere, the absorption of X-rays is smaller than in atmosphere. For liquid samples that are difficult to keep in a vacuum atmosphere, the sample chamber has been replaced with helium gas for measurement.

-Absorption by film-

Figure 3 shows a graph calculating the amount of X-ray absorption by the analysis film. X-ray absorption by the film also occurs when X-ray pass through the analysis film. When measuring a liquid sample, absorption by the analysis film must be taken into consideration. In the low-vacuum liquid sample capsule introduced here, two analysis films are used to prevent leakage of liquid, and the amount of absorption when two films are used is added to the graph. The film is assumed to be a polypropylene polymer with a density of 0.91 g/cm³ and a thickness of 4 μm.

Low-vacuum liquid sample capsule

Figure 4 shows a schematic diagram of a low-vacuum liquid sample capsule. The low-vacuum liquid sample capsule contains a liquid sample cup inside. The liquid sample cup has an analysis film on the bottom and is filled with a liquid sample in the center. The low-vacuum liquid sample capsule is equipped with a pressure control mechanism and a leak valve. After the low-vacuum liquid sample capsule is placed in the sample chamber of XRF instrument, the entire sample chamber is evacuated. The inside of the low-vacuum liquid sample capsule is also evacuated through the pressure control mechanism, causing the pressure to drop. When the pressure reaches the pressure set by the pressure control mechanism, the pressure drop stops and the low-vacuum liquid sample capsule is closed. The pressure inside the low-vacuum liquid sample capsule can be set between approximately 20,000 and 10,000 Pa, which is higher than the vapor pressure of water at room temperature, enabling analysis while maintaining the liquid

state (**Fig. 5**). The analysis film is a thin polymer film for X-ray analysis, and if the pressure is increased, the film will break and leak liquid samples. Therefore, the pressure is set below the pressure resistance of the analysis film. For this reason, samples with a low boiling point and a vapor pressure higher than the recommended pressure at room temperature cannot be measured.

1) How to use the low-vacuum liquid sample capsule

The low-vacuum liquid sample capsule consists of two parts: the upper pressure control capsule and the lower sample cup (**Fig. 6**).

The pressure control capsule has a mechanism to adjust the pressure inside the capsule. The sample cup is a standard liquid sample cup that can be easily replaced. The sample cup has a groove cut around it, which can be filled with buffer solution to prevent sample vaporization.

2) Recommended pressure of analysis film

Analytical films of different thicknesses and materials are available for X-ray fluorescence analysis.

Table 1 shows the results of measuring the breakdown pressure when typical analysis films were used.

The pressure at which the analysis film breaks was measured by externally applying pressure to a low-vacuum liquid sample capsule using a compressor. A value approximately 1/3 of the breakdown pressure was set as the recommended pressure.

3) Dealing with bubbles generated from the sample

The internal pressure of a low-vacuum liquid sample capsule is lower than atmospheric pressure, which can easily generate bubbles in the sample. Increasing the pressure inside the capsule can prevent the generation of bubbles (**Fig. 7**).

4) Buffer solution

The low-vacuum liquid sample capsule can be filled with buffer solution to prevent vaporization of the sample (**Fig. 8**).

The buffer liquid filling groove and the sample cup filled with the sample are separated by a porous film, which makes the pressure lower in the buffer liquid space.

Fig. 2 X-ray absorption rate by measurement atmosphere.

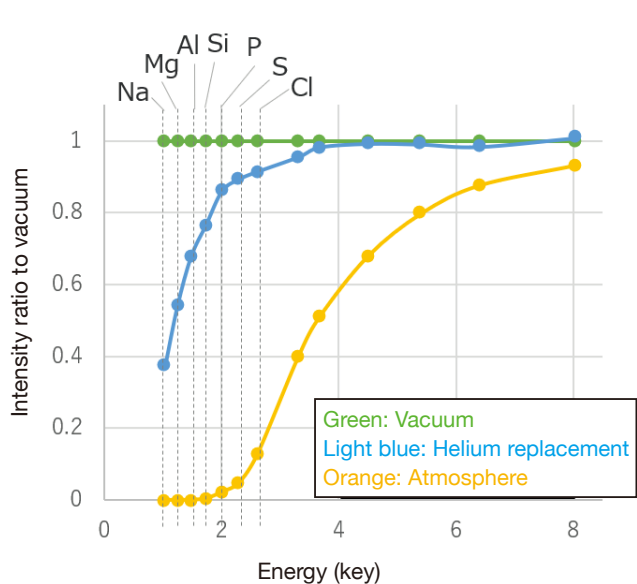
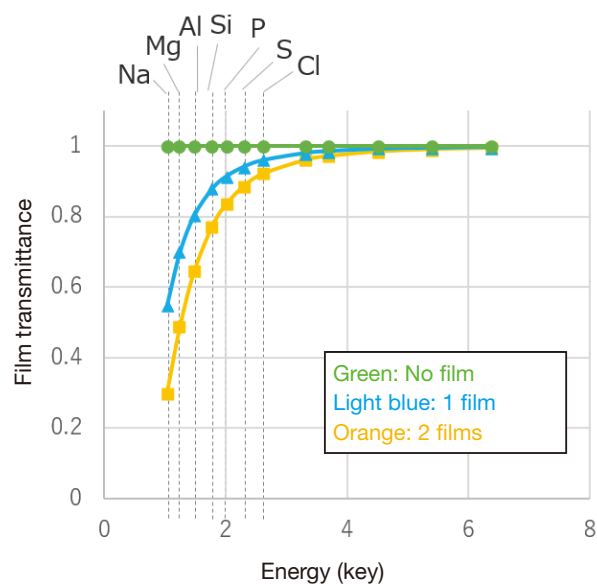


Fig. 3 X-ray absorption rate by analysis film.



The low pressure makes it easy for the sample to vaporize even if the pressure is higher than the sample vapor pressure. However, since the buffer solution in the lower pressure space vaporizes before the sample, it prevents sample vaporization and enables stable measurement over a long period of time.

Figure 8 shows the variation of X-ray intensity of phosphorus (P) in an aqueous solution containing phosphorus (P) (liquid fertilizer) measured with and without buffer solution over a long measurement time. The changes are normalized by the intensity

at the start of the measurement. It can be seen that the addition of buffer solution stabilizes the X-ray intensity of P.

Lower Limit of Detection

Elemental reference solutions were measured using a low-vacuum capsule to determine the lower limit of detection (Table 2).

Na and Mg were detectable up to about 1000 ppm and 100 ppm, respectively.

Fig. 4 Schematic diagram of low-vacuum liquid sample capsule.

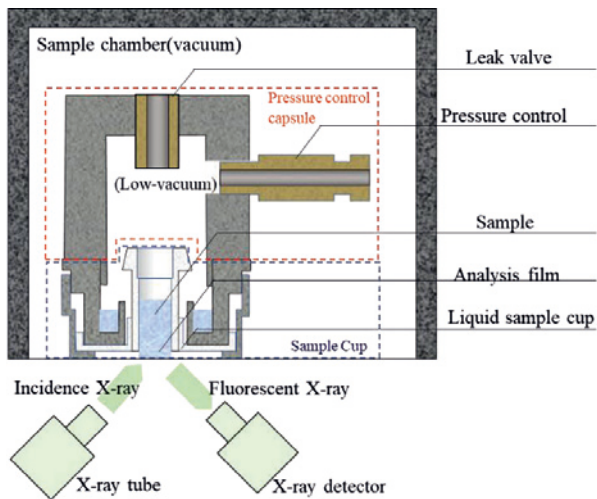


Fig. 5 Set pressure of low-vacuum liquid sample capsule.

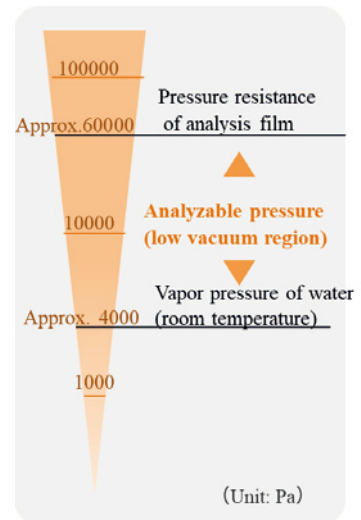


Fig. 6 Sample preparation in the low-vacuum liquid sample capsule.

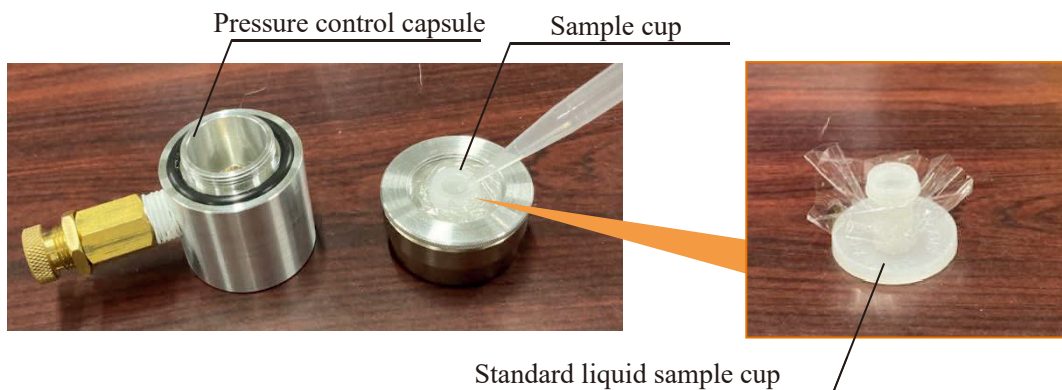


Table 1 Pressure resistance table for analytical film.

Analysis film	Thickness	Breakdown pressure	recommended pressure
Prolene*1	4 μm	Approx. 210 kPa	70 kPa
Prolene*1	3 μm	Approx. 180 kPa	60 kPa
Mylar*2	2.5 μm	Approx. 160 kPa	50 kPa
Etnom*1	1.5 μm	Approx. 100 kPa	30 kPa

*1 Registered trademark of Chemplex

*2 Registered trademark of DuPont

Fig. 7 Relationship between the set pressure of the low-vacuum capsule and bubbles.

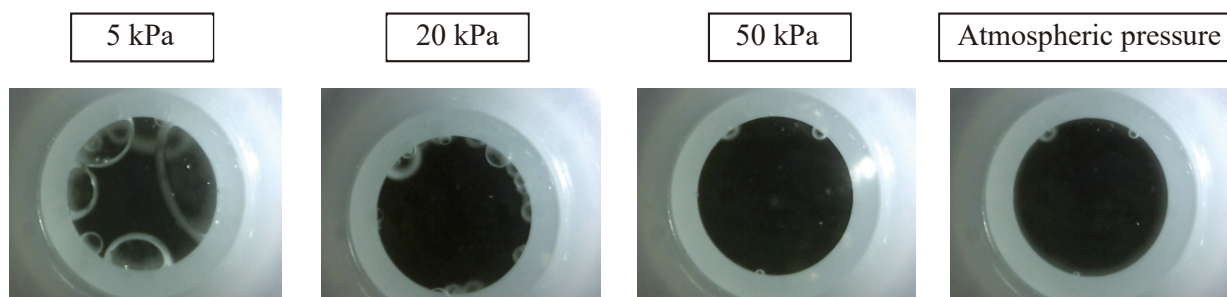
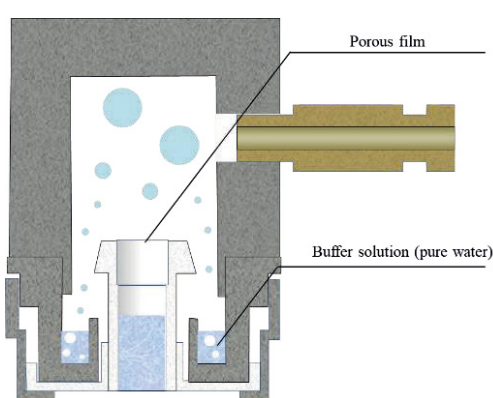
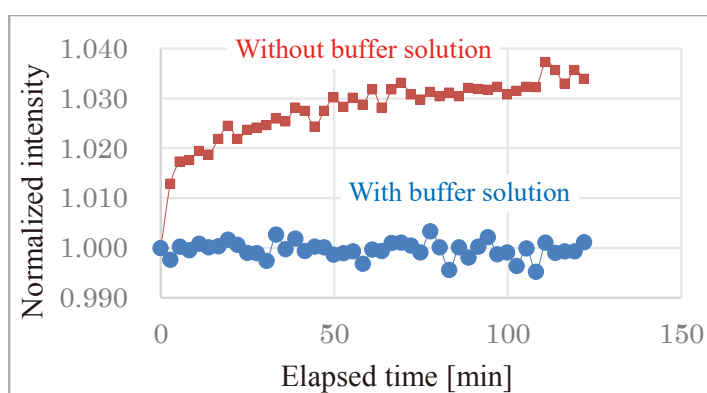


Fig. 8 Schematic diagram of the low-vacuum liquid sample capsule and long-term measurement of P in liquid fertilizer.



Measurement instrument: JSX-1000S
Low-vacuum liquid sample capsule set pressure: 20 kPa



Measurement conditions
Tube voltage: 30 kV, Collimator: 2 mm, Filter: Open
Measurement time: 120 s repetition measurement

Table 2 Lower limit of detection when using a low-vacuum liquid sample capsule.

Element	Lowest limit of detection (ppm)
Na	1,228
Mg	108

Measurement conditions
Measurement time: 300 s
Tube voltage: 15 kV
Filter: OPEN
Collimator: 2 mm
Note: Prolene film 4 μ m

Examples of analysis using the low-vacuum liquid sample capsule

1) Analysis of additives in oil

Magnesium compounds are contained in engine oil as a clean dispersant.

Comparing the spectra taken under vacuum and atmospheric pressure, a magnesium (Mg) peak that was not detected at atmospheric pressure could be confirmed under vacuum condition. Quantitative analysis was performed. Thin-film FP method was used to correct for the absorption of two analytical films. The analysis was performed assuming the structural formula of CH_2 and the density of 0.91 g/cm^3 (Fig. 9).

2) Analysis of food minerals in soy milk

Magnesium in soy milk is difficult to detect because its concentration is lower than that of oil. The use of a liquid sample

capsule enables detection of magnesium at low concentrations. Due to the low X-ray intensity of magnesium, a thin 3- μ m Prolene film was used for the analysis and the measurement time was extended to 600 seconds. Quantitative analysis was performed in the same way as for oil (Fig. 10).

3) Analysis of disodium hydrogen phosphate solution

In X-ray fluorescence analysis, not only mass concentration calculation but also molar concentration calculations is possible.

From the molar concentration of phosphoric acid and sodium ions, the ratio of sodium to phosphoric acid was 2:1. The absorption of the analytical film was corrected and a reasonable quantitative analysis result was calculated. (Fig. 11).

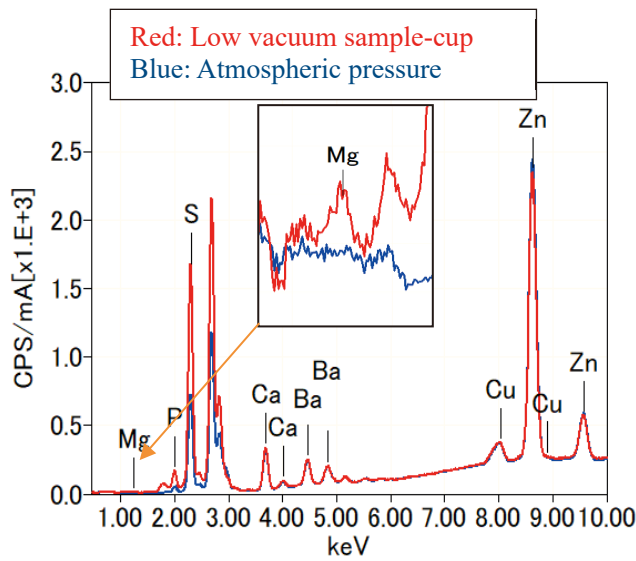
Conclusion

The use of a low-vacuum liquid sample capsule for the analysis of light elements in liquids provides results equivalent to or better than helium-substituted instruments, provided that the instrument is equipped with a sample chamber pumping unit. This enables stable measurement of light elements in liquids without the use of helium, a scarce resource.

References

- [1] Izumi Nakai “Keikou-Xsen-bunseki no Gisai” Asakura Publishing Co., Ltd.

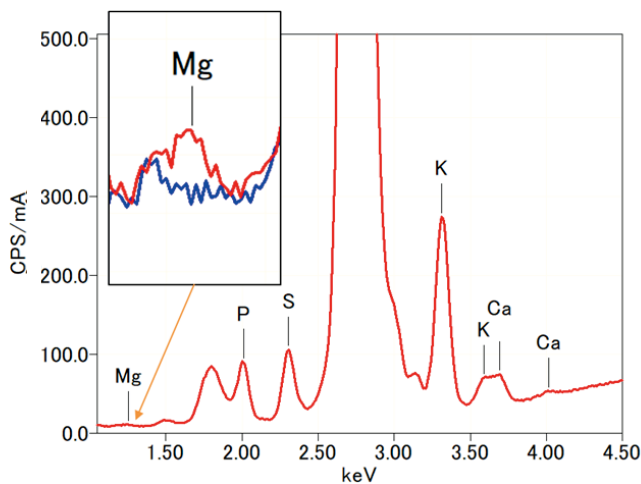
Fig. 9 Example of oil sample measurement. Comparison between measurements under atmospheric pressure and using a low-vacuum capsule.



Element	Reference	Analysis value
Mg	0.09%	0.09%
P	0.09%	0.08%
Zn	0.09%	0.10%
Ba	0.09%	0.08%
Ca	0.09%	0.07%
CH ₂		99.60%

Measurement conditions
 Measurement time: 120 s
 Tube voltage: 30 kV
 Filter: OPEN
 Collimator: 2 mm
 Memo: Prolene film 4 μm

Fig. 10 Example of measuring trace magnesium in food.

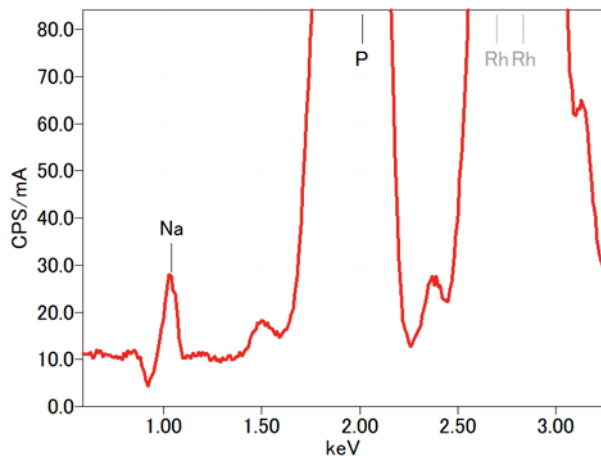


Element	Reference	Analysis value
Mg	53 mg	68.4 mg
Ca	34 mg	37.0 mg
K	425 mg	379 mg
H ₂ O		99.6%

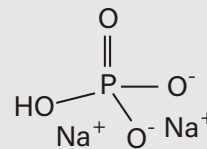
(per 200 ml)

Measurement conditions
 Measurement time: 600 s
 Tube voltage: 30 kV
 Filter: OPEN
 Sample: Soy milk
 Memo: Prolene film 3 μm

Fig. 11 Example of chemical measurement.



Disodium phosphate



Element	Analysis value	unit
Na	3.53	mol%
HPO ₄	1.55	mol%
H ₂ O	94.91	mol%

▼ Local office



Certain products in this brochure are controlled under the "Foreign Exchange and Foreign Trade Law" of Japan in compliance with international security export control. JEOL Ltd. must provide the Japanese Government with "End-user's Statement of Assurance" and "End-use Certificate" in order to obtain the export license needed for export from Japan. If the product to be exported is in this category, the end user will be asked to fill in these certificate forms.



3-1-2 Musashino Akishima Tokyo 196-8558 Japan Sales Division Tel. +81-3-6262-3560 Fax. +81-3-6262-3577
www.jeol.com ISO 9001 • ISO 14001 Certified

ARGENTINA

COASIN S.A.C.I.yF.
Virrey del Pino 4071,
C1430CAM-Buenos Aires
Argentina
Tel. 54-11-4552-3185
Fax. 54-11-4555-3321

AUSTRALIA & NEW ZEALAND

JEOL (AUSTRALASIA) Pty.Ltd.
Suite 1, L2 18 Aquatic Drive
- Frenchs Forest NSW 2086
Australia
Tel. 61-2-9451-3855
Fax. 61-2-9451-3822

AUSTRIA

JEOL (GERMANY) GmbH
Gute Aenger 30
85356 Freising, Germany
Tel. 49-8161-9845-0
Fax. 49-8161-9845-100

BANGLADESH

A.Q. CHOWDHURY SCIENCE & SYNERGY PVT. LTD.
87, Suhrawardy Avenue, Floor 2
Baridhara, Dhaka1212
Bangladesh
Tel. 88-02-222262272
Fax. 88-02-222264228

BELGIUM

JEOL (EUROPE) B.V.
Planet II, Gebouw B
Leuvensesteenweg 542,
B-1930 Zaventem
Belgium
Tel.32-2-720-0560
Fax.32-2-720-6134

BRAZIL

JEOL Brasil Instrumentos Cientificos Ltda.
Av. Jabaquara, 2958 5º andar conjunto 52 ;
04046-500 Sao Paulo, SP
Brazil
Tel. 55-11-5070 4000
Fax. 55-11-5070 4010

CANADA

JEOL CANADA, INC.
3275 1ere Rue, Local #8
St-Hubert, QC J3Y-6Y6, Canada
Tel. 1-450-676-8776
Fax. 1-450-676-6694

CHINA

JEOL (BEIJING) CO., LTD.
Zhongkezyuan Building South Tower 2F,
Zhongguancun Nanshanjie Street No. 6,
Haidian District, Beijing, P.R.China
Tel. 86-10-6804-6321
Fax. 86-10-6804-6324

JEOL (BEIJING) CO., LTD., SHANGHAI BRANCH

2F-BC Room, Building A, Mingji Business Plaza,
No.207 Songhong Road, Changning District,
Shanghai 200335, P.R.China
Tel. 86-21-6249-4487
Tel. 86-21-5836-6350
Fax. 86-21-5836-3668

JEOL (BEIJING) CO., LTD., GUANGZHOU BRANCH

Rm.3501, OneInCenter, 230 Tianhe Road, Tianhe District,
Guangzhou, Guangdong Prov., 510620, China
Tel. 86-20-8778-7848
Fax. 86-20-8778-4268

JEOL (BEIJING) CO., LTD., WUHAN BRANCH

Room A2118, Zhongshang Plaza Office Bldg.,
No. 7 Zhongnan Road, Wuhuan,
Hubei, 430070, P.R.China
Tel. 86-27-8713-2567
Fax. 86-27-8713-2567

JEOL LTD. (BEIJING) CO., LTD., CHENGDU BRANCH

1807A Zongfu Building,
NO. 35 Zhongfu Road, Chengdu, Sichuan, 610016
P.R. China
Tel. 86-28-86622554
Fax. 86-28-86622564

EGYPT

JEOL SERVICE BUREAU
3rd Fl. Nile Center Bldg., Nawal Street,
Dokki, Cairo, Egypt
Tel. 20-2-3335-7220
Fax. 20-2-3338-4186

FRANCE

JEOL (EUROPE) SAS
Espace Claude Monet, 1 Allée de Giverny
78290, Croissy-sur-Seine, France
Tel. 33-13015-3737
Fax. 33-13015-3747

GERMANY

JEOL (GERMANY) GmbH
Gute Aenger 30
85356 Freising, Germany
Tel. 49-8161-9845-0
Fax. 49-8161-9845-100

GREAT BRITAIN & IRELAND

JEOL (U.K.) LTD.
Silver Court, Watchmead,
Welwyn Garden City, Hertfordshire AL7 1LT, U.K.
Tel. 44-1707-377117
Fax. 44-1707-373254

GREECE

N. ASTERIASIS S.A.
56-58 S. Trikoupi Str. P.O. Box 26140
GR-10022, Athens, Greece
Tel. 30-1-823-5383
Fax. 30-1-823-9567

HONG KONG

FARMING LTD.
Unit No. 1009, 10/F, Prosperity
663 King's Road, North Point, Hong Kong
Tel. 852-2915-7299
Fax. 852-2581-4635

INDIA

JEOL INDIA PVT. LTD.
Unit No.305, 3rd Floor,
ABW Elegance Tower,
Jasola District Centre,
New Delhi 110 025, India
Tel. 91-11-4595-8000
Tel. 91-11-4595-8005
Tel. 91-11-4595-8017

JEOL INDIA PVT. LTD. Mumbai Office

214 E Square, Subhash Road,
Vile Parle (EAST),
Mumbai 400 057, India
Tel. 91-22-2612-9387

JEOL INDIA PVT. LTD. Bangalore Office

422, Regus Solitaire Business centre,
1-10-39 to 44, level 4, Gumtelli Towers,
Old Airport Road,
Begumpet, Hyderabad - 500016, India
Tel. 91-40-6704-3708

JEOL INDIA PVT. LTD. Kolkata Office

422, Regus Solitaire Business centre,
1-10-39 to 44, level 4, Gumtelli Towers,
Old Airport Road,
Begumpet, Hyderabad - 500016, India
Tel. 91-40-6704-3708

INDONESIA

PT. TEKNO LABindo Penta Perkasa
Komplek Gading Bukit Indah Blok I/11
Jl. Bukit Gading Raya Kelapa Gading Permai,
Jakarta 14240, Indonesia
Tel. 62-21-45847057/58
Fax. 62-21-45842729

ITALY

JEOL (ITALIA) S.p.A.
Palazzo Pacinotti - Milano 3 City,
Via Ludovico il Moro, 6/A
20079 Basiglio(MI) Italy
Tel. 39-02-9041431
Fax. 39-02-90414343

KOREA

JEOL KOREA LTD.
Dongwoo Bldg. 7F, 1443, Yangjae Daero,
Gangdong-Gu, Seoul, 05355, Korea
Tel. 82-2-511-5501
Fax. 82-2-511-2635

KUWAIT

Ashraf & CO. Ltd.
P.O.Box 3555 Safat 13036, Kuwait
Tel. 965-1805151
Fax. 965-2435373

MALAYSIA

JEOL (MALAYSIA) SDN.BHD.
508, Block A, Level 5,
Kelana Business Center,
97, Jalan SS 7/2, Kelana Jaya,
47301 Petaling Jaya, Selangor, Malaysia
Tel. 60-3-7492-7722
Fax. 60-3-7492-7723

MEXICO

JEOL DE MEXICO S.A. DE C.V.
Arkansas 11 Piso 2
Colonia Napoles,
Delegacion Benito Juarez, C.P. 03810
Mexico D.F., Mexico
Tel. 971-4-609-1497
Fax. 92-5-55-211-4511
Fax. 92-5-55-211-0720

Middle East

JEOL GULF FZCO
P.O. Box No. 371107
Dubai Airport Free Trade Zone West Wing 5WA No. G12,
Dubai, UAE
Tel. 971-4-609-1497
Fax. 971-4-609-1498

PAKISTAN (Karachi)

ANALYTICAL MEASURING SYSTEM (PVT) LTD. (AMS LTD.)
14-C Main Sehar Commercial Avenue Lane 4,
Khayaban-e-Sehar,
D.H.A-VII, Karachi-75500, Pakistan
Tel. 92-21-35345581/35340747
Fax. 92-21-35345582

PANAMA

PROMED S.A.
Parque Industrial Costa del Este
Urbanizacion Costa del Este
Apartado 0816-01755, Panama, Panama
Tel. 507-303-3100
Fax. 507-303-3115

PHILIPPINES

JATEC Philippines Corporation
28 Floor, The Enterprise Center Tower 2,
Ayala Avenue corner Paseo de Roxas,
Ergy, San Lorenzo, Makati City, 1226 Philippines
Tel. (632) 849 3304

PORTUGAL

Izessa Portugal Lda.
R. do Proletariado, 1
2790-138 CARNAXIDE, Portugal
Tel. 351-21-424-73-00
Fax. 351-21-418-60-20

QATAR

Mannai Trading Company W.L.L.
AlU Emadi Complex,
Salwa Road P.O.Box 76, Doha, Qatar
Tel. +974 4455-8216
Fax. +974 4455-8214

RUSSIA

JEOL (RUS) LLC
Office 351, floor 3, 23,
Novoslobodskaya St,
Moscow 127055, Russia
Tel. 7-495-748-7791/7792
Fax. 7-495-748-7793

SAUDI ARABIA

ABDULREHMAN ALGOSAIBI G.T.C. (Riyadh)
Algosaibi Building-Old Airport Road
P.O. Box 215, Riyadh-11411, Saudi Arabia
Tel. 966-1-477-7302

SCANDINAVIA

SWEDEN
JEOL (Nordic) AB
Hammarbacken 6A, Box 716, 191 27 Sollentuna
Sweden
Tel. 46-8-28-2800
Tel. 46-8-29-1647
Fax. 46-8-29-1647

SINGAPORE

JEOL ASIA PTE.LTD.
2 Corporation Road
#01-12 Corporation Place
Singapore 618494
Tel. 65-6565-9989
Fax. 65-6565-7552

SOUTH AFRICA

ADI Scientific (Pty) Ltd.
370 Angus Crescent,
Northlands Business Park, 29 Newmarket Road
Northriding, Randburg, Republic of South Africa
Tel. 27-11-462-1363
Fax. 27-11-462-1466

SPAIN

IZASA Scientific SLU.
Argoneses, 13, 28108 Alcobendas,
Madrid, Spain
Tel. 34 902 20 30 80
Fax. 34 902 20 30 81

SWITZERLAND

JEOL (GERMANY) GmbH
Gute Aenger 30
85356 Freising, Germany
Tel. 49-8165-77346
Fax. 49-8165-77512

TAIWAN

JEI DONG CO., LTD.
7F, 112, Chung Hsiao East Road,
Section 1, Taipei, Taiwan 10023 (R.O.C.)
Tel. 886-2-2395-2978
Fax. 886-2-2322-4655

For NMR & Mass Spectrometer Products:

TechnMax Technical Co., Ltd.
5F, No. 11, Wuqian 2nd Rd., Wugu Dist.,
New Taipei City 248, Taiwan (R.O.C.)
Tel. 886-2-8990-1779
Fax. 886-2-8990-2559

For Semiconductor Products:

JEOL TAIWAN SEMICONDUCTORS LTD.
2F-2, No. 192, Dongguang Rd.
East Dist., Hsinchu City 30069,
Taiwan (R.O.C.)
Tel. 886-3-571-5656
Fax. 886-3-571-5151

THAILAND

BECTHAI BANGKOK EQUIPMENT & CHEMICAL CO., Ltd.
300 Phaholyothin Rd. Phayathai, Bangkok 10400,
Thailand
Tel. 66-2-615-2929
Fax. 66-2-615-2350/2351

JEOL ASEAN TECHNICAL CENTER (JATC)

MTEC building room 533
114 Moo9, Thailand Science Park
Phaholyothin Rd., Klong 1, Klong Luang,
Pathumthani 12120
THAILAND
Tel. 66-2-564-7738
Fax. 66-2-564-7739

THE NETHERLANDS

JEOL (EUROPE) B.V.
Lireweg 4, NL-2153 PH Nieuw-Vennep,
The Netherlands
Tel. 31-252-623500
Fax. 31-252-623501

TURKEY

Tekser A.S.
Kartal Cad. No: 55/3 Inonu Wah.,
Atasehir 34755, Istanbul, Turkey
Tel. 90-216-5736470
Fax. 90-216-5736475

USA

JEOL USA, INC.
11 Dearborn Road, Peabody, MA 01960, U.S.A.
Tel. 1-978-535-5900
Fax. 1-978-536-2205/2206

JEOL USA, INC. WEST OFFICE

5653 Stoneridge Drive Suite #110
Pleasanton, CA 94588, U.S.A.
Tel. 1-925-737-1740
Fax. 1-925-737-1749

VENEZUELA

GOMSA Service and Supply C.A.
Urbanizacion Montalban III
- Residencias Don Andres - Piso 7 - Apartamento 74
Avenida 3, entre calles 7 y 6
Montalban, Caracas, Venezuela
Tel. 58-212-443-4342
Fax. 58-212-443-4342

VIETNAM

TECHNICAL MATERIALS AND RESOURCES
IMPORT-EXPORT JOINT STOCK COMPANY(REXCO)
Hanoi Branch
SALES & SERVICE
159-157 Lang Ha Street, Dong Da District, Hanoi, Vietnam
Tel. +84 (43) 562 0516
Fax. +84 (43) 853 2511